The Dissertation Committee for Matthias Franz Taus
certifies that this is the approved version of the following dissertation:

Isogeometric Analysis for Boundary Integral Equations

Committee:

Gregory J. Rodin, Supervisor

Thomas J. R. Hughes, Co-Supervisor

Leszek F. Demkowicz

George Biros

Francisco Javier Sayas

Isogeometric Analysis for Boundary Integral Equations

by

Matthias Franz Taus, D.I.; M.S.C.S.E.M.

DISSERTATION

Presented to the Faculty of the Graduate School of

The University of Texas at Austin

in Partial Fulfillment

of the Requirements

for the Degree of

DOCTOR OF PHILOSOPHY

THE UNIVERSITY OF TEXAS AT AUSTIN

December 2015

Für meine Großeltern

Alois und Gertrude Brandner

Franz und Erika Taus

Acknowledgments

At this point I would like to thank all those people who have supported me throughout the years. Without them, I would have not been able to complete or even start this dissertation. In particular, I would like to thank the following: My advisors Gregory J. Rodin and Thomas J. R. Hughes; their guidance, encouragement and insight have made me evolve not only in research but also in life. Michael A. Scott; his help and discussions have enormously helped me to understand Isogeometric Analysis. My committee members Leszek F. Demkowicz, George Biros and Francisco Javier Sayas; their very useful and insightful input has greatly improved the quality of this work. The Institute for Computational Engineering and Sciences at the University of Texas at Austin, the National Science Foundation, and the Fulbright Foundation; their financial support has made it possible for me to enter and continue the PhD program.

I would also like to thank the people who have made it possible for me to start this dissertation. I would like to thank my undergraduate advisor, Olaf Steinbach, who taught me the basics of research and computational mathematics. Without his academic and personal advice I would never have made it so far. Further, I am very grateful for my high school teachers in mathematics, Sabina Söllinger and Dietmar Ticar, they were the first to introduce me into

the world of mathematics and showed me the joy one experiences when solving hard problems.

I am also very grateful for the support of my friends and family in Austria and the United States. First, I wish to thank my family for teaching me the value of commitment, responsibility and hard work. In particular, I would like to thank my parents, Franz and Beate Taus, and my grandparents to whom I have dedicated this dissertation. I would also like to thank the students of the CSEM program at the University of Texas at Austin for their support and for the welcoming environment they have provided for me in the United States. I wish to thank my friends in Austria in and around the saving's club, Sparverein zum Frommen Schülling. They have provided me with the feeling that there will always be a group where I belong.

Last but not least, I would like to thank my girlfriend Olivia Dinica. Her endless support, patience and understanding have helped me to get through graduate school. Through her, I have learned so much about the world, which will help me to be a good researcher in the future.

Isogeometric Analysis for Boundary Integral Equations

Publication No. _____

Matthias Franz Taus, Ph.D.
The University of Texas at Austin, 2015

Supervisor: Gregory J. Rodin
Co-Supervisor: Thomas J. R. Hughes

Since its emergence, Isogeometric Analysis (IgA) has initiated a revolution within the field of Finite Element Methods (FEMs) for two reasons: (i) geometry descriptions originating from Computer Aided Design (CAD) can be used directly for analysis purposes, and (ii) the availability of smooth exact geometry descriptions and smooth basis functions can be used to develop new, highly accurate and highly efficient numerical methods. Whereas in FEMs the first issue is still open, it has already been shown that Isogeometric BEMs (IBEMs) provide a complete design-through-analysis framework. However, in contrast to FEMs, the effect of smoothness provided by IgA has not yet been explored in IBEMs. In this dissertation, we address this aspect of IgA. We show that the smoothness and exactness properties provided by the IgA framework can be used to design highly accurate and highly efficient BEMs which are not accessible with conventional BEMs.

We develop Collocation IBEMs on piecewise smooth geometries. This allows us to show that IBEMs converge in the expected rates and result in system matrices with mesh-independent condition numbers. The latter property is particularly beneficial for large-scale problems that require iterative linear solvers. However, using conventional Collocation BEMs, this approach is not accessible because hyper-singular integrals have to be evaluated. In contrast, using Collocation IBEMs, the smoothness properties of the IgA framework can be used to regularize the hyper-singular integrals and reduce them to weakly singular integrals which can be evaluated using well-known techniques. We perform several numerical examples on canonical shapes to show these results. In addition, we use well-known mathematical results to develop a sound theoretical foundation to some of our methods, a result that is very rare for Collocation discretizations. Finally, using the exactness of IgA geometry descriptions, we design Patch Tests that allow one to rigorously test IBEM implementations. We subject our implementation to these Patch Tests which not only shows the reliability of our method but also shows that IBEMs can be as accurate as machine precision.

We apply our IBEMs to Laplace's equation and the equations of linear elasticity. In addition, input files for our implementation can be automatically obtained from commercial CAD packages. These practical aspects allow us to apply IBEMs to analyze a propeller under a wind load.

Table of Contents

Acknowledgments **v**

Abstract **vii**

List of Tables **xii**

List of Figures **xiv**

Chapter 1. Introduction **1**

1.1 Goals and problem statement 1
1.2 Isogeometric Analysis 2
1.3 Boundary Integral Equations 3
1.4 Main contributions 8
1.4.1 Convergence and conditioning properties 9
1.4.2 Collocation discretizations of hyper-singular BIEs 10
1.4.3 Adaption of numerical integration schemes 11
1.4.4 Patch Tests 12
1.4.5 Industrial example 12
1.5 Structure of this dissertation 13

Chapter 2. Isogeometric Analysis **16**

2.1 Classification of geometries 16
2.2 CAD geometry 16
2.3 Basis functions 19
2.4 Collocation points 20

Chapter 3. Laplace's equation **23**
3.1 Continuous Formulation 23
3.1.1 Model boundary-value problem 23
3.1.2 Integral equations 24
3.1.3 Analysis of integral equations 25
3.2 Collocation discretization 28
3.3 Regularization of operators 32
3.3.1 Integral operators on C^2-surfaces 33
3.3.2 Integral operators on $\tilde{C}^2$-surfaces 34
3.4 Numerical Integration 37
3.4.1 Evaluation of weakly-singular integrals 37
3.4.2 Evaluation of regular integrals 42
3.4.3 Integration over elements with high curvature or high aspect ratio 44
3.5 Numerical Examples 48
3.5.1 Overview 48
3.5.2 Recursive subdivision for near-singular integration . . . 52
3.5.3 Surface reparametrization scheme 53
3.5.4 Exponential convergence of the integration scheme . . . 56
3.5.5 Spectral properties of integral operators 58
3.5.5.1 Dirichlet problems 58
3.5.5.2 Mixed boundary-value problem 64
3.5.6 Discontinuous basis functions 65
3.5.7 Approximations for mixed boundary-value problems . . 69

Chapter 4. Equations of linear elasticity **75**
4.1 Introduction 75
4.2 Continuous Formulation 75
4.2.1 Model boundary-value problem 75
4.2.2 Integral equations 77
4.3 Collocation discretization 80
4.4 Regularization of operators 85

Chapter 5. Patch Tests for Boundary Element Methods **89**
5.1 Neumann Patch Test 89
5.2 Dirichlet Patch Test 91
5.3 Numerical examples 92
5.3.1 Overview 92
5.3.2 Neumann Patch Test 92
5.3.3 Dirichlet Patch Test on canonical shapes 93
5.4 Exterior Problems 94

Chapter 6. An industrial example **102**
6.1 Introduction 102
6.2 Compatibility with CAD Tools 102
6.3 A propeller under a wind load 104
6.3.1 Problem and CAD description 104
6.3.2 Patch Tests 105
6.3.3 Results 107

Chapter 7. Conclusion **111**

Appendices **115**

Appendix A. Compactness of integral operators **116**

Appendix B. Numerical evaluation of weakly singular integrals **119**

Bibliography **123**

Vita **139**

List of Tables

3.1 $L^2(\Gamma)$-errors for two near-singular integration schemes: with and without subdivision. 54

3.2 The manufactured pure Dirichlet BVP for the sphere: $L^2(\Gamma)$-errors for two singular integration schemes, with and without reparametrization. 55

3.3 The manufactured pure Dirichlet BVP for the sphere: $L^2(\Gamma)$-errors for two approaches, one based on the SBIE (dashed line) and the other based on the HSBIE (solid line). 57

3.4 Numerical integration $L^2(\Gamma)$-errors for the (a) torus (b) sphere, and (c) cube. 60

3.5 Iteration counts of the preconditioned GMRES method and condition numbers κ for the (a) torus (b) sphere, and (c) cube . . 63

3.6 Iteration counts of the preconditioned GMRES method for the (a) torus, (b) sphere, and (c) cube. 67

3.7 $L^2(\Gamma)$-errors for two approximations, with and without the discontinuous basis functions. 69

3.8 $L^2(\Gamma)$-errors for the flux t and potential u on the (a) torus (b) sphere, and (c) cube. The approximations involved continuous basis functions degree $p = 2$ for u and discontinuous basis functions of degree $p = 2$ for t. 72

3.9 $L^2(\Gamma)$-errors for the flux t and potential u on the (a) torus (b) sphere, and (c) cube. The approximations involved continuous basis functions degree $p = 3$ for u and discontinuous basis functions of degree $p = 2$ for t (solid lines). The dashed lines correspond to the results presented in Figure 3.12. 74

5.1 Neumann Patch Test for the (a) sphere and (b) spheroid. . . 94

5.2 Dirichlet Patch Test for the (a) sphere and (b) spheroid. . . . 95

5.3 Neumann Patch Test for oblate spheroidal voids in an infinite body. 98

5.4 Neumann Patch Test for prolate spheroidal voids in an infinite body. 99

5.5 Neumann Patch Test for oblate spheroidal voids in an infinite body. 100
5.6 Neumann Patch Test for prolate spheroidal voids in an infinite body. 101

List of Figures

2.1 Parametric and physical spaces for a torus. 18

2.2 Greville abscissae (large grey circles) and "2-ring" Greville abscissae (small black circles) for a single patch in (a) 1-D and (b) 2-D. Note that the abscissae coincide except for the patch boundaries. 22

3.1 Examples for the adaptive refinement technique for different locations of the collocation point with respect to the Bézier element. 45

3.2 Three representative shapes: (a) torus (inner radius $r = 1$ and outer radius $R = 3$), (b) sphere (radius $r = 1$), and (c) cube (edge length $a = 1$). The source points for the manufactured solutions: $x_0 = (0, 0, 60)$ for the torus, $x_0 = (0, 0, 20)$ for the sphere, and $x_0 = (1/2, 1/2, 15)$ for the cube. 49

3.3 Meshes for the first two refinement levels for the (a) torus, (b) sphere, and (c) cube. 50

3.4 $L^2(\Gamma)$-errors for two near-singular integration schemes: with and without subdivision. 53

3.5 The manufactured pure Dirichlet BVP for the sphere: $L^2(\Gamma)$-errors for two singular integration schemes, with and without reparametrization. 55

3.6 The manufactured pure Dirichlet BVP for the sphere: $L^2(\Gamma)$-errors for two approaches, one based on the SBIE (dashed line) and the other based on the HSBIE (solid line). 56

3.7 Numerical integration $L^2(\Gamma)$-errors for the (a) torus (b) sphere, and (c) cube. 59

3.8 Iteration counts of the preconditioned GMRES method and condition numbers κ for the (a) torus (b) sphere, and (c) cube . . 62

3.9 Mixed boundary conditions for the torus, sphere, and cube. . . 64

3.10 Iteration counts of the preconditioned GMRES method for the (a) torus, (b) sphere, and (c) cube. 66

3.11 $L^2(\Gamma)$-errors for two approximations, with and without the discontinuous basis functions. 68

3.12 $L^2(\Gamma)$-errors for the flux t and potential u on the (a) torus (b) sphere, and (c) cube. The approximations involved continuous basis functions degree $p = 2$ for u and discontinuous basis functions of degree $p = 2$ for t. 71

3.13 $L^2(\Gamma)$-errors for the flux t and potential u on the (a) torus (b) sphere, and (c) cube. The approximations involved continuous basis functions of degree $p = 3$ for u and discontinuous basis functions of degree $p = 2$ for t (solid lines). The dashed lines correspond to the results presented in Figure 3.12. 73

5.1 Neumann Patch Test for the (a) sphere and (b) spheroid. . . 93

5.2 Dirichlet Patch Test for the (a) sphere and (b) spheroid. . . . 95

5.3 Neumann Patch Test for oblate spheroidal voids in an infinite body. 97

5.4 Neumann Patch Test for prolate spheroidal voids in an infinite body. 98

5.5 Neumann Patch Test for oblate spheroidal voids in an infinite body. 99

5.6 Neumann Patch Test for prolate spheroidal voids in an infinite body. 100

6.1 The CAD geometry of the propeller. 105

6.2 The Bézier mesh of the propeller. 106

6.3 The Dirichlet boundary for the wind loading on the propeller. 107

6.4 The creased edges to define discontinuous basis functions. . . . 108

6.5 The deformed propeller exaggerated by a factor of 1000. The propeller is colored by the magnitude of the displacement and superimposed by the Bézier mesh of the original geometry. . . 109

6.6 The Von Mises Stress on the propeller. 110

B.1 The definition of the triangles used to define polar coordinate transformations centered at $\hat{t}$. 120

Chapter 1

Introduction

1.1 Goals and problem statement

This dissertation is concerned with combining numerical methods for boundary integral equations (BIEs) and Isogeometric Analysis (IgA). This combination is very appealing because BIEs can be defined and solved on surfaces generated via computer aided design (CAD), without any additional meshing or geometry reconstruction techniques. This feature can significantly shorten the design-through-analysis process for high-end engineering components. In contrast, IgA-based finite element (FE) methods require volumetric meshing.

Since CAD-generated surfaces are typically smooth, IgA allows for efficient and accurate numerical methods which exploit the smoothness. However, this important aspect of IgA has not been exploited in the context of BIEs. In fact, no effort has been made to (i) establish basic convergence and conditioning properties, and (ii) exploit the smoothness properties provided by IgA for the development of better numerical methods. These two themes are central to this dissertation.

For all practical purposes, CAD-generated surfaces are based on piecewise smooth parametrizations, even for smooth geometries. This severely effects the mathematical properties of BIEs defined on CAD-generated surfaces, and therefore numerical methods for solving BIEs defined on smooth surfaces must be augmented in order to be able to deal with CAD-generated surfaces. In this dissertation, we develop numerical schemes for handling irregularities associated with CAD parametrizations, and demonstrate the robustness of those schemes using numerical examples rather than mathematical proofs. All developments in this dissertation are restricted to boundary-value problems (BVPs) for either Laplace's equation or the equations of linear elasticity. Nevertheless, we believe that many results of this dissertation will be important for IgA of BIEs associated with other elliptic and non-elliptic BVPs.

1.2 Isogeometric Analysis

IgA [35, 57] is a framework for numerical schemes for solving BVPs in which the basis functions coincide with those used for geometric parametrizations in CAD. Thus, in contrast to conventional finite element methods, IgA relies on Non-Uniform Rational B-splines (NURBS) [76, 82], T-splines [93, 99] or subdivision surfaces [29, 86, 90] rather than piecewise polynomials as the basis functions.

IgA is advantageous because, in contrast to finite element methods (FEMs), it fully preserves the geometry of CAD-generated surfaces and involves basis

functions with attractive properties. These features have given rise to accurate and efficient numerical schemes successfully applied to fluid mechanics [1, 5, 7, 9, 10, 14, 43], solid mechanics [68], electromagnetism [28], fluid-structure interaction [11, 12, 13, 107], structural dynamics [36, 37], plates and shells [17, 18, 30, 31, 39, 42, 62], phase-field models [19, 49, 50], and shape optimization [72, 73, 78, 105].

These features have drawn a lot of attention from the scientific and industrial community and have triggered many new areas of research. However, the vast majority of IgA research has been done within the context of finite element discretizations but only little work has been done in the context of BIEs.

1.3 Boundary Integral Equations

BVPs for many partial differential equations can be reformulated as BIEs. Among others, those partial differential equations include Laplace's equation and equations of linear elasticity, which are of primary interest to this dissertation. Further, we restrict our attention to BIEs involving natural field variables (potential and flux or displacement and traction). Numerical methods for such BIEs are often referred to as direct boundary element methods (BEMs). Mathematical properties and numerical analysis of such methods have been studied in depth; see [55, 69, 71, 88, 103] and references therein.

Any numerical method for a BIE involves discretization and solution of a dense

linear algebraic system. The latter issue has been elegantly addressed with the introduction of fast BEMs [51, 83] which reduce the storage of the system matrices from $\mathcal{O}(N^2)$ to $\mathcal{O}(N)$ and the operations count to invert the system matrices from $\mathcal{O}(N^3)$ to $\mathcal{O}(N)$, here N is the problem size; for more details see [74] and the references therein. The discretization strategy is significantly dependent on the smoothness of the geometry and field variables. For smooth problems, it is advantageous to use Nyström discretizations[26, 53, 64, 106], while Galerkin discretizations can be exploited for non-smooth problems. In the engineering community of BEMs, Collocation discretizations are often used instead of Galerkin discretizations because they deliver similarly accurate solutions but are more efficient. However, Collocation discretizations can only be applied to a restrictive class of BIEs and consequently result in sub-optimally conditioned system matrices. In addition, mathematical foundations can only be established for a very restrictive classes of Collocation BEMs [2, 33, 34, 56, 87].

In this regard, the piecewise smooth approximations provided by IgA, on the one hand, are insufficiently smooth for Nyström discretizations, and, on the other hand, make Collocation discretizations accessible for a larger class of BIEs which allows for the development of Collocation discretizations that result in optimally conditioned system matrices. Further, a sound mathematical foundation can be established for IgA-based Collocation discretizations of certain BIEs defined on smooth surfaces. As a result, in this dissertation, we focus

on collocation discretizations, well suited for piecewise smooth approximations of IgA.

Conventional Galerkin and Collocation discretizations of BIEs involve globally continuous piecewise polynomial approximations of the surface defined on a user-generated mesh. Since essentially any practically relevant surface can be approximated by piecewise polynomials, this approach provides a lot of flexibility and is very attractive for problems involving complex non-smooth geometries. However, this approach has two major disadvantages: (i) user-generated meshes for complex geometries are often very hard to obtain and most of the time cannot be obtained directly from CAD surface descriptions, and (ii) the use of globally continuous piecewise polynomial approximations does not preserve the possible smoothness of the exact geometry. The latter is especially disadvantageous because approximations of the geometry severely affect the accuracy of BEMs and the lack of smoothness of the geometry does not allow for the development of Collocation discretization resulting in well-conditioned system matrices. Consequently, Collocation and Galerkin discretizations usually result in extremely reliable but sub-optimal numerical methods in view of efficiency and accuracy.

Conventional Nyström discretizations rely on smooth parametrizations of the surfaces. In this context, numerical methods have been developed that exploit

the smoothness of the parametrization for approximation and integration purposes [4, 26, 27, 79, 106]. On C^∞ surface parametrizations, these methods are extremely efficient and accurate and consequently superior to Galerkin or Collocation discretizations. Furthermore, they can be extended to C^k surface parametrizations for $k \geq 1$ and therefore seem to be the optimal choice for BIE defined on smooth CAD-generated surfaces. However, only a very small class of CAD-generated surfaces results in globally smooth surface parametrizations. An arbitrary CAD surface usually involves extraordinary points or points with zero Jacobians. In either case, the surface parametrization is only C^0. In this case, a direct application of Nyström discretizations developed for smooth surfaces does not result in a reliable or efficient numerical method because the efficiency and accuracy of Nyström discretizations heavily relies on the global smoothness of the surface parametrization. This issue can be addressed by the surface reconstruction technique developed in [24]. In this case, a point cloud can be automatically obtained from the CAD-generated surface and then used to obtain a smooth surface parametrization on which Nyström discretizations can be applied efficiently. However, there are subtle caveats to this approach. While the approximations of the surfaces obtained from the reconstruction technique converge spectrally to the exact geometry and preserve the optimal convergence of the Nyström method, their accuracy depends on the choice of the point cloud resulting in a not completely automatic procedure. In addition, while the surface reconstruction technique converges rapidly to the exact geometry, it does not represent the original geometry exactly. In

this regard, while spectrally accurate, this approach can be less accurate than methods based on exact geometry descriptions, especially for very coarse discretizations. Alternatively, one can directly work with the piecewise smooth CAD surface parametrization of the smooth geometry. However, in this case, new Nyström discretizations have to be developed for piecewise smooth surface parametrizations. This could be addressed in the same way as piecewise smooth surfaces involving sharp edges and corners for which some work has been done in the context of Nyström discretizations [20, 22, 23, 25, 54, 65]. However, all of these approaches are for two-dimensional problems only and no reliable approach has been found for the treatment of non-smooth surface parametrizations for three-dimensional problems.

Existing IgA-based BEMs [15, 16, 48, 67, 75, 77, 94, 100] have shown that IgA allows for the direct use of (exact) CAD-generated geometries in BEMs. However, the proposed methods are essentially the same Collocation and Galerkin methods defined on piecewise polynomial surfaces and do not exploit any additional smoothness properties provided by IgA. In fact, while these methods have been successfully applied to many engineering problems, no theoretical foundation has been established for these methods and their convergence and conditioning properties are still unknown.

1.4 Main contributions

In this dissertation we combine IgA with BEMs resulting in isogeometric BEMs (IBEMs). The proposed approach can be classified as a direct high-order collocation BEM allowing for weakly-singular, singular, and hypersingular integral operators. Previously this setting was possible with Galerkin but not collocation methods. Accordingly, we exploited analytical tools different from those usually used in analysis of Galerkin methods [88, 103]. In this regard, we believe that our approach may be useful for developing mathematical foundations for collocation schemes for BIEs. We believe that our approach not only successfully addresses the lack of appropriate geometry descriptions in conventional BEMs while preserving the same flexibility as piecewise polynomial geometry approximations, but also exploits the smoothness of the geometry and the basis functions for the development of new more accurate and more efficient BEMs in the same spirit as Nyström discretizations on C^∞ surfaces.

While the proposed numerical methods allow for a direct use of CAD-generated surfaces and exploit the smoothness provided by these surface descriptions, the main focus of this dissertation is on reliability rather than efficiency of the developed methods. In particular, the proposed numerical integration schemes for the evaluation of the BIEs heavily rely on well-established schemes developed for piecewise polynomial surface parametrizations and no effort is made in developing more appropriate numerical integration schemes for piece-

wise smooth surfaces. While our methods can reliably treat arbitrary CAD-generated surfaces resulting in optimally convergent methods, their efficiency is not comparable to the efficiency of Nyström discretizations on smooth surfaces.

The main contributions of this dissertation include the establishment of convergence and conditioning properties of IgA-based Collocation BEMs defined on smooth or piecewise smooth CAD-generated surfaces, the development of Collocation discretizations for hyper-singular BIEs in the context of IgA, the sophistication of existing numerical integration techniques for singular functions and their adaptation for IBEMs, the introduction of Patch Tests for BEMs, and the consideration of an industrial example for IBEMs. In what follows we provide details for each of those contributions.

1.4.1 Convergence and conditioning properties

Convergence and conditioning properties of IBEMs cannot be found in the literature, neither a mathematical analysis nor numerical examples have been considered to reveal these properties. In this dissertation, we reveal these properties for smooth surfaces by providing a mathematical analysis and numerical examples, and for non-smooth surfaces by providing numerical examples. The mathematical analysis is based on well-established mathematical properties of boundary integral operators and can be applied to pure Dirichlet or pure Neumann BVPs. Numerical examples for pure Dirichlet, pure Neu-

mann and mixed BVPs are considered on three geometries, each representing a class of geometry parametrization. The torus represents a smooth geometry with a smooth CAD surface parametrization, the sphere represents a smooth geometry with a non-smooth CAD surface parametrization, and the cube represents a non-smooth geometry with a non-smooth CAD surface parametrization. These examples reveal that in each case IBEMs converge in optimal rates as long as the basis functions are chosen appropriately. Furthermore, numerical examples suggest that for the proposed methods, the conditioning of the resulting system matrices depends on the smoothness of the geometry and the type of the boundary conditions. For smooth geometries and either pure Dirichlet or pure Neumann boundary conditions, the conditioning of the system matrices is independent of the mesh-size, while for any other combination of boundary conditions or geometry smoothness the condition numbers grow logarithmically with the mesh-size. This is an improvement over conventional Collocation BEMs which often result in system matrices whose condition numbers grow linearly with the mesh-size, even for smooth geometries.

1.4.2 Collocation discretizations of hyper-singular BIEs

Conventional Collocation discretizations are usually only applied to singular but not hyper-singular BIEs. This is mainly because the numerical evaluation of hyper-singular integrals is problematic. Some techniques have been proposed to numerically evaluate hyper-singular integrals. Those include a regularization technique that reduces the evaluation of the hyper-singular

integral to the evaluation of weakly-singular integrals only. However, numerical examples for this technique are only provided for two-dimensional problems. In this dissertation, we provide explicit formulas on how to apply this regularization technique to three-dimensional problems and rigorously prove that all hyper-singular integrals reduce to weakly singular ones. Furthermore, we provide several numerical examples for three-dimensional problems which show the accuracy of this approach in the context of IgA. Furthermore, we show that the accessibility of hyper-singular integral equations for collocation discretizations can be used to develop methods that result in system matrices whose condition numbers grow at most logarithmically with the mesh size (see Section 1.4.1).

1.4.3 Adaption of numerical integration schemes

We show that existing integration techniques for piecewise smooth surfaces can be adapted for IBEMs and are very reliable and sufficiently accurate for CAD-generated surfaces that do not involve (i) points with a vanishing Jacobian, and (ii) elements with high curvature or aspect ratio. We address both issues by refining existing integration techniques. A local reparametrization technique is employed in the vicinity of points with a vanishing Jacobian in order to regularize weakly singular integrals and preserve the accuracy and efficiency of existing numerical integration schemes for weakly singular integrals. Elements with high curvatures or aspect ratios are addressed by introducing a suitable adaptive subdivision technique. These developments allow for a very

reliable and accurate evaluation of all integrals considered in this dissertation.

1.4.4 Patch Tests

Patch Tests are ubiquitous in finite element methods but have not been developed for BEMs. In finite element methods, Patch Tests are based on the solution of BVPs whose exact solutions are global polynomials. Tests of the exact recovery of these polynomials are commonly known as Patch Tests. In this dissertation, we extend this notion to BEMs. Similar to finite element methods, BEM Patch Tests can be used to (i) test the correctness of a BEM implementation, and (ii) provide information about the accuracy of the numerical solution. In particular, BEM Patch Tests allow one to rigorously control the numerical integration error on complex geometries to an extend that it becomes negligible. This is of immense practical value because controlling the error of the numerical evaluation of singular integrals defined on arbitrary complex (curved) geometries is not trivial.

1.4.5 Industrial example

All numerical methods developed in this dissertation involve CAD-generated surfaces based on T-splines. The well-known commercial software package Rhinoceros$^{\text{TM}}$(Rhino) can be combined with the T-Splines$^{\text{TM}}$plug-in in order to handle such surfaces. In addition, these packages allow one to automatically generate input files for our IBEM code. Consequently, arbitrary T-spline geometries generated in this environment can be automatically used

for a BEM analysis. We show this feature by simulating a wind load on a propeller. We do this by first obtaining confidence in the employed integration scheme for the considered IBEM is obtained by employing a Patch Test. Then the proper integration scheme is used to compute a solution for the wind loading problem.

1.5 Structure of this dissertation

In Chapter 2, we briefly introduce the main concepts of IgA. We introduce geometry parametrizations, basis functions, and collocation points.

In Chapter 3, we introduce IBEMs for Laplace's equation. We define the model BVP, corresponding BIEs, and a proper continuous setting for BVPs defined on domains with smooth boundaries. We introduce collocation schemes for the integral operators defined on smooth surfaces, and demonstrate that all collocated integral operators defined on smooth surfaces can be reduced to weakly-singular integrals. We then describe the extension of our methodology to piecewise smooth surfaces which allows us to accommodate multiple patches with C^0-continuity, degenerate patches resulting in local C^0-continuity, and extraordinary points or star-points. We conclude the chapter by considering representative example problems, which allow us to demonstrate various important mathematical and computational aspects of our IBEMs.

In Chapter 4, we extend the results for Laplace's equation to the equations of

linear elasticity. We define the model BVP and corresponding BIEs on piecewise smooth boundaries. We introduce collocation schemes for the integral operators and demonstrate that all collocated integral operators defined on piecewise smooth surfaces can be reduced to weakly singular integrals.

In Chapter 5, we develop Patch Tests. We introduce the theoretical background for Patch Tests based on pure Neumann and pure Dirichlet interior BVPs, and comment on the extension to other BVPs, e.g. mixed BVPs. Numerical examples are considered for both Neumann and Dirichlet Patch Tests and confirm the robustness of our IBEM implementation. Finally, we extend Patch Tests to exterior BVPs and apply them to spheroidal voids in an infinite body. These problems show that IBEMs deliver solutions up to machine precision, independently of the aspect ratio of the spheroids.

In Chapter 6, we analyze a CAD-generated propeller under a wind load. We show the compatibility of our IBEMs with commercial CAD packages and describe a procedure to use CAD geometries directly in our IBEM implementation. We use this procedure and begin the analysis by first considering Patch Tests on the propeller geometry in order to assess the reliability of our approach. A high confidence is obtained from this consideration and results for the wind load are presented.

In Chapter 7, we we summarize key results of this work and briefly discuss

directions for future research. Mathematical details are presented in the appendix.

Chapter 2

Isogeometric Analysis

2.1 Classification of geometries

Consider a bounded domain $\Omega \subset \mathbb{R}^3$ with $\Gamma := \partial\Omega$. In this dissertation, Γ is either a C^2-surface or a piecewise C^2-surface. Loosely speaking, a C^2-surface Γ ($\Gamma \in C^2$) is such that Γ can be mapped on $\mathbb{R}^2$, and the inverse of that map ψ is twice continuously differentiable. For a rigorous definition of C^2-surfaces we refer to the appendix. However, a typical CAD generated surface is not C^2 but rather a union of C^2-surfaces, resulting in a globally Lipschitz Γ; we denote this class of surfaces by $\tilde{C}^2$.

2.2 CAD geometry

In IgA it is presumed that the surface Γ is described using a CAD tool. Invariably those descriptions rely on B-splines. A one-dimensional B-spline of degree p is a piecewise polynomial function of degree p. The smoothness between polynomials can be controlled locally and can be up to C^{p-1}. Thus, if desired, one can construct a B-spline of degree p, which is C^{p-1} globally. Multi-dimensional B-splines are constructed as tensor products of one-dimensional B-splines. T-splines are constructed as linear combinations of B-splines without

the need for the tensor-product structure. This feature is very attractive, as it allows local refinement with hanging nodes, and therefore we use T-splines. For further details on T-splines we refer to [93, 94].

First, let us assume that Γ can be mapped on a rectangular parametric domain $\hat{\Gamma} \subset \mathbb{R}^2$. In CAD the map $\varphi : \hat{\Gamma} \to \Gamma$ is constructed in terms of a set of control points $P_A \in \mathbb{R}^3$, weights $w_A > 0$, and T-splines $\hat{N}_A^T$ defined on $\hat{\Gamma}$:

$$x = \varphi(\xi_1, \xi_2) := \frac{\sum_A P_A w_A \hat{N}_A^T(\xi_1, \xi_2)}{\sum_B w_B \hat{N}_B^T(\xi_1, \xi_2)} \quad (\xi_1, \xi_2) \in \hat{\Gamma}. \tag{2.1}$$

This map has numerous advantages over the simpler map $\sum_A P_A \hat{N}_A^T(\xi_1, \xi_2)$. In particular, it can represent quadric surfaces exactly. Further, since T-splines $\hat{N}_A^T$ are a superset of B-splines, the map (2.1) can be restricted to NURBS, which are currently an industrial standard. Note that in principle the map smoothness can be controlled by choosing appropriately smooth T-splines. However, in practice it is standard to set $p = 3$ and use C^2 T-splines, so that $\varphi \in C^2(\hat{\Gamma})$. By adopting a global definition for the map $\psi := \varphi$, we conclude that Γ defined by φ is a C^2-surface.

The map defined in (2.1) requires a rectangular $\hat{\Gamma}$ and therefore it is rather limited. For example, it cannot be used for constructing a cube. In the context of NURBS, this issue is usually addressed by allowing the parametric domain to consist of multiple rectangular patches. This creates a new host of problems associated with imposing continuity conditions across patches. This issue is

naturally resolved with T-splines, as they allow for hanging nodes and smooth basis functions across patches. Nevertheless, even with T-splines, one has to address extraordinary points. By definition, those points are intersections of three or more than four patches. At extraordinary points, the parametrization map φ is only C^0, and as a result $\Gamma \in \tilde{C}^2$. For details we refer to [94]. Another way of generalizing (2.1) is by allowing rectangles to be mapped on triangles by collapsing edges. This approach involves two ingredients: (i) in the parametric domain, all T-splines, supported on the edge to be collapsed, are constructed as C^0 functions across the edge, and (ii) control points corresponding to T-splines supported on the edge to be collapsed are assigned to the same position. Like the treatment of extraordinary points, this construction yields locally C^0-parametrizations. Thus generalized maps, involving multiple rectangular patches, give rise to $\Gamma \in \tilde{C}^2$.

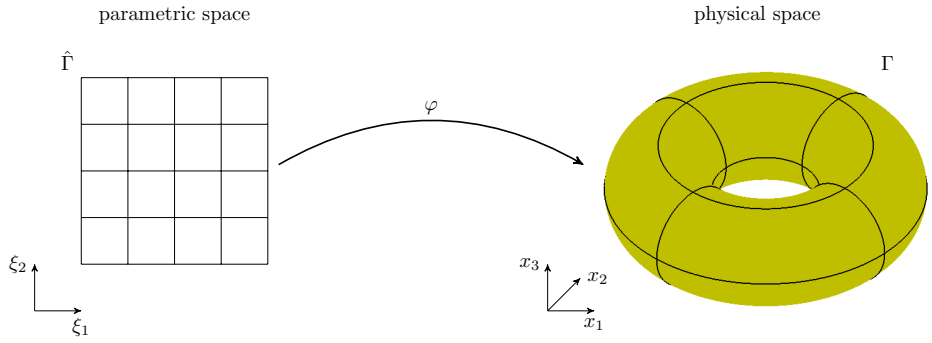

Figure 2.1: Parametric and physical spaces for a torus.

2.3 Basis functions

Let us suppose that control points P_A, weights w_A, and T-splines $\hat{N}_A^T$, prescribing Γ via (2.1) are given. Then in the parametric domain the basis functions are constructed using the partition of unity

$$\hat{N}_A(\xi_1, \xi_2) := \frac{w_A \hat{N}_A^T(\xi_1, \xi_2)}{\sum_{B=1}^{n} w_B \hat{N}_B^T(\xi_1, \xi_2)} \,. \tag{2.2}$$

The basis functions N_A in the physical domain Γ are constructed via the standard map

$$N_A := \hat{N}_A \circ \varphi^{-1} \,. \tag{2.3}$$

This construction includes extraordinary points but not collapsed edges. For the latter cases, the basis functions $\hat{N}_{A'}$ supported on a collapsed edge are replaced by a single basis function

$$\hat{N} = \sum_{A'} \hat{N}_{A'} \,.$$

After that, the corresponding basis function N is constructed via (2.3). Note that in our work, both extraordinary points and collapsed edges give rise to basis functions which are locally C^2 but globally continuous. For extraordinary points, one could use a constrained optimization framework that gives rise to C^1-basis functions; for details see [94].

For solving BIEs, one also needs discontinuous basis functions for approximating Neumann data, which can be discontinuous and even singular even if

$\Gamma \in C^2$ and prescribed Cauchy data are smooth. It is straightforward to define discontinuous T-splines $\hat{N}_A^{T,\text{disc}}$. However, CAD parametrizations involve the weights for continuous T-splines only. While, in principle, one can compute the weights for discontinuous T-splines, and then use (2.2), we adopt a simpler construction involving unweighted scaled basis functions:

$$\hat{N}_A(\xi_1, \xi_2) := \frac{\hat{N}_A^{T,\text{disc}}(\xi_1, \xi_2)}{\sum_{B=1}^{n} w_B \hat{N}_B^T(\xi_1, \xi_2)} \,. \tag{2.4}$$

The scaling by $\left[\sum_{B=1}^{n} w_B \hat{N}_B^T(\xi_1, \xi_2)\right]^{-1}$ is motivated by numerical examples rather than theory. The construction in (2.4) is not a partition of unity, but this property is not required for analysis of BIEs.

2.4 Collocation points

The Greville abscissa of a B-spline is a point in the parametric domain $\hat{\Gamma}$ whose coordinates are defined as the average of the coordinates of the knots. These points often correspond to the maximum value of the B-spline. It has been shown that they are ideally suited for interpolation and that they can be naturally extended to T-splines. Further, Greville abscissae have been widely used as collocation points for the basis functions (2.3) in various numerical methods [6, 8, 89], including those for BIEs [67, 94, 100, 101]. However, it has been recognized [94] that for discontinuous T-splines Greville's abscissae may coincide, and therefore one needs to modify the construction. This issue has been addressed by introducing "2-ring" collocation points [94] for discontinuous cubic T-splines.

In this work, we generalize the definition of the "2-ring" collocation points to T-splines of degree p. To this end, let us consider a one-dimensional B-spline $B(\xi)$ of degree p with $a \leq \xi \leq b$. If $B(\xi) \in C([a,b])$, then the "2-ring" collocation point is simply the Greville abscissa. If $B(\xi)$ is discontinuous at $\xi = a$ then the "2-ring" collocation point is

$$\xi_{2-ring} := a + \frac{b-a}{p+2};$$

if the discontinuity is at $\xi = b$, then

$$\xi_{2-ring} := b + \frac{a-b}{p+2}.$$

To construct the collocation point for a two-dimensional discontinuous T-spline, we can exploit that locally (rather than globally) T-splines are tensor products of one-dimensional B-splines. Therefore once a two-dimensional discontinuous T-spline is represented by $T_{ij}(\xi_1, \xi_2) = B_i(\xi_1)B_j(\xi_2)$, one can find the coordinates of the "2-ring" collocation point by treating $B_i(\xi_1)$ and $B_j(\xi_2)$ separately.

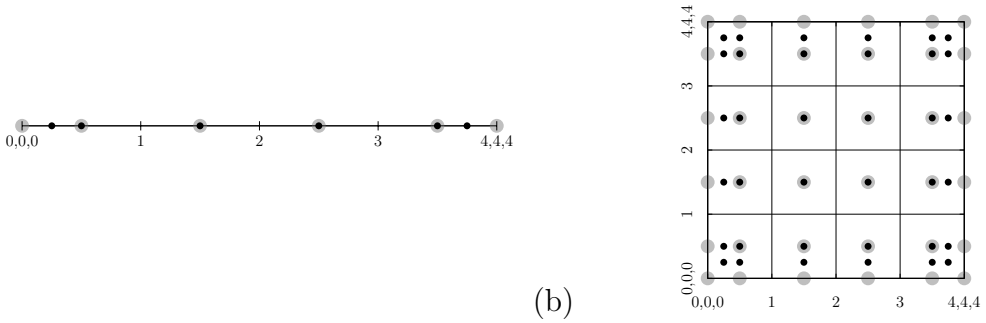

(a) (b)

Figure 2.2: Greville abscissae (large grey circles) and "2-ring" Greville abscissae (small black circles) for a single patch in (a) 1-D and (b) 2-D. Note that the abscissae coincide except for the patch boundaries.

Chapter 3

Laplace's equation

3.1 Continuous Formulation

3.1.1 Model boundary-value problem

Consider a bounded domain $\Omega \subset \mathbb{R}^3$ with $\Gamma := \partial\Omega$. We assume that $\Gamma \in C^2$. This restriction is sufficient for establishing mathematical foundations for integral equations. Unfortunately, mathematical foundations for BIEs defined on $\tilde{C}^2$-surfaces are not well developed at this stage. Thus, in this and the two following sections, we restrict our attention to $\Gamma \in C^2$. On the other hand, the loss of smoothness of $\tilde{C}^2$-surfaces can be compensated by using appropriate numerical schemes presented in Sections 3.4 and 3.5.

The model BVP is formulated for Laplace's equation

$$-\Delta u = 0 \quad \text{in } \Omega, \tag{3.1}$$

and mixed boundary conditions, which include Dirichlet

$$u = g_D \quad \text{on } \Gamma_D, \tag{3.2}$$

and Neumann

$$t := n \cdot \nabla u = g_N \quad \text{on } \Gamma_N \tag{3.3}$$

data. Here n denotes the outward unit normal vector on Γ; $\overline{\Gamma_D \cup \Gamma_N} = \Gamma$ and $\Gamma_D \cap \Gamma_N = \emptyset$. At this stage, we require $\Gamma \in C^2$, but we do not specify the smoothness of u, g_D, and g_N. This will be done once we introduce the integral operators.

3.1.2 Integral equations

The integral equations equivalent to (3.1)-(3.3) and their mathematical properties are well known [55, 88, 103]. They involve the representation formula that allows one to determine the solution u in terms of the Cauchy boundary data (u, t):

$$u(x) = \int_\Gamma G(x,y)t(y)ds_y - \int_\Gamma n(y) \cdot [\nabla_y G(x,y)]\, u(y)ds_y \quad x \in \Omega\,, \tag{3.4}$$

where

$$G(x,y) = \frac{1}{4\pi|x-y|}$$

is the fundamental solution of Laplace's equation. The Cauchy data can be reconstructed using the singular boundary integral equation (SBIE)

$$\left(\frac{1}{2}\mathcal{I} + \mathcal{K}\right) u = \mathcal{V}t \quad \text{on } \Gamma\,.$$

Here $\mathcal{I}$ is the identity,

$$\mathcal{V}t(x) := \int_\Gamma G(x,y)t(y)ds_y, \quad x \in \Gamma$$

is the single-layer operator, and

$$\mathcal{K}u(x) := \int_\Gamma n(y) \cdot [\nabla_y G(x,y)]\, u(y)ds_y, \quad x \in \Gamma$$

is the double-layer operator. Alternatively, the Cauchy data can be reconstructed using the hyper-singular integral equation (HSBIE)

$$\left(\frac{1}{2}\mathcal{I} - \mathcal{K}'\right) t = \mathcal{D}u \quad \text{on } \Gamma\,,$$

where

$$\mathcal{K}'t(x) := \int_\Gamma n(x) \cdot [\nabla_x G(x,y)]\, t(y) ds_y, \quad x \in \Gamma$$

is the adjoint double-layer operator, and

$$\mathcal{D}u(x) := -\int_\Gamma n(x) \cdot \{\nabla_x n(y) \cdot [\nabla_y G(x,y)]\}\, u(y) ds_y, \quad x \in \Gamma$$

is the hyper-singular operator.

3.1.3 Analysis of integral equations

Since $\Gamma \in C^2$ one can prove that the operators

$$\mathcal{K}, \mathcal{K}' : C(\Gamma) \to C(\Gamma)$$

are compact; see Appendix. Here $C(\Gamma)$ is the space of continuous functions on Γ. Similarly, we adopt the same convention for other spaces such as $C^2(\Gamma)$ which is the space of twice continuously differentiable functions on Γ. As a consequence of the compactness, Fredholm's alternative implies that the operators

$$\left(\frac{1}{2}\mathcal{I} + \mathcal{K}\right) : C_*(\Gamma) \to C_{**}(\Gamma), \quad \text{and} \quad \left(\frac{1}{2}\mathcal{I} - \mathcal{K}'\right) : C(\Gamma) \to C(\Gamma)$$

are invertible. Here $C_*(\Gamma)$ is the space of all functions $u \in C(\Gamma)$ with

$$\int_\Gamma u(y) ds_y = 0 \,,$$

and $C_{**}(\Gamma)$ is the space of all functions $u \in C(\Gamma)$ with

$$\int_\Gamma u(y) w_{eq}(y) ds_y = 0 \,,$$

where $w_{eq} = \mathcal{V}^{-1}1$ is the natural weight, which has been used in analysis of the hyper-singular operator [103]. Further, compactness of $\mathcal{K}$ and $\mathcal{K}'$ implies that the SBIE and HSBIE should be solved by inverting $\frac{1}{2}\mathcal{I} + \mathcal{K}$ and $\frac{1}{2}\mathcal{I} - \mathcal{K}'$, respectively.

For the pure Neumann BVP, the SBIE takes the form

$$\left(\frac{1}{2}\mathcal{I} + \mathcal{K}\right) u = \mathcal{V} g_N \quad \text{on } \Gamma. \tag{3.5}$$

Since $\mathcal{V} : C(\Gamma) \to C(\Gamma)$ and the boundary data g_N must satisfy the solvability condition

$$\int_\Gamma g_N(x) ds_x = 0 \,,$$

it follows that $g_N \in C(\Gamma)$ implies $\mathcal{V} g_N \in C_{**}(\Gamma)$. Therefore, the invertibility of $\left(\frac{1}{2} I + \mathcal{K}\right)$ implies that (3.5) has a unique solution for $u \in C_*(\Gamma)$.

For the pure Dirichlet BVP, the HSBIE takes the form

$$\left(\frac{1}{2}\mathcal{I} - \mathcal{K}'\right) t = \mathcal{D} g_D \quad \text{on } \Gamma. \tag{3.6}$$

One can prove that $g_D \in C^2(\Gamma)$ implies $\mathcal{D}g_D \in C(\Gamma)$. Thus the invertibility of $\left(\frac{1}{2}\mathcal{I} - \mathcal{K}'\right)$ implies that (3.6) has a unique solution for $t \in C(\Gamma)$.

Based on the analysis of the pure BVPs, it is appropriate to require $g_D \in C^2(\Gamma_D)$ and $g_N \in C(\Gamma_N)$ for the mixed BVP. These restrictions, however, do not guarantee $u \in C^2(\Gamma)$ and $t \in C(\Gamma)$. To formulate the BIEs corresponding to the mixed BVP, we define extensions $\tilde{g}_D \in C^2(\Gamma)$ and $\tilde{g}_N \in C(\Gamma)$, and express the Cauchy data as

$$u = \tilde{u} + \tilde{g}_D \quad \text{and} \quad t = \tilde{t} + \tilde{g}_N \,. \tag{3.7}$$

By construction, $\tilde{u}|_{\Gamma_D} = 0$ and $\tilde{t}|_{\Gamma_N} = 0$. Now we can rewrite the SBIE and HSBIE as the equations for $\tilde{u}$ and $\tilde{t}$:

$$\mathcal{V}\tilde{t} - \left(\frac{1}{2}\mathcal{I} + \mathcal{K}\right)\tilde{u} = \left(\frac{1}{2}\mathcal{I} + \mathcal{K}\right)\tilde{g}_D - \mathcal{V}\tilde{g}_N \quad \text{on } \Gamma, \tag{3.8}$$

and

$$\left(\frac{1}{2}\mathcal{I} - \mathcal{K}'\right)\tilde{t} - \mathcal{D}\tilde{u} = \mathcal{D}\tilde{g}_D - \left(\frac{1}{2}\mathcal{I} - \mathcal{K}'\right)\tilde{g}_N \quad \text{on } \Gamma \,. \tag{3.9}$$

Note that while $\tilde{g}_D$ and $\tilde{g}_N$ are not uniquely defined, the structure of (3.8) and (3.9) is such that u and t are uniquely defined as long as (3.8) and (3.9) are uniquely solvable for $\tilde{u}$ and $\tilde{t}$. Since $\tilde{g}_D \in C^2(\Gamma)$ and $\tilde{g}_N \in C(\Gamma)$, the right-hand sides of both equations are in $C(\Gamma)$. However, this is insufficient for establishing unique solvability for (3.8) and (3.9), under the provisions $\tilde{u} \in C^2(\Gamma)$ and $\tilde{t} \in C(\Gamma)$.

Remark 3.1.1. *It is straightforward to extend our analysis to the pure Robin BVP in which the boundary data are prescribed as*

$$t + \kappa u = g_R \quad on\ \Gamma\,,$$

where $\kappa \in L^\infty(\Gamma)$ *and* g_R *is a prescribed function in* $C(\Gamma)$*. This problem is similar to the pure Neumann problem.*

Remark 3.1.2. *The regularity requirements on* Γ*,* g_D *and* g_N *can be slightly relaxed. The results of this section can be extended to continuously differentiable* Γ*,* g_D *with Lipschitz continuous derivatives, and* $g_N \in L^\infty$*.*

Remark 3.1.3. *While it appears that the condition* $\tilde{g}_D \in C^2(\Gamma)$ *is too restrictive, in practice* g_D *is often a constant. For example, in the context of heat conduction, Dirichlet boundary conditions represent a situation in which* Ω *is placed in a constant-temperature environment whose temperature is not affected by* Ω*. If it is the case, a constant* g_D *is simply extended to the entire boundary, so that* $\tilde{g}_D$ *is constant.*

3.2 Collocation discretization

Let us consider the mixed BVP. Approximations for $\tilde{u}$ and $\tilde{t}$ are constructed as

$$\tilde{u}_h(x) = \sum_{A=1}^{n^D} \underline{\tilde{u}}[A] N_A^D(x), \quad \text{and} \quad \tilde{t}_h(x) = \sum_{A=1}^{n^N} \underline{\tilde{t}}[A] N_A^N(x)\,,$$

respectively, where $N_A^D(x)$ and $N_A^N(x)$ are the basis functions and $\underline{\tilde{u}}$ and $\underline{\tilde{t}}$ are column-vectors. Since $\tilde{u}(x) = 0$ for $x \in \Gamma_D$ and $\tilde{t}(x) = 0$ for $x \in \Gamma_N$, the basis functions are such that $N_A^D(x) = 0$ for $x \in \Gamma_D$ and $N_A^N(x) = 0$ for $x \in \Gamma_N$. Accordingly, we define collocation points x_A^D on Γ_N and x_A^N on Γ_D. This assignment of the superscripts may be somewhat confusing, but it simply reflects the fact that the basis functions $N_A^D(x)$ and $N_A^N(x)$ are supported on Γ_N and Γ_D, respectively.

Upon collocating (3.8) at x_A^D and (3.9) at x_A^N, one generates the system of linear algebraic equations for $\underline{\tilde{u}}$ and $\underline{\tilde{t}}$:

$$V\underline{\tilde{t}} - \left(\frac{1}{2}I_D + K\right)\underline{\tilde{u}} = \underline{f}_S \tag{3.10}$$

and

$$\left(\frac{1}{2}I_N - K'\right)\underline{\tilde{t}} - D\underline{\tilde{u}} = \underline{f}_H \,. \tag{3.11}$$

Here the components of the system matrices are defined as

$$
\begin{aligned}
V[A,B] &:= \mathcal{V}N_B^N(x_A^D) = \int_{\Gamma_D} G(x_A^D, y) N_B^N(y) ds_y \,, \\
I_D[A,B] &:= N_B^D(x_A^D) \,, \\
K[A,B] &:= \mathcal{K}N_B^D(x_A^D) \\
&= \int_{\Gamma_N} n(y) \cdot [\nabla_y G(x_A^D, y)] N_B^D(y) ds_y \,, \\
I_N[A,B] &:= N_B^N(x_A^N) \,, \\
K'[A,B] &:= \mathcal{K}'N_B^N(x_A^N) \\
&= \int_{\Gamma_D} n\left(x_A^N\right) \cdot [\nabla_x G(x_A^N, y)] N_B^N(y) ds_y \,, \\
D[A,B] &:= \mathcal{D}N_B^D(x_A^N) \\
&= -\int_{\Gamma_N} n\left(x_A^N\right) \cdot \left\{\nabla_x \left[n(y) \cdot \nabla_y G(x_A^N, y)\right]\right\} N_B^D(y) ds_y \,.
\end{aligned}
\tag{3.12}
$$

The right-hand-side vectors are defined as

$$
\begin{aligned}
\underline{f}_S[A] &:= \frac{1}{2}\tilde{g}_D(x_A^D) + \mathcal{K}\tilde{g}_D(x_A^D) - \mathcal{V}\tilde{g}_N(x_A^D) \,, \\
\underline{f}_H[A] &:= \mathcal{D}\tilde{g}_D(x_A^N) - \frac{1}{2}\tilde{g}_N(x_A^N) + \mathcal{K}'\tilde{g}_N(x_A^N) \,.
\end{aligned}
$$

For the pure Neumann BVP, all collocation points are x_A^D, and therefore it is sufficient to solve (3.10) by setting $\tilde{t}_h = 0$, $\tilde{g}_D = 0$, and $\tilde{g}_N = g_N$:

$$
-\left(\frac{1}{2} I_D + K\right) \underline{\tilde{u}} = \underline{f}_S. \tag{3.13}
$$

The compactness of $\mathcal{K}$ can be used to show that (3.13) is uniquely solvable as long as

$$
\int_\Gamma \tilde{u}_h(x) ds_x = 0 \,. \tag{3.14}
$$

Furthermore, under condition (3.14), $\tilde{u}_h$ converges to the exact solution u of (3.5) at optimal rates.

For the pure Dirichlet BVP, all collocation points are x_A^N, and therefore it is sufficient to solve (3.11) by setting $\tilde{u}_h = 0$, $\tilde{g}_N = 0$, and $\tilde{g}_D = g_D$:

$$\left(\frac{1}{2} I_N - K'\right) \underline{\tilde{t}} = \underline{f}_H \,. \tag{3.15}$$

The compactness of $\mathcal{K}'$ can be used to show that (3.15) is uniquely solvable and $\tilde{t}_h$ converges to the exact solution t of (3.6) at optimal rates.

Remark 3.2.1. *It is straightforward to extend the collocation scheme to the pure Robin BVP following the prescription for the Neumann BVP. Also, for the pure Robin BVP, unique solvability and optimal convergence rates can be established in a way similar to the pure Neumann BVP.*

Remark 3.2.2. *In all cases, the system of governing algebraic equations is constructed so that one has to invert matrices associated with the operators* $\frac{1}{2}\mathcal{I} + \mathcal{K}$ *and* $\frac{1}{2}\mathcal{I} - \mathcal{K}'$. *This construction results in well-conditioned linear algebraic systems [3], and it is superior to alternative formulations; see Section 3.5 for numerical examples.*

Remark 3.2.3. *Following [71] one can prove unique solvability and optimal convergence of the Collocation scheme using two ingredients, (i) compactness*

of both $\mathcal{K}$ and $\mathcal{K}'$, and (ii) boundedness of the interpolation operator $\mathcal{I}_h$. This leads to the bounds

$$\|u_h\|_{L^\infty} \leq C \left\| \mathcal{I}_h \left(\frac{1}{2}\mathcal{I} + \mathcal{K} \right) u_h \right\|_{L^\infty} ,$$

and

$$\|t_h\|_{L^\infty} \leq C \left\| \mathcal{I}_h \left(\frac{1}{2}\mathcal{I} - \mathcal{K}' \right) t_h \right\|_{L^\infty} ,$$

which in turn lead to unique solvability and optimal convergence of the Neumann and Dirichlet problems, respectively. For NURBS, the boundedness of $\mathcal{I}_h$ has been established under restrictive conditions [40, 41, 60] but not in general.

3.3 Regularization of operators

In general, the SBIE and HSBIE involve weakly-singular, singular and hyper-singular integrals. This is problematic because the numerical evaluation of singular or hyper-singular integrals is problematic. In this section, we establish that for sufficiently smooth geometries and functions, all boundary integral operators introduced in Section 3.1 can be evaluated as weakly-singular integrals. To this end, we first concentrate on $\Gamma \in C^2$ and then generalize the results to $\Gamma \in \tilde{C}^2$. Once it is established that all integral operators can be evaluated as weakly-singular integrals, appropriate numerical integration schemes are established in Section 3.4.

3.3.1 Integral operators on C^2-surfaces

The single-layer operator $\mathcal{V}$ is naturally weakly-singular for the continuous data; the same is true for $\mathcal{K}$ and $\mathcal{K}'$ (see Appendix). To regularize the hyper-singular operator $\mathcal{D}$ we begin with approximating $u \in C^2(\Gamma)$ in the vicinity of x:

$$u(y) = u(x) + (\nabla_T u)(x) \cdot (y - x) + \mathcal{O}(|x - y|^2) \,, \tag{3.16}$$

where $(\nabla_T u)(x)$ is the tangential gradient of u on Γ. With this approximation, the hyper-singular operator can be expressed as

$$\begin{aligned}
\mathcal{D}u(x) &= -\int_\Gamma n(x) \cdot \nabla_x \left\{ n(y) \cdot [\nabla_y G(x,y)] \right\} u(y) ds_y \\
&= -\int_\Gamma n(x) \cdot \nabla_x \left\{ n(y) \cdot [\nabla_y G(x,y)] \right\} \\
&\qquad\qquad [u(y) - u(x) - (\nabla_T u)(x) \cdot (y - x)] ds_y \\
&\quad - u(x) \int_\Gamma n(x) \cdot \nabla_x \left\{ n(y) \cdot [\nabla_y G(x,y)] \right\} ds_y \\
&\quad - \int_\Gamma n(x) \cdot \nabla_x \left\{ n(y) \cdot [\nabla_y G(x,y)] \right\} (\nabla_T u)(x) \cdot (y - x) ds_y \,.
\end{aligned} \tag{3.17}$$

Since constant and linear functions are harmonic, the HSBIE implies that

$$-\int_\Gamma n(x) \cdot \nabla_x \left\{ n(y) \cdot [\nabla_y G(x,y)] \right\} ds_y = 0$$

and

$$\begin{aligned}
&-\int_\Gamma n(x) \cdot \{ \nabla_x n(y) \cdot [\nabla_y G(x,y)] \} (\nabla_T u)(x) \cdot (y - x) ds_y = \\
&\qquad -\int_\Gamma n(x) \cdot \nabla_x \left[G(x,y) \right] n(y) \cdot (\nabla_T u)(x) ds_y .
\end{aligned}$$

Now the last line of (3.17) can be rewritten as

$$\begin{aligned}\mathcal{D}u(x) = \\ &- \int_\Gamma n(x)\cdot\nabla_x\left\{n(y)\cdot[\nabla_y G(x,y)]\right\}\left[u(y)-u(x)-(\nabla_T u)(x)\cdot(y-x)\right]ds_y \\ &- \int_\Gamma n(x)\cdot\nabla_x\left[G(x,y)\right]n(y)\cdot(\nabla_T u)(x)ds_y\,.\end{aligned} \tag{3.18}$$

In this equation, the first term on the right-hand side is weakly-singular because of (3.16) and the second term is weakly-singular because it is equal to $\mathcal{K}'[n(y)\cdot(\nabla_T u)(x)]$. Our development closely follows that in [61] where some theoretical aspects are laid but no scheme is suggested to compute the surface gradient $\nabla_T u$. In addition, no numerical examples can be found in the literature that use this regularization scheme for Collocation discretizations of BIEs defined on surfaces in $\mathbb{R}^3$. In this dissertation, we provide an explicit procedure to compute $\nabla_T u$ in Section 3.4, and provide several numerical examples involving smooth and non-smooth surfaces in $\mathbb{R}^3$ that confirm the reliability of this regularization technique in the context of IgA.

3.3.2 Integral operators on $\tilde{C}^2$-surfaces

In Section 3.3.1, we have established that the evaluation of all integral operators on C^2-surfaces can be reduced to the evaluation of weakly-singular integrals. In this section, we extend these results to $\tilde{C}^2$-surfaces. As established in Section 3.2 for $\tilde{C}^2$-surfaces, discontinuous basis functions should be used to approximate the Neumann data t and continuous basis functions should be used to approximate the Dirichlet data u. Accordingly, since we use the SBIE

to invert for u and the HSBIE to invert for t, the integral operators of the SBIE have to be evaluated at collocation points that possibly lie on non-smooth parts of Γ, whereas the integral operators of the HSBIE can be evaluated at points that only lie on smooth parts of Γ. In what follows we show that this allows one to extend the results of Section 3.3.1 to $\tilde{C}^2$-surfaces.

The single layer potential $\mathcal{V}$ naturally remains a weakly-singular operator on $\tilde{C}^2$-surfaces and therefore can be straight-forwardly evaluated as a weakly-singular integral. The double layer potential $\mathcal{K}$, however, is not a natural weakly-singular operator on $\tilde{C}^2$-surfaces. Nevertheless, one can use the fact that

$$(\sigma\mathcal{I} + \mathcal{K})\, 1 = 0$$

for the regularization

$$(\sigma\mathcal{I} + \mathcal{K})\, u(x) = \int_\Gamma n(y)\nabla_y G(x,y)\,[u(y) - u(x)]\, ds_y\,.$$

Consequently, if u is Lipschitz continuous,

$$|u(y) - u(x)| < C\,|y - x|\ ,$$

the operator $\mathcal{K}$ can be evaluted as a weakly-singular integral. Not every continuous function u is Lipschitz continuous but the T-spline basis functions used to approximate u are naturally Lipschitz continuous. Consequently, all integral operators of the SBIE can be reduced to the evaluation of weakly-singular integrals.

To establish the result for the HSBIE, we first observe that because discontinuous basis functions are used for t, the HSBIE only has to be evaluated at points that lie on smooth parts of Γ. Consequently, the representation (3.18) of $\mathcal{D}$ is still valid on $\tilde{C}^2$-surfaces and we get

$$\begin{aligned}
\mathcal{K}'t(x) &= \int_\Gamma n(x)\cdot\nabla_x G(x,y)t(y)ds_y,\\
\mathcal{D}u(x) &= \\
&-\int_\Gamma n(x)\cdot\nabla_x\left\{n(y)\cdot\left[\nabla_y G(x,y)\right]\right\}\left[u(y)-u(x)-(\nabla_T u)(x)\cdot(y-x)\right]ds_y\\
&-\int_\Gamma n(x)\cdot\nabla_x\left[G(x,y)\right]n(y)\cdot(\nabla_T u)(x)ds_y\,.
\end{aligned}$$

Since $\Gamma\in\tilde{C}^2$ and x lies on a smooth part of Γ, there exists a smooth neighborhood $U_x\subset\Gamma$ of x. Accordingly, all integrals can be divided into two: an integral over U_x, and an integral over $\Gamma\backslash U_x$. Let us first observe that since $x\in U_x$, all integrals over $\Gamma\backslash U_x$ are naturally regular integrals and we only have to focus on the integrals over U_x. It is easy to see that using local rather than global Taylor expansions $\mathcal{K}'$ can still be proved to be weakly-singular on U_x. Similarly, the techniques described in Section 3.3.1 can be used on U_x rather than Γ in order to show that the integrals over U_x required to evaluate $\mathcal{D}$ also reduce to weakly-singular ones. As a result, on C^2 as well as $\tilde{C}^2$-surfaces, all boundary integral operators considered in this dissertation can be reduced to the evaluation of weakly-singular integrals only.

3.4 Numerical Integration

It has been established in Section 3.3 that, upon collocation, all operators can be evaluated as weakly-singular integrals on C^2- and $\tilde{C}^2$-surfaces. In this section, we focus on numerical integration schemes to evaluate these weakly-singular integrals. Let us observe that even for $\tilde{C}^2$-surfaces the T-spline surface parametrization and basis functions are both C^∞ on each Bézier element and the neighborhood U_x introduced in Section 3.3.2 can be defined as a union of Bézier elements. This allows one to evaluate all boundary integral operators as integrals over Bézier elements that are either weakly-singular (if the evaluation point touches the Bézier element) or regular (if the evaluation point does not touch the Bézier element). Accordingly, in what follows we introduce integration schemes for the evaluation of these weakly-singular and regular integrals over one Bézier element.

3.4.1 Evaluation of weakly-singular integrals

Since all basis functions are C^∞ on every Bézier element $\varphi(e) \subset \Gamma$, we need to develop numerical integration techniques for integrals of the form

$$I_x := \int_{\varphi(e)} \frac{1}{|x-y|} f(y) ds_y \tag{3.19}$$

where $x \in \overline{\varphi(e)}$ and f is a C^∞ function on $\varphi(e)$. As usual, we evaluate these integrals in the parametric domain e rather than $\varphi(e)$. To this end, we can rewrite

$$I_x = \int_e \frac{1}{|\varphi(\eta_1,\eta_2) - \varphi(\xi_1,\xi_2)|} f(\varphi(\xi_1,\xi_2)) J(\xi_1,\xi_2) d\xi_1 d\xi_2$$

where $(\eta_1, \eta_2) \in \overline{e}$ such that $\varphi(\eta_1, \eta_2) = x$ and

$$J(\xi_1, \xi_2) = \left| \frac{\partial \varphi(\xi_1, \xi_2)}{\partial \xi_1} \times \frac{\partial \varphi(\xi_1, \xi_2)}{\partial \xi_2} \right|.$$

For conventional BEMs, many reliable and spectrally accurate integration schemes have been developed for these types of integrals and are still a topic of ongoing research [21, 63, 92]. In this dissertation, we adapt the technique of using polar coordinate transformations for the evaluation of weakly-singular integrals; details of this technique can be found in Appendix B. In many cases, this integration scheme is appropriate for the evaluation of the weakly-singular integrals. However, in the context of IgA, if the geometry parametrization involves collapsed edges, a straight forward application of this integration scheme is not adequate; see Section 3.5.3. This is because the first derivative of the surface parametrization vanishes at collapsed edges, a situation that does not appear in conventional BEMs. In what follows, we show how the existing polar coordinate transformation can be adapted to efficiently treat geometry parametrizations that may or may not involve collapsed edges.

Let us recall that it was established in [91] that the integral kernel can be rewritten as

$$\frac{1}{|\varphi(\eta_1, \eta_2) - \varphi(\xi_1, \xi_2)|} = \frac{1}{\rho} \sum_{n=0}^{\infty} \rho^n \frac{p_{3n}(\theta)}{[l_2(\theta)]^{n+\frac{1}{2}}}$$

as long as φ is analytic in e. Here, (ρ, θ) are the polar coordinates in e centered at (η_1, η_2), p_{3n} is a homogeneous polynomial of order $3n$ in $\cos\theta$ and $\sin\theta$ whose coefficients only depend on derivatives of φ at (η_1, η_2), and

$$l_2(\theta) = c\left(\lambda\cos^2\theta + 2\cos\gamma\cos\theta\sin\theta + \frac{1}{\lambda}\sin^2\theta\right),$$

where

$$c = \left|\frac{\partial\varphi(\eta_1,\eta_2)}{\partial\eta_1}\right|\left|\frac{\partial\varphi(\eta_1,\eta_2)}{\partial\eta_2}\right|, \quad \lambda = \frac{\left|\frac{\partial\varphi(\eta_1,\eta_2)}{\partial\eta_1}\right|}{\left|\frac{\partial\varphi(\eta_1,\eta_2)}{\partial\eta_2}\right|}, \quad \cos\gamma = \frac{\frac{\partial\varphi(\eta_1,\eta_2)}{\partial\eta_1}\cdot\frac{\partial\varphi(\eta_1,\eta_2)}{\partial\eta_2}}{\left|\frac{\partial\varphi(\eta_1,\eta_2)}{\partial\eta_1}\right|\left|\frac{\partial\varphi(\eta_1,\eta_2)}{\partial\eta_2}\right|}.$$

This shows that as long as l_2 is bounded below, the transformation of the integral I_x into polar coordinates results in an analytic integrand in (ρ, θ) because the Jacobian of the polar coordinate transformation cancels with the term $1/\rho$. While this is true for all geometry parametrizations used in conventional BEMs, if the IgA geometry parametrization involves collapsed edges, l_2 is not necessarily bounded below. In this case, the integrand is not analytic in ρ and θ and therefore Gaussian quadratures cannot be applied efficiently. To address this issue we consider the two cases of the collocation point x_A being on and away from a collapsed edge.

If the collocation point is away from a collapsed edge, we can observe that if the vectors $\frac{\partial\varphi(\eta_1,\eta_2)}{\partial\eta_1}$ and $\frac{\partial\varphi(\eta_1,\eta_2)}{\partial\eta_2}$ are orthonormal, then $l_2(\theta) = 1$. Therefore, the issue of l_2 not being bounded below can be effectively treated by orthonormalizing the vectors $\frac{\partial\varphi(\eta_1,\eta_2)}{\partial\eta_1}$ and $\frac{\partial\varphi(\eta_1,\eta_2)}{\partial\eta_2}$. We do this in the same fashion as in [21]:

1. At a given collocation point, compute the vectors τ^1 and τ^2 as

$$\tau^1 = \frac{\partial \varphi(\eta_1, \eta_2)}{\partial \eta_1} \quad \text{and} \quad \tau^2 = \frac{\partial \varphi(\eta_1, \eta_2)}{\partial \eta_2} \, .$$

2. Form a Jacobian matrix

$$\begin{pmatrix} \tau_1^1 & \tau_1^2 \\ \tau_2^1 & \tau_2^2 \\ \tau_3^1 & \tau_3^2 \end{pmatrix} \, ,$$

   where the subscripts refer to the Cartesian components in a global coordinate system, in which the control points are prescribed.

3. Compute the reduced singular-value decomposition

$$\begin{pmatrix} \tau_1^1 & \tau_1^2 \\ \tau_2^1 & \tau_2^2 \\ \tau_3^1 & \tau_3^2 \end{pmatrix} = U \Sigma V^* \, ,$$

   so that U is a 3×2 matrix and Σ is a 2×2 diagonal matrix with no zeros on the diagonal.

4. Define the reparametrization $\bar{\varphi}(\bar{\xi}_1, \bar{\xi}_2)$ of $\varphi(\xi_1, \xi_2)$ via

$$\varphi(\xi_1, \xi_2) = \bar{\varphi}(\bar{\xi}_1, \bar{\xi}_2) = \varphi(V \Sigma^{-1} \bar{\xi}) \, ,$$

   where $\bar{\xi} = (\bar{\xi}_1, \bar{\xi}_2)^T$.

5. Evaluate the integral I_x by using polar coordinate transformations on the parallelogram $\Sigma V^T e$; for details see Appendix B.

Note that this procedure can be applied to every collocation point that does not lie on a collapsed edge. In this case, independently of the surface parametrization, it can be assured that the integrand is analytic. This has already been

realized in [91] but is not commonly used in conventional BEMs where l_2 is bounded below and the orthonormalization scheme only provides a small improvement over standard polar coordinate transformation schemes. In contrast, in IBEMs, this orthonormalization scheme is crucial for the accurate evaluation of integral operators defined on surface parametrizations that involve collapsed edges; see Section 3.5.3.

If the collocation point is on a collapsed edge, then either $\frac{\partial\varphi(\eta_1,\eta_2)}{\partial\eta_1} = 0$ or $\frac{\partial\varphi(\eta_1,\eta_2)}{\partial\eta_2} = 0$. Here, we address the case $\frac{\partial\varphi(\eta_1,\eta_2)}{\partial\eta_1} = 0$ but the other case can be treated in the same way. If $\frac{\partial\varphi(\eta_1,\eta_2)}{\partial\eta_1} = 0$, it is easy to see that

$$l_2(\theta) = \left|\frac{\partial\varphi(\eta_1,\eta_2)}{\partial\eta_2}\right|^2 \sin^2\theta$$

and following [91] it can also be seen that

$$p_{3n}(\theta) = \sin^{3n}\theta\bar{p}_{3n}(\theta)$$

where $\bar{p}_{3n}$ is a homogeneous polynomial of order $3n$ in $\cos\theta$ and $\sin\theta$ whose coefficients only depend on derivatives of φ at (η_1,η_2). In addition, it holds

$$J(\xi_1,\xi_2) = |\xi_2-\eta_2|\bar{J}(\xi_1-\eta_1,\xi_2-\eta_2)$$

where $\bar{J}(\xi_1,\xi_2)$ is an analytic function whose coefficients only depend on derivatives of φ at (η_1,η_2). As a result, we get that

$$\frac{J(\xi_1,\xi_2)}{|\varphi(\eta_1,\eta_2)-\varphi(\xi_1,\xi_2)|} = \sum_{n=0}^{\infty}\rho^n\sin^n(\theta)\bar{p}_{3n}(\theta)\bar{J}(\rho\cos\theta,\rho\sin\theta).$$

is an analytic function in ρ and θ. This shows that in the case of the collocation point being located at a collapsed edge, without orthonormalizaiton, the use of polar coordinate transformations results in analytic integrands and therefore Gaussian quadratures can be applied efficiently for the variables ρ and θ; for details see Appendix B.

3.4.2 Evaluation of regular integrals

Again, since all basis functions are C^∞ on every Bézier element $\varphi(e)$, we need to develop numerical integration techniques for integrals of the form

$$I_x := \int_{\varphi(e)} \frac{1}{|x-y|} f(y) ds_y \tag{3.20}$$

where $x \notin \overline{\varphi(e)}$ and f is a C^∞ function on $\varphi(e)$. In the same way as weakly-singular integrals, we evaluate the regular integrals in the parametric domain e rather than $\varphi(e)$. To this end, we can rewrite

$$I_x = \int_e \frac{1}{|x-\varphi(\xi_1,\xi_2)|} f(\varphi(\xi_1,\xi_2) J(\xi_1,\xi_2) d\xi_1 d\xi_2 \, .$$

Note that these integrals are regular and therefore Gaussian quadratures can be used. Adapting the proof of Theorem 5.3.24 in [88], it is easy to see that using n Gaussian integration points in each direction, the error E of this numerical integration scheme can be estimated by

$$E \leq C h^2 d^{-3} \left(\frac{d}{h}\right)^p \left(\max\left(\frac{d}{h}, 1\right)\right)^{-2n} \tag{3.21}$$

where h is the ratio of the square root of the area of $\varphi(e)$ and $\sqrt{|\Gamma|}$, d is the ratio of the distance of $\varphi(e)$ to x_A in physical space and $\sqrt{|\Gamma|}$, $|\Gamma|$ is the surface area of Γ, p is the polynomial degree of the basis function, and $C > 0$ is a constant independent of h, p and d.

Note that this shows that the error of Gaussian quadratures directly applied to the regular integral significantly increases if x_A is close to $\varphi(e)$. To this end, it is standard to employ a subdivision scheme to reduce the distance of x_A with respect to the size of the integration domain. Here, we first compute d and h. If $d < 3h$, we recursively refine the element $\varphi(e)$ until $d \geq 3h$ for every subelement and then apply Gaussian quadratures to each subelement. If $d \geq 3h$, Gaussian quadratures are applied directly to the whole element. Figure 3.1 illustrates this adaptive refinement strategy. Then the estimate (3.21) can be used to estimate the number of Gaussian integration points needed in each subelement to achieve the error E. Note that ignoring the constant C, the number of Gaussian integration points needed in order to achieve an error E on each subelement can be estimated by

$$n \geq \frac{1}{2}\left(p - 3 - \frac{\log(Eh)}{\log 3}\right) .$$

Here we used that the subdivision scheme is such that $d \geq 3h$ on each subelement. Further, if the subdivision scheme is not employed, it holds $d \geq 3h$ for the element $\varphi(e)$ and Gaussian quadratures can be used directly on the element e. In this case, the number of Gauss points to achieve an error E on

the element can be estimated by

$$n \geq \frac{1}{2}\left(p - 3 - \frac{\log(Eh)}{\log \frac{d}{h}}\right).$$

Note that T-splines of degree p result in the element-wise approximation error of $\mathcal{O}\left(h^{p+1}\right)$. To preserve this error estimate globally one should choose $E = \mathcal{O}\left(h^{p+3}\right)$. The exponent $p+3$ rather than $p+1$ takes into account that the global error is induced by $\mathcal{O}\left(h^{-2}\right)$ element-wise approximation errors.

For curvilinear elements, the distance d between $\varphi(e)$ and x is computed as follows:

1. Construct the L^2-projection of $\varphi(e)$ on $(p+1)^2$ local Bernstein polynomials.
2. The vector-valued coefficients of the projection are the control points of the approximating surface.
3. Use Ritter's algorithm [80] to compute a bounding ball of those control points.
4. Compute the distance d as the distance between x and the ball.

3.4.3 Integration over elements with high curvature or high aspect ratio

The outlined integration scheme, which we regard as the basic one, works well for relatively simple geometries and fine meshes. However, if the

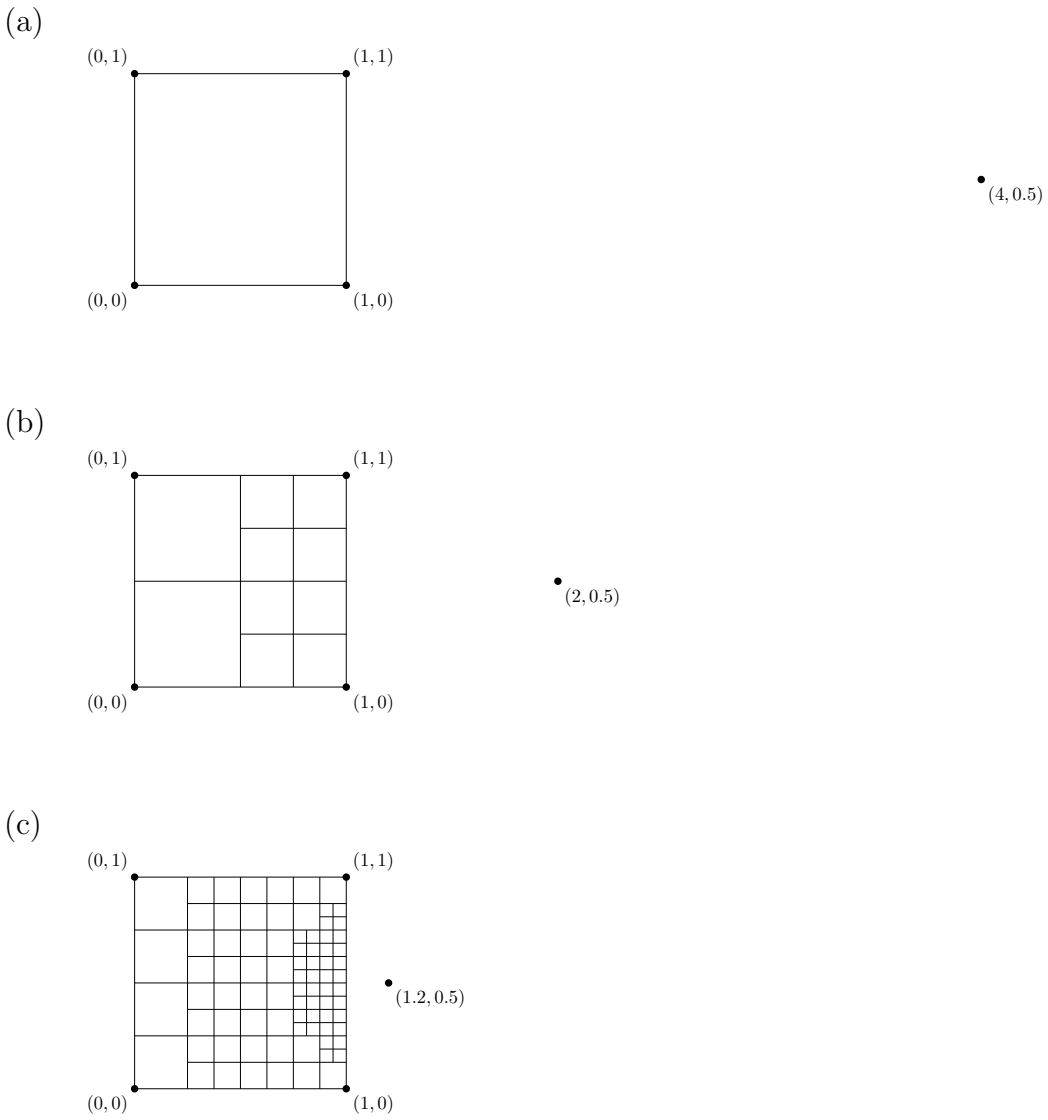

Figure 3.1: Examples for the adaptive refinement technique for different locations of the collocation point with respect to the Bézier element.

geometric parametrization involves Bézier elements with large aspect ratios in the physical space or if the derivatives of φ are very high for an element e (e.g. if the element is highly curved), the outlined integration scheme may be insufficient. To address this issue, we introduce additional subdivision schemes, which reduce the aspect ratios and curvatures via local refinement.

The aspect ratio of an element e is reduced according to the following scheme:

1. Chose a threshold constant $C_a > 1$.

2. Compute the length of each edge of e in the physical space.

3. If the element does not involve a collapsed edge, compute the aspect ratio as
$$\rho_a = \frac{l_1 + l_3}{l_2 + l_4}.$$
In this equation, the subscript 1 refers to the longest edge, the subscript 3 refers to the edge opposite to the longest one, and the subscripts 2 and 4 refer to the other two edges. If $\rho_a > C_a$, split e into two elements by connecting the mid-points of the edges 1 and 3; otherwise accept the element.

4. If the element involves a collapsed edge, we do not address the issue of high aspect ratios and automatically accept elements that involve collapsed edges.

The curvature of an element e is reduced according to the following scheme:

1. Chose a threshold constant $C_c > 1$.

2. Compute the area A of e in the physical space.

3. If the element does not involve a collapsed edge, compute the total area A_0 of two *planar* triangles, one formed by the vertices of the edges 1 and 2, and the other by the vertices of the edges 3 and 4. Compute the normalized curvature
$$\rho_c = \frac{A}{A_0}.$$

4. If the element involves a collapsed edge, the area A_0 is computed using the element vertices.

5. If $\rho_c > C_c$, divide e into four elements using the standard procedure; otherwise accept the element.

The two schemes are applied using a two-stage cycle. At the first stage, if necessary, one reduces the aspect ratio. At the second stage, if necessary, one reduces the curvature of the elements generated during the first stage. Then the cycle is repeated as necessary. Once all elements attain sufficiently small aspect ratios and curvatures, one proceeds with the basic integration scheme. In Section 5, we use the framework of BEM Patch Tests to provide numerical examples that show the need and the effect of this additional subdivision technique.

3.5 Numerical Examples

3.5.1 Overview

In this section, we present numerical examples emphasizing various important mathematical and computational aspects of IgA of BIEs. All examples involve three shapes: a torus, a sphere, and a cube. The torus is a C^∞-surface which allows a C^2-parametrization; actually one can show that the torus parametrization is C^∞ but this additional smoothness is not exploited. The sphere is a C^∞-surface with a $\tilde{C}^2$-parametrization, because it involves collapsed edges at the poles. The cube is a $\tilde{C}^2$-surface with a $\tilde{C}^2$-parametrization. All shapes were constructed using standard parametrizations based on 16 (torus), 8 (sphere), and 6 (cube) NURBS patches. For each shape, the patches were used to generate five meshes via uniform refinement in the parametric domain, so that at each level of refinement, each element was divided into four. Figure 3.3 shows the two coarsest meshes for each shape. Continuous basis functions of degree p were constructed so that, upon refinement, they remained C^{p-1} locally and continuous over patch boundaries. In contrast to continuous basis functions, their discontinuous counterparts were C^{p-1} locally and discontinuous over patch boundaries. Unless otherwise noted, all regular approximations involved $p = 2$, and degree elevated approximations involved $p = 3$. All numerical examples presented in this section involve the basic numerical integration scheme only, the subdivision scheme aimed at reducing aspects ratios and curvatures is not necessary. This procedure will be utilized in Chapter 5.

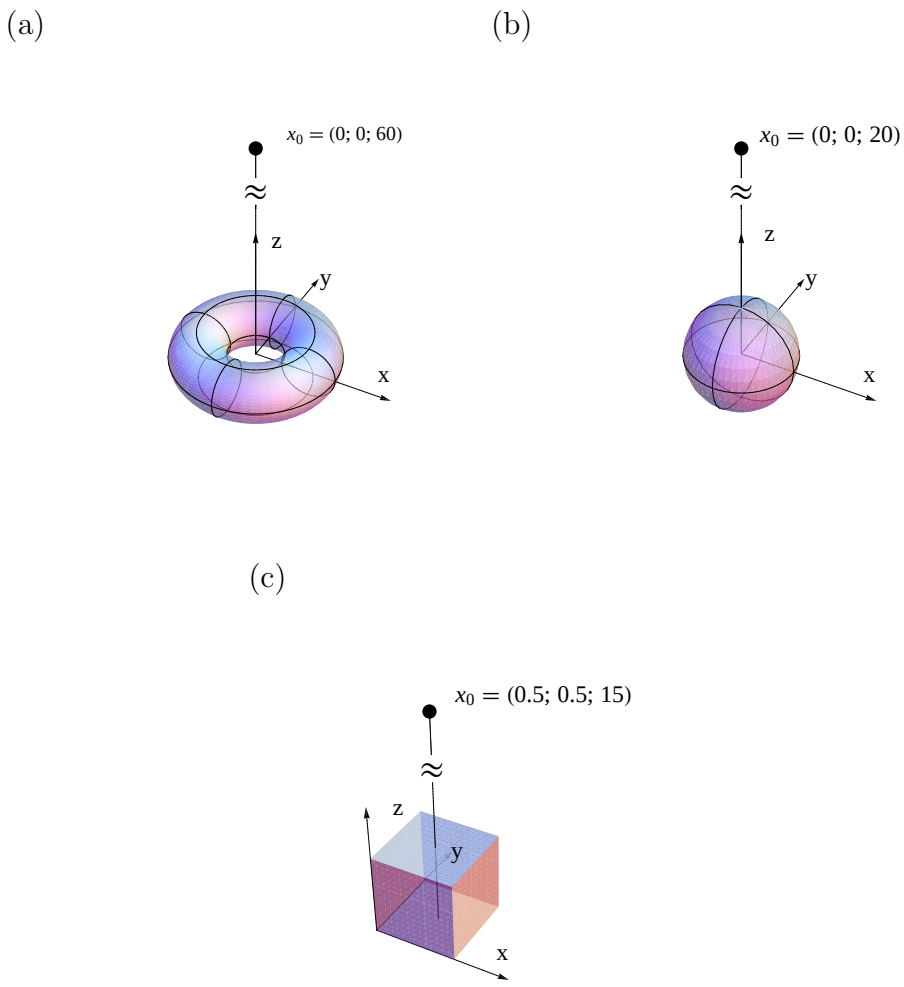

Figure 3.2: Three representative shapes: (a) torus (inner radius $r = 1$ and outer radius $R = 3$), (b) sphere (radius $r = 1$), and (c) cube (edge length $a = 1$). The source points for the manufactured solutions: $x_0 = (0, 0, 60)$ for the torus, $x_0 = (0, 0, 20)$ for the sphere, and $x_0 = (1/2, 1/2, 15)$ for the cube.

(a)

(b)

(c)

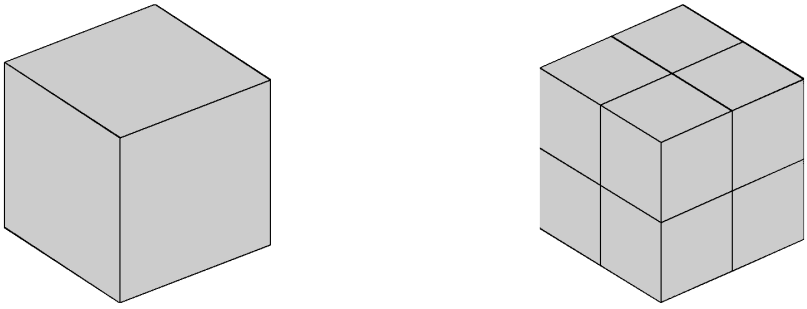

Figure 3.3: Meshes for the first two refinement levels for the (a) torus, (b) sphere, and (c) cube.

The majority of numerical examples involved manufactured exact solutions in the form

$$u(x) = \frac{1}{|x - x_0|} \,. \tag{3.22}$$

For each shape the source point x_0 was chosen far away from the shape center (Fig. 3.2), so that $u(x)$ was an analytic function which did not involve near-singular behavior. These manufactured solutions were chosen in order to demonstrate the necessity of numerical schemes even for problems with smooth solutions. The function $u(x)$ was used to construct the boundary data g_D and/or g_N for various BVPs. After that, appropriate BIEs were solved numerically to reconstruct the full Cauchy data.

The quality of numerical solutions was measured using the $L^2(\Gamma)$-error for the Cauchy data. To evaluate the order of convergence, we defined the mesh size h as the square root of the area of the largest Bézier element in the physical space. The estimated order of convergence (eoc) for each refinement was computed as

$$eoc = \frac{\log\left(\frac{e_f}{e_c}\right)}{\log\left(\frac{h_f}{h_c}\right)} \,,$$

where the subscripts f and c refer to the fine and coarse meshes, respectively. For $p = 2$ the optimal order of convergence for the $L^2(\Gamma)$-error for the Cauchy data is equal to $p + 1 = 3$. In addition, we also provide the number of kernel evaluations N_{Keval} required for each solution. This provides a comparison

of the computational efficiency of our method compared to other methods. However, as the main focus of this dissertation is reliability and not efficiency, no further comparisons are made in view of efficiency.

Unless stated otherwise, all arising algebraic problems were solved using a preconditioned GMRES method [85] with a tolerance of 10^{-12}. Each preconditioner was constructed as the inverse of the interpolation matrix corresponding to the basis functions. As a result, we were able to reveal the spectral properties of the collocated operators and significantly reduce the iteration count.

In the remainder of this section, we present six case studies. Each study demonstrates the importance of a particular aspect. Those studies focus on (i) the recursive subdivision scheme for near-singular integration (Section 3.5.2), (ii) local surface reparametrization (Section 3.5.3), (iii) exponential convergence of the adopted integration scheme (Section 3.5.4), (iv) spectral properties of the collocated operators (Section 3.5.5), (v) discontinuous basis functions (Section 3.5.6), and (vi) approximations for mixed BVPs (Section 3.5.7).

3.5.2 Recursive subdivision for near-singular integration

The objective of this section is to demonstrate that the recursive subdivision scheme (Section 3.4) for evaluating near-singular integrals is essential. To this end, we considered the manufactured pure Neumann BVP on the torus and established that the optimal order of convergence and accurate results can

be attained only if the subdivision scheme was employed. The approximate solutions to this problem were obtained by solving (3.13) and (3.14), using continuous basis functions.

Figure 3.4 and Table 3.1 present the $L^2(\Gamma)$-error of $\tilde{u}_h$ for two numerical integration schemes, with and without recursive subdivision. It is clear that recursive subdivision is necessary for attaining the optimal order of convergence. Furthermore, recursive subdivision significantly reduced the magnitude of the errors. The numerical example is representative of the other shapes and boundary conditions.

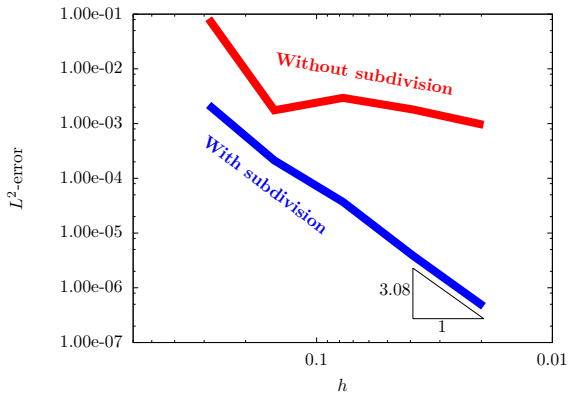

Figure 3.4: $L^2(\Gamma)$-errors for two near-singular integration schemes: with and without subdivision.

3.5.3 Surface reparametrization scheme

The objective of this section is to demonstrate the importance of the surface reparametrization scheme (Section 3.3) for evaluating singular inte-

	With subdivision			Without subdivision		
h	N_{Keval}	L^2-error	eoc	N_{Keval}	L^2-error	eoc
2.87E-01	4.97E+05	2.19E-03		2.97E+04	8.24E-02	
1.51E-01	4.18E+06	2.12E-04	3.62	1.98E+05	1.75E-03	5.97
7.73E-02	2.68E+07	3.70E-05	2.62	1.95E+06	2.95E-03	-0.78
3.90E-02	1.62E+08	3.87E-06	3.31	2.43E+07	1.81E-03	0.72
1.96E-02	1.28E+09	4.60E-07	3.08	3.43E+08	9.49E-04	0.93

Table 3.1: $L^2(\Gamma)$-errors for two near-singular integration schemes: with and without subdivision.

grals, particularly when collapsed edges are involved. To this end, we considered the manufactured pure Dirichlet BVP on the sphere. The approximate solutions to this problem were first obtained by using the SBIE and discontinuous basis functions. The corresponding linear algebraic problem is

$$V\underline{\tilde{t}} = \underline{f}_S \,. \tag{3.23}$$

Note that the SBIE requires one to invert the matrix corresponding to the single-layer operator, which is not optimal, as far as the spectral properties are concerned. Nevertheless, it allows us to demonstrate that the surface reparametrization scheme is necessary even for a naturally weakly-singular operator.

Figure 3.5 and Table 3.2 present the $L^2(\Gamma)$-error for the solutions of (3.23), using two numerical integration schemes, with and without the reparametrization. It is clear that the reparametrization is necessary for attaining the optimal order of convergence and small errors. This example is representative of

other CAD parametrizations involving collapsed edges.

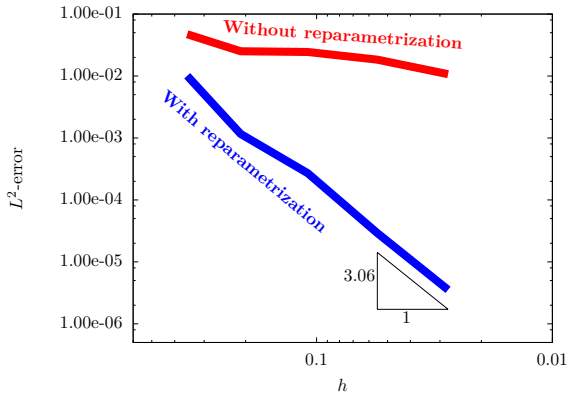

Figure 3.5: The manufactured pure Dirichlet BVP for the sphere: $L^2(\Gamma)$-errors for two singular integration schemes, with and without reparametrization.

	With reparametrization			Without reparametrization		
h	N_{Keval}	L^2-error	eoc	N_{Keval}	L^2-error	eoc
3.54E-01	3.53E+05	1.01E-02		3.53E+05	4.72E-02	
2.10E-01	2.36E+06	1.16E-03	4.17	2.36E+06	2.51E-02	1.21
1.09E-01	1.67E+07	2.70E-04	2.23	1.67E+07	2.44E-02	0.05
5.53E-02	1.00E+08	2.92E-05	3.26	1.00E+08	1.84E-02	0.41
2.77E-02	6.52E+08	3.54E-06	3.06	6.52E+08	1.07E-02	0.79

Table 3.2: The manufactured pure Dirichlet BVP for the sphere: $L^2(\Gamma)$-errors for two singular integration schemes, with and without reparametrization.

Alternatively, one can solve the manufactured problem using the HSBIE (3.15) and the discontinuous basis functions. In this case, similar to equation (3.23), the reparametrization scheme is necessary for accurate integration at collocation points near collapsed edges. Further the reparametrization scheme is

natural for computing the tangent gradient required for regularizing the hyper-singular operator. Figure 3.6 and Table 3.3 present the $L^2(\Gamma)$-error of $\tilde{t}_h$ on the sphere using SBIE and HSBIE; results for the SBIE are identical to those presented in Figure 3.5. It is clear that the two approaches yield similar results, and therefore both are acceptable. Thus we can conclude that the surface reparametrization scheme is necessary, and it is capable of delivering optimal and accurate numerical solutions even if the hyper-singular operator is involved.

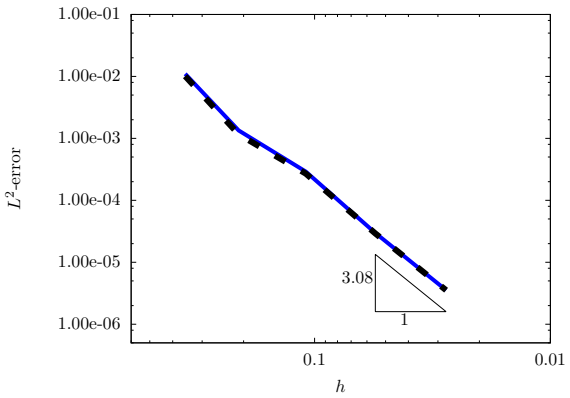

Figure 3.6: The manufactured pure Dirichlet BVP for the sphere: $L^2(\Gamma)$-errors for two approaches, one based on the SBIE (dashed line) and the other based on the HSBIE (solid line).

3.5.4 Exponential convergence of the integration scheme

The objective of this section is to demonstrate that the adopted numerical integration scheme is exponentially convergent with respect to the number of integration points. The demonstration involves all three shapes. Thus the

	SBIE			HSBIE		
h	N_{Keval}	L^2-error	eoc	N_{Keval}	L^2-error	eoc
3.54E-01	3.53E+05	1.01E-02		3.53E+05	1.10E-02	
2.10E-01	2.36E+06	1.16E-03	4.17	2.36E+06	1.34E-03	4.05
1.09E-01	1.67E+07	2.70E-04	2.23	1.67E+07	2.91E-04	2.34
5.53E-02	1.00E+08	2.92E-05	3.26	1.00E+08	2.98E-05	3.34
2.77E-02	6.52E+08	3.54E-06	3.06	6.52E+08	3.55E-06	3.08

Table 3.3: The manufactured pure Dirichlet BVP for the sphere: $L^2(\Gamma)$-errors for two approaches, one based on the SBIE (dashed line) and the other based on the HSBIE (solid line).

integration scheme was tested on problems involving non-smooth surfaces and parametrizations. For each shape, the test problem was a pure Neumann BVP with the exact solution

$$u(x) = x_1 + x_2 + x_3, \quad x \in \Omega\,.$$

For this choice, one can prove that the approximation error is exactly equal to zero for every shape, and therefore the chosen test problems are ideal for assessing numerical integration errors.

Figure 3.7 and Table 3.4 present the $L^2(\Gamma)$-error of the solution u_h. The results were obtained by using the coarsest meshes, while the number of integration points in each direction was increased. The results confirm an exponential convergence for every shape. Note that we were able to reach the machine precision for the sphere and the cube, while for the torus the error stagnated near 10^{-10} due to round-off errors in the adopted numerical integration scheme.

If desired, this issue can be resolved by using a more sophisticated singular integration scheme proposed in [21].

3.5.5 Spectral properties of integral operators

It is well-known that, upon discretization, the operators $\frac{1}{2}\mathcal{I} + \mathcal{K}$ and $\frac{1}{2}\mathcal{I} - \mathcal{K}'$ give rise to well-conditioned matrices. The objective of this section is to demonstrate that one should choose the governing BIEs so that one takes advantage of this property. Accordingly, for pure Neumann BVPs, the SBIE is a natural choice. In contrast, for pure Dirichlet BVPs, one should choose the HSBIE. This choice would be problematic for conventional collocation BEMs but it is legitimate for IgA. This point will be supported by numerical examples presented in Section 3.5.5.1. Further, we show that for mixed boundary-value problems one should choose the SBIE on Γ_N and the HSBIE on Γ_D. Numerical examples presented in Section 3.5.5.2 show that, as far as spectral properties and iteration counts are concerned, this choice is superior than uniform use of SBIE. Numerical examples involved the manufactured solutions for all three shapes and results are presented for both iteration counts and condition numbers.

3.5.5.1 Dirichlet problems

In principle, a pure Dirichlet BVP can be solved using either the SBIE or HSBIE. The corresponding linear algebraic problems are

$$V\underline{\tilde{t}} = \underline{f}_S$$

(a)

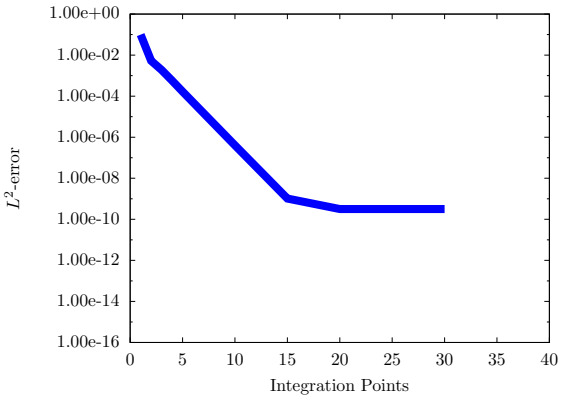

(b)

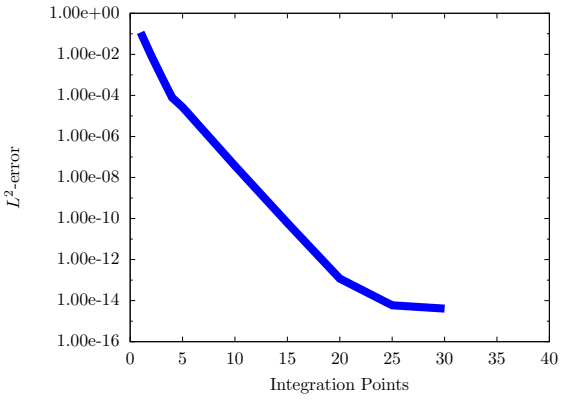

(c)

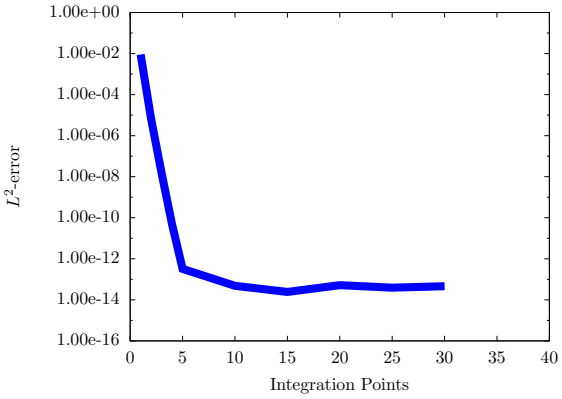

Figure 3.7: Numerical integration $L^2(\Gamma)$-errors for the (a) torus (b) sphere, and (c) cube.

(a)

Int. Pts.	N_{Keval}	L^2-error
1	4.16E+04	9.97E-02
2	1.66E+05	5.28E-03
3	3.74E+05	1.89E-03
4	6.65E+05	5.70E-04
5	1.04E+06	1.67E-04
10	4.16E+06	4.05E-07
15	9.35E+06	1.03E-09
20	1.66E+07	3.16E-10
25	2.60E+07	3.16E-10
30	3.74E+07	3.16E-10

(b)

Int. Pts.	N_{Keval}	L^2-error
1	2.58E+04	1.17E-01
2	1.03E+05	8.87E-03
3	2.32E+05	8.07E-04
4	4.12E+05	7.80E-05
5	6.44E+05	2.66E-05
10	2.58E+06	3.69E-08
15	5.80E+06	6.12E-11
20	1.03E+07	1.18E-13
25	1.61E+07	5.93E-15
30	2.32E+07	4.10E-15

(c)

Int. Pts.	N_{Keval}	L^2-error
1	1.98E+04	9.01E-03
2	7.91E+04	6.45E-06
3	1.78E+05	1.48E-08
4	3.16E+05	4.71E-11
5	4.94E+05	3.23E-13
10	1.98E+06	4.84E-14
15	4.45E+06	2.42E-14
20	7.91E+06	5.19E-14
25	1.24E+07	3.92E-14
30	1.78E+07	4.61E-14

Table 3.4: Numerical integration $L^2(\Gamma)$-errors for the (a) torus (b) sphere, and (c) cube.

and

$$\left(\frac{1}{2}I_N - K'\right)\underline{\tilde{t}} = \underline{f}_H \,.$$

Thus the SBIE-based approach requires one to invert V, whereas the HSBIE-based approach requires one to invert $\frac{1}{2}I_N - K'$.

Figure 3.8 and Table 3.5 present the iteration counts and spectral condition numbers κ as functions of h for the three shapes.

It is clear that the HSBIE is a better choice than the SBIE both in terms of the iteration counts and spectral properties. For the torus and sphere, the iteration counts and spectral properties for the HSBIE are independent of the mesh size. This is in agreement with theoretical results based on compactness of $\mathcal{K}'$. In this regard, let us observe that upon discretization the torus remains a C^2-surface, whereas the sphere becomes a $\tilde{C}^2$-surface. Thus the numerical results for the torus are fully expected, while the results for the sphere need additional theoretical considerations. For the cube, both the iteration count and the spectral condition number show a logarithmic dependence on h. For the cube, the mathematical foundations are not well-established because $\mathcal{K}'$ is not compact. For the SBIE, the iteration count should grow as $1/\sqrt{h}$ whereas κ should grow as $1/h$. Surprisingly, these scalings hold only for the cube. It is unclear to us why the results for the torus are better than expected and for the sphere worse than expected.

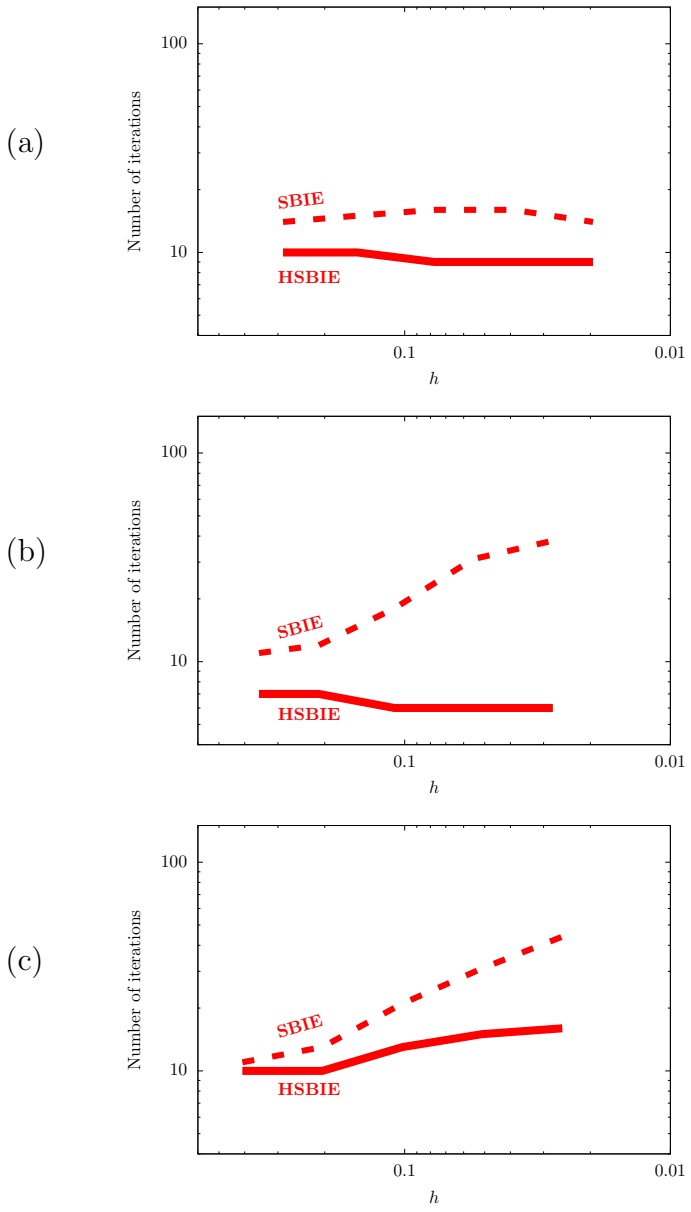

Figure 3.8: Iteration counts of the preconditioned GMRES method and condition numbers κ for the (a) torus (b) sphere, and (c) cube .

(a)

h	SBIE Number of iterations	SBIE κ	HSBIE Number of iterations	HSBIE κ
2.87E-01	14	33.44	10	3.21
1.51E-01	15	68.86	10	3.27
7.73E-02	16	145.92	9	3.29
3.90E-02	16	276.92	9	3.12
1.96E-02	14	523.13	9	2.98

(b)

h	SBIE Number of iterations	SBIE κ	HSBIE Number of iterations	HSBIE κ
3.54E-01	11	45.52	7	2.03
2.10E-01	12	154.40	7	2.23
1.09E-01	18	637.32	6	2.37
5.53E-02	31	2447.40	6	2.27
2.77E-02	38	9327.80	6	2.18

(c)

h	SBIE Number of iterations	SBIE κ	HSBIE Number of iterations	HSBIE κ
4.08E-01	11	16.25	10	3.17
2.04E-01	13	25.49	10	3.39
1.02E-01	21	50.36	13	4.02
5.10E-02	31	97.01	15	4.36
2.55E-02	44	187.97	16	4.61

Table 3.5: Iteration counts of the preconditioned GMRES method and condition numbers κ for the (a) torus (b) sphere, and (c) cube .

3.5.5.2 Mixed boundary-value problem

In this section, we present numerical examples suggesting that one should choose the SBIE on Γ_N and the HSBIE on Γ_D, as opposed to using the SBIE on the entire Γ. For our purposes, we choose boundary conditions as shown in Figure 3.9. For the torus and sphere, the Dirichlet (Neumann) boundary conditions are prescribed on the upper (lower) halves. For the cube, the Neumann boundary conditions are prescribed on the top and bottom faces, and the Dirichlet boundary conditions on the other faces. Similar to pure

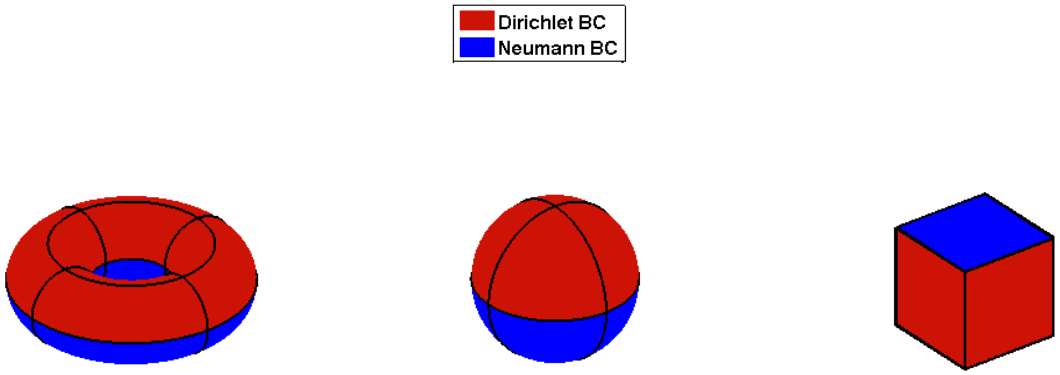

Figure 3.9: Mixed boundary conditions for the torus, sphere, and cube.

Dirichlet BVPs, mixed BVPs can be solved with our without the HSBIE. We refer to the former method as SBIE/HSBIE and to the latter one SBIE/SBIE. In the SBIE/HSBIE, the natural domain for the HSBIE is Γ_D, as in Dirichlet BVPs, while the SBIE is natural for Γ_N. In the SBIE/SBIE, the SBIE must be

applied in its unnatural domain Γ_D. In terms of linear algebra, SBIE/HSBIE allows one to avoid inverting matrices with unfavorable spectral properties.

Figure 3.10 and Table 3.6 present the iteration counts for the mixed BVPs for the three shapes. It is clear that (i) the SBIE/HSBIE is superior to SBIE/SBIE, and (ii) the iteration counts grow with mesh-refinement for all three problems; for the SBIE/HSBIE scheme, the iteration counts grow logarithmically with h^{-1}. We do not present comparisons for the spectral properties because such comparisons strongly depend on the definition of spectral properties. That is, the spectral properties for the entire matrices are different from those obtained using Schur complements; in contrast, the use of Schur complements has minimal effects on iteration counts.

3.5.6 Discontinuous basis functions

The objective of this section is to demonstrate that discontinuous basis functions are critical for approximating t when it is discontinuous. Those problems include not only non-smooth domains like a cube, but also mixed BVPs defined on smooth domains; in the latter case, t may be discontinuous at the interface between Γ_D and Γ_N. For demonstration purposes, we solved the manufactured pure Dirichlet BVP on the cube. In this problem, t is discontinuous at the edges and vertices because of the discontinuous normal. Further, the normal discontinuity does not allow us to collocate the operators $\frac{1}{2}\mathcal{I} - \mathcal{K}'$ and $\mathcal{D}$ at the edges and vertices. This creates two options: (i) one

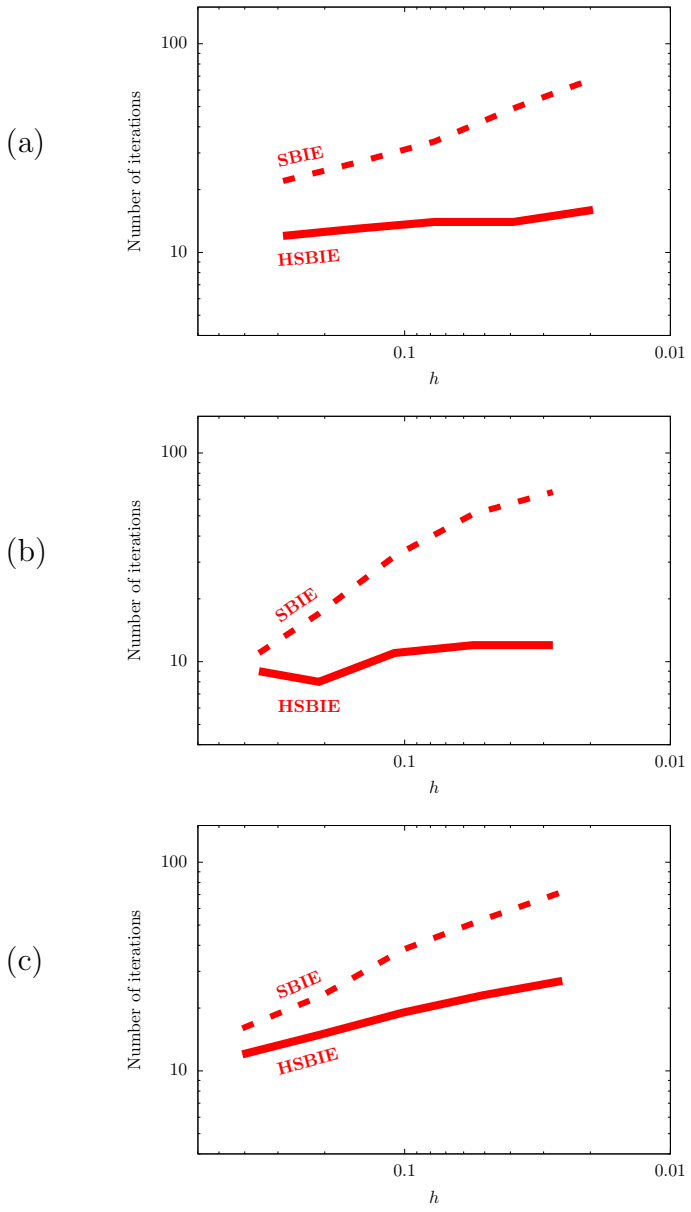

Figure 3.10: Iteration counts of the preconditioned GMRES method for the (a) torus, (b) sphere, and (c) cube.

(a)

h	SBIE/SBIE	SBIE/HSBIE
2.87E-01	22	12
1.51E-01	27	13
7.73E-02	34	14
3.90E-02	49	14
1.96E-02	68	16

(b)

h	SBIE/SBIE	SBIE/HSBIE
3.54E-01	11	9
2.10E-01	17	8
1.09E-01	32	11
5.53E-02	51	12
2.77E-02	65	12

(c)

h	SBIE/SBIE	SBIE/HSBIE
4.08E-01	16	12
2.04E-01	23	15
1.02E-01	38	19
5.10E-02	53	23
2.55E-02	72	27

Table 3.6: Iteration counts of the preconditioned GMRES method for the (a) torus, (b) sphere, and (c) cube.

can use the SBIE with either continuous or discontinuous basis functions, or (ii) one can use either the SBIE or HSBIE with discontinuous basis functions because they require collocation points off the edges and vertices. We pursue the first option as it allows us to compare continuous versus discontinuous basis functions.

Figure 3.11 and Table 3.7 present the $L^2(\Gamma)$-error of $\tilde{t}_h$ for two approximations, one involves only continuous basis functions and the other only discontinuous ones. It is clear that for the continuous basis functions $\tilde{t}_h$ converges very slowly. In contrast, for the discontinuous basis functions, $\tilde{t}_h$ converges at the optimal rate and delivers very accurate solutions.

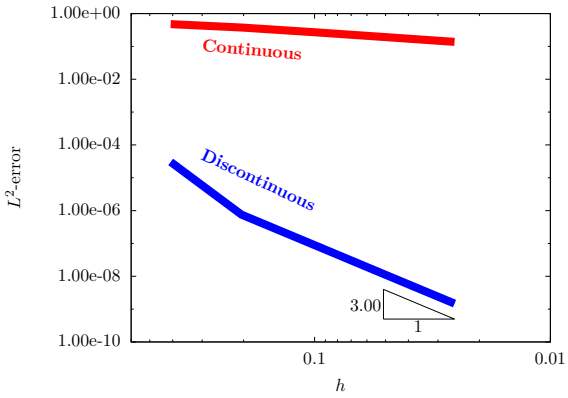

Figure 3.11: $L^2(\Gamma)$-errors for two approximations, with and without the discontinuous basis functions.

	Continuous			Discontinuous		
h	N_{Keval}	L^2-error	eoc	N_{Keval}	L^2-error	eoc
4.08E-01	1.20E+05	3.04E-05		2.80E+04	4.78E-01	
2.04E-01	1.20E+06	7.52E-07	5.33	5.19E+05	3.75E-01	0.35
1.02E-01	7.74E+06	9.46E-08	2.99	4.81E+06	2.72E-01	0.46
5.10E-02	4.39E+07	1.18E-08	3.00	3.36E+07	1.94E-01	0.49
2.55E-02	2.90E+08	1.48E-09	3.00	2.52E+08	1.37E-01	0.50

Table 3.7: $L^2(\Gamma)$-errors for two approximations, with and without the discontinuous basis functions.

3.5.7 Approximations for mixed boundary-value problems

In approximation theory for BIEs, it is well established that for mixed boundary-value problems one should use different approximations for the Cauchy data u and t. In particular, to attain the optimal convergence rate for the Cauchy data, approximations for u should be one degree higher than those for t [103]. In this section, we present numerical results supporting this statement. Further, we present results suggesting that approximations of the same degree are capable of delivering the optimal convergence rate for the torus and sphere.

For demonstration purposes, we considered the same mixed BVPs as in Section 3.5.5. These problems were solved using the SBIE/HSBIE scheme, discontinuous basis functions for approximating t, and continuous regular ($p = 2$) and degree elevated ($p = 3$) basis functions for approximating u. Figure 3.12 and Table 3.8 present the $L^2(\Gamma)$-errors obtained using regular basis functions for u. It is clear that the $L^2(\Gamma)$-error for u converges optimally for all three cases. In contrast, the rate of convergence for t is optimal for the torus and sphere,

but not for the cube. Perhaps the results for the torus and sphere are more surprising than those for the cube, as we expected suboptimal convergence rates for t for all three cases.

Figure 3.13 and Table 3.9 present the $L^2(\Gamma)$-errors obtained using degree elevated basis functions for u.

It is clear that in all three cases the $L^2(\Gamma)$-errors for both u and t exhibit optimal convergence rates. Note that for the cube the errors corresponding to the degree elevated basis functions are significantly smaller than those corresponding to the regular basis functions. For the torus and sphere, the errors in u corresponding to the degree elevated basis functions are also significantly smaller than those corresponding to the regular basis functions, which is not surprising simply because we used higher-order approximations. In contrast, for the torus and sphere, the degree elevated approximation for u had a minor impact on the errors for t.

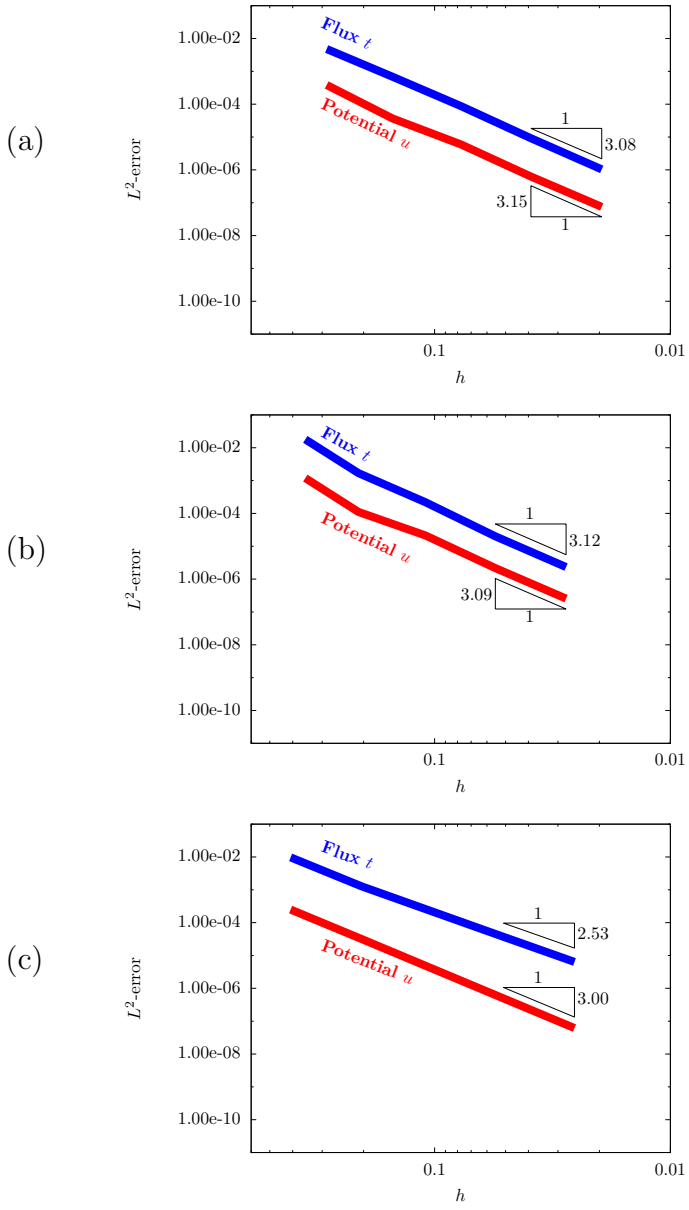

Figure 3.12: $L^2(\Gamma)$-errors for the flux t and potential u on the (a) torus (b) sphere, and (c) cube. The approximations involved continuous basis functions degree $p = 2$ for u and discontinuous basis functions of degree $p = 2$ for t.

(a)

		Flux		Potential	
h	N_{Keval}	L^2-error	eoc	L^2-error	eoc
2.87E-01	9.26E+05	4.80E-03		3.85E-04	
1.51E-01	6.04E+06	6.82E-04	3.02	3.65E-05	3.65
7.73E-02	3.30E+07	8.74E-05	3.08	5.96E-06	2.72
3.90E-02	1.80E+08	9.21E-06	3.29	6.28E-07	3.29
1.96E-02	1.35E+09	1.04E-06	3.15	7.48E-08	3.08

(b)

		Flux		Potential	
h	N_{Keval}	L^2-error	eoc	L^2-error	eoc
3.54E-01	2.05E+05	1.80E-02		1.19E-03	
2.10E-01	1.54E+06	1.68E-03	4.56	1.11E-04	4.57
1.09E-01	1.21E+07	2.20E-04	3.11	2.14E-05	2.51
5.53E-02	7.93E+07	2.01E-05	3.51	2.16E-06	3.37
2.77E-02	5.55E+08	2.33E-06	3.12	2.55E-07	3.09

(c)

		Flux		Potential	
h	N_{Keval}	L^2-error	eoc	L^2-error	eoc
4.08E-01	8.40E+04	9.70E-03		2.50E-04	
2.04E-01	8.94E+05	1.28E-03	2.92	3.17E-05	2.98
1.02E-01	6.31E+06	2.17E-04	2.56	3.97E-06	3.00
5.10E-02	3.86E+07	3.70E-05	2.55	4.95E-07	3.00
2.55E-02	2.69E+08	6.38E-06	2.53	6.18E-08	3.00

Table 3.8: $L^2(\Gamma)$-errors for the flux t and potential u on the (a) torus (b) sphere, and (c) cube. The approximations involved continuous basis functions degree $p = 2$ for u and discontinuous basis functions of degree $p = 2$ for t.

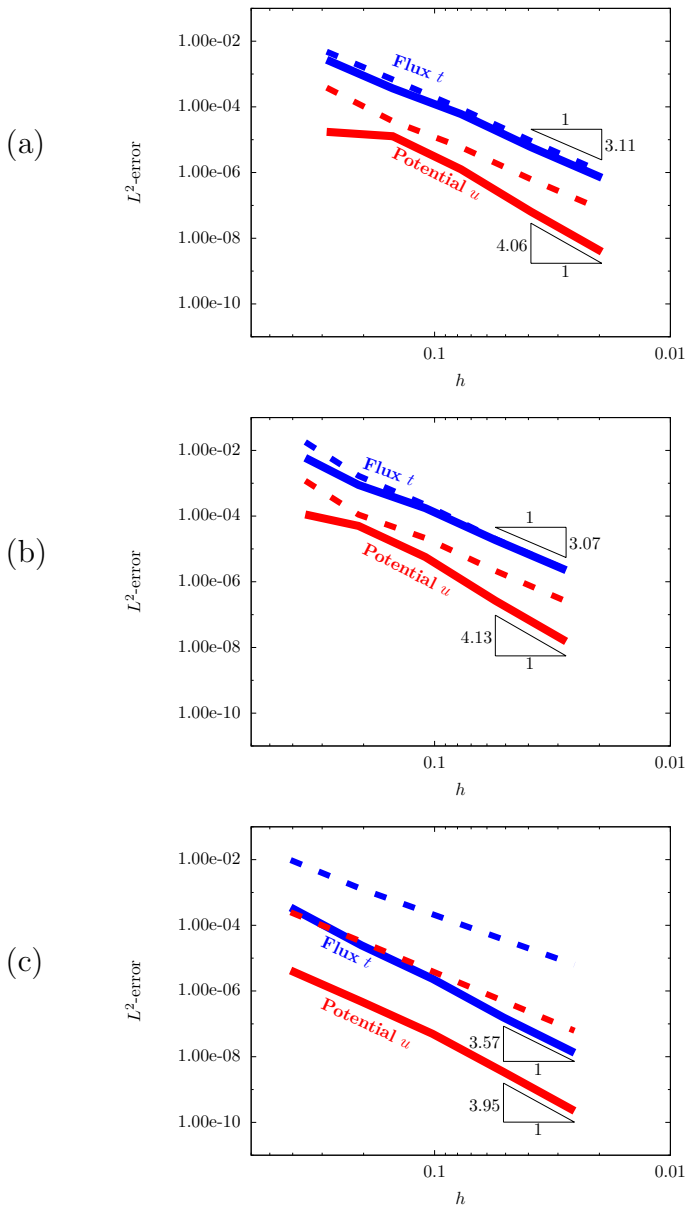

Figure 3.13: $L^2(\Gamma)$-errors for the flux t and potential u on the (a) torus (b) sphere, and (c) cube. The approximations involved continuous basis functions of degree $p = 3$ for u and discontinuous basis functions of degree $p = 2$ for t (solid lines). The dashed lines correspond to the results presented in Figure 3.12.

(a)

		Flux		Potential	
h	N_{Kevanl}	L^2-error	eoc	L^2-error	eoc
2.87E-01	2.58E+06	2.72E-03		1.73E-05	
1.51E-01	1.31E+07	3.66E-04	3.11	1.28E-05	0.46
7.73E-02	5.76E+07	6.04E-05	2.70	1.26E-06	3.48
3.90E-02	2.87E+08	5.97E-06	3.39	6.44E-08	4.35
1.96E-02	2.10E+09	6.96E-07	3.11	3.89E-09	4.06

(b)

		Flux		Potential	
h	N_{Kevanl}	L^2-error	eoc	L^2-error	eoc
3.54E-01	4.94E+05	5.93E-03		1.12E-04	
2.10E-01	3.36E+06	8.88E-04	3.65	5.03E-05	1.53
1.09E-01	2.16E+07	1.74E-04	2.49	5.66E-06	3.34
5.53E-02	1.31E+08	1.87E-05	3.27	2.66E-07	4.48
2.77E-02	8.39E+08	2.25E-06	3.07	1.53E-08	4.13

(c)

		Flux		Potential	
h	N_{Kevanl}	L^2-error	eoc	L^2-error	eoc
4.08E-01	2.16E+05	3.49E-04		4.21E-06	
2.04E-01	2.23E+06	2.45E-05	3.83	4.73E-07	3.15
1.02E-01	1.17E+07	2.35E-06	3.38	4.99E-08	3.25
5.10E-02	6.14E+07	1.56E-07	3.91	3.43E-09	3.86
2.55E-02	4.01E+08	1.32E-08	3.57	2.23E-10	3.95

Table 3.9: $L^2(\Gamma)$-errors for the flux t and potential u on the (a) torus (b) sphere, and (c) cube. The approximations involved continuous basis functions degree $p = 3$ for u and discontinuous basis functions of degree $p = 2$ for t (solid lines). The dashed lines correspond to the results presented in Figure 3.12.

Chapter 4

Equations of linear elasticity

4.1 Introduction

In this Chapter we extend the results of Chapter 3 to the equations of classical linear elasticity. We introduce the BIEs associated with the partial differential equations of linear elasticity, and show that all boundary integral operators can be evaluated using weakly-singular integrals only. We consider collocation discretizations of these BIEs for interior and exterior BVPs with mixed boundary conditions. In contrast to Chapter 3, we do not present any numerical examples in this chapter. Rather we will present numerical examples in Chapter 5, where we describe boundary element patch tests.

4.2 Continuous Formulation

4.2.1 Model boundary-value problem

Consider a bounded domain $\Omega \subset \mathbb{R}^3$ with $\Gamma = \partial\Omega$. We assume that $\Gamma \in \tilde{C}^2$. The model BVP in this chapter is formulated for the equations of classical linear elasticity written in Navier's form:

$$-u_{i,jj} + (\lambda + \mu)u_{j,ij} = 0 \quad \text{on } \Omega\,. \tag{4.1}$$

Here u_i is the displacement vector and λ and μ are Lamé's constants. Here we use the standard notation which implies summation over repeated indices and differentiation with respect to the indices following commas. For our purposes, it is also useful to introduce Poisson's ratio

$$\nu = \frac{\lambda}{2(\lambda + \mu)}.$$

The boundary conditions include Dirichlet data prescribed for the displacement vector

$$u_i = g_i \quad \text{on } \Gamma_D^i, \tag{4.2}$$

and Neumann data prescribed for the traction vector

$$t_i := \mu(u_{i,j} + u_{j,i})n_j + \lambda u_{j,j} n_i = h_i \quad \text{on } \Gamma_N^i\,. \tag{4.3}$$

Here we use the notation Γ_D^i and Γ_N^i rather than Γ_D and Γ_N to emphasize that boundary conditions at a point may involve both Dirichlet and Neumann data. For example, boundary conditions at a point may be $u_1 = 0$, $t_2 = 0$, and $t_3 = 0$. Further, for simplicity of notation, we state boundary conditions using global Cartesian components. It is often the case that boundary conditions are imposed in local coordinates, aligned with the outward normal and tangent vectors. For example, boundary conditions imposed by a smooth plane are $u_{1'} = 0$, $t_{2'} = 0$, and $t_{3'} = 0$, where the $1'$ axis is normal to the plane, and $2'$ and $3'$ axes are in the plane. Of course $\overline{\Gamma_D^i \cup \Gamma_N^i} = \Gamma$ and $\Gamma_D^i \cap \Gamma_N^i = \emptyset$.

Further, we define the Dirichlet-to-Neumann map

$$t_i(x) = \gamma_{ij}\left[u_j(x), x\right] := \left\{ n_k(x)\left[\mu\left(\delta_{ij}\delta_{kl} + \delta_{jk}\delta_{il}\right) + \lambda\delta_{ik}\delta_{jl}\right]\frac{\partial}{\partial x_l}\right\} u_j(x)$$

which maps u_i onto t_i.

4.2.2 Integral equations

Similar to Laplace's equation, the integral equations equivalent to (4.1)-(4.3) are well-known. They involve a representation formula that allows one to determine the solution u_i in terms of the Cauchy boundary data (u_i, t_i):

$$u_i(x) = \int_\Gamma U_{ij}(x,y)t_j(y)ds_y - \int_\Gamma \gamma_{ik}\left[U_{kj}(x,y), y\right]u_j(y)ds_y \tag{4.4}$$

where

$$U_{ij}(x,y) = \frac{1}{4\pi\mu(1-\nu)}\left[(3-4\nu)\frac{\delta_{ij}}{|x-y|} + \frac{(y_i - x_i)(y_j - x_j)}{|x-y|^3}\right]$$

is the fundamental solution of linear elasticity. Similar to Laplace's equation, the Cauchy data can be reconstructed using either the SBIE

$$\left[\sigma_{ij}\mathcal{I} + \mathcal{K}_{ij}\right]u_j = \mathcal{V}_{ij}t_j \quad \text{on } \Gamma$$

or the HSBIE

$$\left[(\delta_{ij} - \sigma_{ij})\mathcal{I} - \mathcal{K}'_{ij}\right]t_j = \mathcal{D}_{ij}u_j \quad \text{on } \Gamma.$$

Here, $\mathcal{I}$ is the identity,

$$\mathcal{V}_{ij}t_j(x) = \int_\Gamma U_{ij}(x,y)t_j(y)ds_y, \quad x \in \Gamma$$

is the single-layer operator,

$$\mathcal{K}_{ij}u_j(x) = \int_\Gamma \gamma_{ik}\left[U_{kj}(x,y),y\right]u_j(y)ds_y, \quad x \in \Gamma$$

is the double-layer operator,

$$\mathcal{K}'_{ij}t_j(x) = \int_\Gamma \gamma_{ik}\left[U_{kj}(x,y),x\right]t_j(y)ds_y, \quad x \in \Gamma$$

is the adjoint double-layer operator,

$$\mathcal{D}_{ij}u_j(x) = -\int_\Gamma \gamma_{ik}\left\{\gamma_{kl}\left[U_{lj}(x,y),y\right],x\right\}u_j(y)ds_y, \quad x \in \Gamma$$

is the hyper-singular operator, and

$$\sigma_{ij}(x) = -\int_\Gamma \gamma_{ik}\left[U_{kj}(x,y),y\right]ds_y, \quad x \in \Gamma.$$

To formulate BIEs for the mixed BVP, we assume that $\tilde{g}_i$ and $\tilde{h}_i$ are extensions of g_i and h_i onto the entire Γ such that $\tilde{g}_i|_{\Gamma_D^i} = g_i$ and $\tilde{h}_i|_{\Gamma_N^i} = h_i$. Then the Dirichlet data u_i and the Neumann data t_i can be represented as

$$u_i = \tilde{u}_i + \tilde{g}_i \tag{4.5}$$

and

$$t_i = \tilde{t}_i + \tilde{h}_i, \tag{4.6}$$

where $\tilde{u}_i|_{\Gamma_D^i} = \tilde{t}_i|_{\Gamma_N^i} = 0$. In Chapter 3 we have established that for the mixed BVP for Laplace's equation, one should choose the extensions such that $\tilde{g}_i$ is

continuous and $\tilde{h}_i$ is discontinuous at the interface between Γ_D^i and Γ_N^i. To this end, we assume that $\tilde{g}_i$ and $\tilde{u}_i$ are continuous at the interface and we simply set $\tilde{h}_i|_{\Gamma_D^i} = 0$. Then the SBIE and the HSBIE can be rewritten as

$$\mathcal{V}_{ij}\tilde{t}_j - [\sigma_{ij}\mathcal{I} + \mathcal{K}_{ij}]\,\tilde{u}_j = f_i^S \quad \text{on } \Gamma \tag{4.7}$$

and

$$\left[(\delta_{ij} - \sigma_{ij})\mathcal{I} - \mathcal{K}'_{ij}\right]\tilde{t}_j - \mathcal{D}_{ij}\tilde{u}_j = f_i^H \quad \text{on } \Gamma, \tag{4.8}$$

respectively where

$$f_i^H = [\sigma_{ij}\mathcal{I} + \mathcal{K}_{ij}]\,\tilde{g}_j - \mathcal{V}_{ij}\tilde{h}_j,$$
$$f_i^S = \mathcal{D}_{ij}\tilde{g}_j - \left[(\delta_{ij} - \sigma_{ij})\mathcal{I} - \mathcal{K}'_{ij}\right]\tilde{h}_j.$$

Note that the extension $\tilde{g}_i$ is not uniquely defined. However, (4.5) and (4.6) are structured so that u_i and t_i are uniquely defined as long as (4.7) and (4.8) are uniquely solvable for $\tilde{u}_i$ and $\tilde{t}_i$.

Remark 4.2.1. *The solution of a pure Dirichlet problem ($\Gamma_D^i = \Gamma$ for all $i = 1, 2, 3$) can be obtained by setting $\tilde{g}_i = g_i$ and $\tilde{u}_i = \tilde{h}_i = 0$. A solution of a pure Neumann problem ($\Gamma_N^i = \Gamma$ for all $i = 1, 2, 3$) can be obtained by setting $\tilde{h}_i = h_i$ and $\tilde{t}_i = \tilde{g}_i = 0$.*

Remark 4.2.2. *For exterior boundary value problems, BIEs can be derived in the same manner. In this case, the Cauchy data can be reconstructed using the SBIE*

$$(\sigma_{ij}\mathcal{I} - \mathcal{K}_{ij})\,u_j = -\mathcal{V}_{ij}t_j + u_i^0 \quad \text{on } \Gamma \tag{4.9}$$

or the HSBIE

$$\left[(\delta_{ij}-\sigma_{ij})\mathfrak{I}+\mathcal{K}'_{ij}\right]t_j=\mathcal{D}_{ij}u_j+t_i^0 \quad \text{on } \Gamma. \tag{4.10}$$

Here, u_i^0 and u_i^0 are the leading order terms of the corresponding far-field asymptotic approximations. Typically,

$$u_i^0(x)=\mathcal{O}\left(|x|^{-1}\right) \quad \text{and} \quad t_i^0(x)=\mathcal{O}\left(|x|^{-2}\right)$$

or

$$u_i^0(x)=\mathcal{O}\left(|x|\right) \quad \text{and} \quad t_i^0(x)=\mathcal{O}\left(1\right).$$

Remark 4.2.3. *The double-layer operators $\mathcal{K}_{ij}$ and $\mathcal{K}'_{ij}$ are not compact for the equations of linear elasticity, not even for C^∞-surfaces. Consequently, there is no direct extension of the mathematical analysis for the BIEs of Laplace's equation to the equations of linear elasticity.*

4.3 Collocation discretization

Let us consider the mixed BVP. Approximations of $\tilde{u}_i$ and $\tilde{t}_i$ are constructed as

$$\tilde{u}_i^h(x)=\sum_{A=1}^{n^{D,i}}\underline{\tilde{u}}_i[A]N_A^{D,i}(x), \quad \text{and} \quad \tilde{t}_i^h(x)=\sum_{A=1}^{n^{N,i}}\underline{\tilde{t}}_i[A]N_A^{N,i}(x),$$

respectively, where $N_A^{D,i}$ and $N_A^{N,i}$ are the basis functions and $\underline{\tilde{u}}_i$ and $\underline{\tilde{t}}_i$ are column-vectors. In the same way as for Laplace's equation, the basis functions are such that $N_A^{D,i}(x)=0$ for $x\in\Gamma_D^i$ and $N_A^{N,i}=0$ for $x\in\Gamma_N^i$ and we define collocation points $x_A^{D,i}\in\Gamma_N^i$ and $x_A^{N,i}\in\Gamma_D^i$.

Upon collocating (4.7) at $x_A^{D,i}$ and (4.8) at $x_A^{N,i}$, one generates the system of linear algebraic equations for $\underline{\tilde{u}}_i$ and $\underline{\tilde{t}}_i$:

$$V\underline{\tilde{t}} - \left(\Sigma^D + K\right)\underline{\tilde{u}} = \underline{f}^S \tag{4.11}$$

and

$$\left[\left(I^N - \Sigma^N\right) - K'\right]\underline{\tilde{t}} - D\underline{\tilde{u}} = \underline{f}^H. \tag{4.12}$$

Here the system matrices are defined as

$$V = \begin{pmatrix} V_{11} & V_{12} & V_{13} \\ V_{21} & V_{22} & V_{23} \\ V_{31} & V_{32} & V_{33} \end{pmatrix}, \quad D = \begin{pmatrix} D_{11} & D_{12} & D_{13} \\ D_{21} & D_{22} & D_{23} \\ D_{31} & D_{32} & D_{33}, \end{pmatrix},$$
$$\Sigma^D = \begin{pmatrix} \Sigma_{11}^D & \Sigma_{12}^D & \Sigma_{13}^D \\ \Sigma_{21}^D & \Sigma_{22}^D & \Sigma_{23}^D \\ \Sigma_{31}^D & \Sigma_{32}^D & \Sigma_{33}^D \end{pmatrix}, \quad K = \begin{pmatrix} K_{11} & K_{12} & K_{13} \\ K_{21} & K_{22} & K_{23} \\ K_{31} & K_{32} & K_{33} \end{pmatrix},$$
$$\Sigma^N = \begin{pmatrix} \Sigma_{11}^N & \Sigma_{12}^N & \Sigma_{13}^N \\ \Sigma_{21}^N & \Sigma_{22}^N & \Sigma_{23}^N \\ \Sigma_{31}^N & \Sigma_{32}^N & \Sigma_{33}^N \end{pmatrix}, \quad K' = \begin{pmatrix} K'_{11} & K'_{12} & K'_{13} \\ K'_{21} & K'_{22} & K'_{23} \\ K'_{31} & K'_{32} & K'_{33} \end{pmatrix},$$
$$I^N = \begin{pmatrix} I_{11}^N & 0 & 0 \\ 0 & I_{22}^N & 0 \\ 0 & 0 & I_{33}^N \end{pmatrix},$$

and the vectors are defined as

$$\underline{\tilde{u}} = \begin{pmatrix} \underline{\tilde{u}}_1 \\ \underline{\tilde{u}}_2 \\ \underline{\tilde{u}}_3 \end{pmatrix}, \quad \underline{\tilde{t}} = \begin{pmatrix} \underline{\tilde{t}}_1 \\ \underline{\tilde{t}}_2 \\ \underline{\tilde{t}}_3 \end{pmatrix}, \quad \underline{f}^S = \begin{pmatrix} \underline{f}_1^S \\ \underline{f}_2^S \\ \underline{f}_3^S \end{pmatrix}, \quad \underline{f}^H = \begin{pmatrix} \underline{f}_1^H \\ \underline{f}_2^H \\ \underline{f}_3^H \end{pmatrix}.$$

The components of the system matrices are defined as

$$\Sigma_{ij}^D[A,B] = \sigma_{ij}(x_A^{D,i}) N_B^{D,j}(x_A^{D,i}),$$
$$\Sigma_{ij}^N[A,B] = \sigma_{ij}(x_A^{N,i}) N_B^{N,j}(x_A^{D,i}),$$
$$I_{ii}^N[A,B] = N_B^{N,i}(x_A^{D,i}),$$

and

$$
\begin{aligned}
V_{ij}[A,B] &= \mathcal{V}_{ij} N_B^{N,j}(x_A^{D,i}) \\
&= \int_\Gamma U_{ij}(x_A^{D,i}, y) N_B^{N,j}(y) ds_y, \\
K_{ij}[A,B] &= \mathcal{K}_{ij} N_B^{D,j}(x_A^{D,i}) \\
&= \int_\Gamma \gamma_{ik} \left[U_{kj}(x_A^{D,i}, y), y \right] N_B^{D,j}(y) ds_y, \\
K'_{ij}[A,B] &= \mathcal{K}'_{ij} N_B^{N,j}(x_A^{N,i}) \\
&= \int_\Gamma \gamma_{ik} \left[U_{kj}(x_A^{N,i}, y), x_A^{N,i} \right] N_B^{N,j}(y) ds_y, \\
D_{ij}[A,B] &= \mathcal{D}_{ij} N_B^{D,j}(x_A^{N,i}) \\
&= -\int_\Gamma \gamma_{ik} \left\{ \gamma_{kl} \left[U_{lj}(x_A^{N,i}, y), y \right], x_A^{N,i} \right\} N_B^{D,j}(y) ds_y.
\end{aligned}
$$

Note that in these definitions we do not sum over the indices i and j but we do sum over the indices k and l. The components of the right-hand-side vectors are defined as

$$
\begin{aligned}
\underline{f}_i^S[A] &:= f_i^S(x_A^{D,i}) \\
&= \sigma_{ij}(x_A^{D,i}) \tilde{g}_j(x_A^{D,i}) + \mathcal{K}_{ij} \tilde{g}_j(x_A^{D,i}) - \mathcal{V}_{ij} \tilde{h}_j(x_A^{D,i}), \\
\underline{f}_i^H[A] &:= f_i^H(x_A^{N,i}) \\
&= \mathcal{D}_{ij} \tilde{g}_j(x_A^{N,i}) - \left[\delta_{ij} - \sigma_{ij}(x_A^{N,i}) \right] \tilde{h}_j(x_A^{N,i}) + \mathcal{K}'_{ij} \tilde{h}_j(x_A^{N,i}),
\end{aligned}
$$

where summation is carried out over j but not over i.

Note that the system of governing linear algebraic equations is constructed so that one inverts matrices associated with the double layer potential and the

adjoint double layer potential. We have proved in Chapter 3 that this results in optimally conditioned systems of linear algebraic equations for harmonic problems. This result can be directly extended to linear elastic problems.

For a pure Dirichlet problem, all collocation points are $x_A^{N,i}$, and therefore it is sufficient to solve (4.12) by setting $\tilde{u}_i^h = 0$, $\tilde{h}_i = 0$ and $\tilde{g}_i = g_i$:

$$\left[\left(I^N - \Sigma^N\right) - K'\right] \underline{\tilde{t}} = \underline{f}_H.$$

For the pure Neumann problem, all collocation points are $x_A^{D,i}$, and therefore it is sufficient to solve (4.11) by setting $\tilde{t}_i^h = 0$, $\tilde{g}_i = 0$ and $\tilde{h}_i = h_i$:

$$-\left(\Sigma^D + K\right) \underline{\tilde{u}} = \underline{f}_S.$$

It is well-known that the pure Neumann problem is only uniquely solvable up to rigid body motions. This is reflected in the fact that the matrix $\Sigma^D + K$ is not invertible. To overcome this issue, it is standard to regularize the system of linear equations by enforcing the conditions

$$\int_\Gamma \tilde{u}_1^h(y) ds_y = \int_\Gamma \tilde{u}_2^h(y) ds_y = \int_\Gamma \tilde{u}_3^h(y) ds_y = 0$$

and

$$\begin{aligned}
\int_\Gamma \left[\tilde{u}_1^h(y) y_2 - \tilde{u}_2^h(y) y_1\right] ds_y = 0, \\
\int_\Gamma \left[\tilde{u}_2^h(y) y_3 - \tilde{u}_3^h y_2\right] ds_y = 0, \\
\int_\Gamma \left[\tilde{u}_3^h(y) y_1 - \tilde{u}_1^h(y) y_3\right] ds_y = 0.
\end{aligned}$$

We incorporate these six conditions into the system of linear algebraic equations using Lagrange multipliers. Similarly, for mixed BVPs where $\Gamma_N^i = \Gamma$ for some but not all components i, the system of linear equations is regularized using an appropriate subset of these six conditions.

For exterior BVPs, a system of linear algebraic equations can be obtained upon collocating (4.9) and (4.10):

$$V\tilde{\underline{t}} + \left(\Sigma^D - K\right)\tilde{\underline{u}} = \underline{f}^{S,\text{ext}}, \tag{4.13}$$

and

$$\left[\left(I^N - \Sigma^N\right) + K'\right]\tilde{\underline{t}} - D\tilde{\underline{u}} = \underline{f}^{H,\text{ext}}, \tag{4.14}$$

where

$$\underline{f}^{S,\text{ext}} = \begin{pmatrix} \underline{f}_1^{S,\text{ext}} \\ \underline{f}_2^{S,\text{ext}} \\ \underline{f}_3^{S,\text{ext}} \end{pmatrix}, \quad \underline{f}^{H,\text{ext}} = \begin{pmatrix} \underline{f}_1^{H,\text{ext}} \\ \underline{f}_2^{H,\text{ext}} \\ \underline{f}_3^{H,\text{ext}} \end{pmatrix}$$

with the components

$$\begin{aligned}
\underline{f}_i^{S,\text{ext}}[A] &:= f_i^{S,\text{ext}}(x_A^{D,i}) \\
&= -\mathcal{V}_{ij}\tilde{h}_j(x_A^{D,i}) - \sigma_{ij}(x_A^{D,i})\tilde{g}_j(x_A^{D,i}) + \mathcal{K}_{ij}\tilde{g}_j(x_A^{D,i}) + u_i^0(x_A^{D,i}), \\
\underline{f}_i^{H,\text{ext}}[A] &:= f_i^{H,\text{ext}}(x_A^{N,i}) \\
&= \mathcal{D}_{ij}\tilde{g}_j(x_A^{N,i}) - \left[\delta_{ij} - \sigma_{ij}(x_A^{N,i})\right]\tilde{h}_j(x_A^{N,i}) - \mathcal{K}'_{ij}\tilde{h}_j(x_A^{N,i}) + t_i^0(x_A^{N,i}).
\end{aligned}$$

Note that for these definitions summation is carried out over j but not over i. Similar to the pure Neumann problem for the interior BVP, the operator

$(I^N - \Sigma^N) + K'$ is not invertible. However, the traction vector t_i^h has to satisfy the solvability conditions

$$\int_\Gamma t_1^h(y)ds_y = \int_\Gamma t_2^h(y)ds_y = \int_\Gamma t_3^h(y)ds_y = 0$$

and

$$\begin{aligned}
\int_\Gamma \left[t_1^h(y)y_2 - t_2^h(y)y_1\right] ds_y = 0,\\
\int_\Gamma \left[t_2^h(y)y_3 - t_3^h y_2\right] ds_y = 0,\\
\int_\Gamma \left[t_3^h(y)y_1 - t_1^h(y)y_3\right] ds_y = 0.
\end{aligned}$$

We incorporate these six conditions into the system of linear algebraic equations using Lagrange multipliers which results in an invertible system matrix.

Remark 4.3.1. *We have introduced our discretization for the components $i = 1, 2, 3$. In the same way, one can also use the normal and the two tangential components. This can be particularly useful in applications that involve boundary conditions for the normal or the tangential components.*

4.4 Regularization of operators

Similar to Laplace's equation, the SBIE and the HSBIE associated with the equations of linear elasticity involve weakly-singular, singular and hypersingular integrals. In this section we establish that the evaluation of all integral operators at a point $x \in \Gamma$ can be reduced to the evaluation of weakly-singular integrals.

The single-layer operator is naturally weakly singular; while the same is true for the double-layer operators associated with Laplace's equations, this is not true for the double-layer operators associated with the equations of linear elasticity. Nevertheless, it can be easily seen that

$$\sigma_{ij} + \mathcal{K}_{ij} 1 = 0, \quad \text{for all } i, j = 1, 2, 3$$

and therefore

$$\left(\sigma_{ij} + \mathcal{K}_{ij}\right) u_j(x) = \int_\Gamma \gamma_{ik} \left[U_{kj}(x, y), y\right] \left[u_j(y) - u_j(x)\right] ds_y$$

for all $i, j = 1, 2, 3$. If u_j is Lipschitz continuous, so that

$$|u_j(y) - u_j(x)| < C|y - x|,$$

then the integral becomes weakly singular. This additional restriction on $u_j(x)$ does not pose problems within the context of IgA and therefore we have shown that the double layer potential can also be reduced to the evaluation of a weakly-singular integral.

To regularize the adjoint double-layer operator associated with the equations of linear elasticity, we first note that for all $i, j = 1, 2, 3$

$$\left|\gamma_{ik} \left[U_{kj}(x, y), y\right] - \gamma_{ik} \left[U_{kj}(x, y), x\right]\right| \leq \frac{C}{|x - y|}. \tag{4.15}$$

Then the adjoint double-layer operator can be expressed as

$$\begin{aligned}
&\left(\left(\delta_{ij} - \sigma_{ij}\right) - \mathcal{K}'_{ij}\right) t_j(x) = \\
&\quad = -\int_\Gamma \left\{\gamma_{ik} \left[U_{kj}(x, y), x\right] - \gamma_{ik} \left[U_{kj}(x, y), y\right]\right\} t_j(y) ds_y \\
&\qquad + t_i(x) - \left(\sigma_{ij} + \mathcal{K}_{ij}\right) t_j(x).
\end{aligned}$$

The first integral is weakly-singular because of (4.15). We have already seen that $(\sigma_i\delta_{ij} + \mathcal{K}_{ij})\, t_j(x)$ is weakly-singular as long as t_j is Lipschitz continuous in the vicinity of x. While this is not true for all $x \in \Gamma$, it is easy to see that this is true as long as x is on a smooth part of a $\tilde{C}^2$-surface.

To regularize the hyper-singular operator, we begin with approximating u_j in the vicinity of x by a Taylor expansion:

$$u_j(y) = u_j(x) + (\nabla_T u_j)(x) \cdot (y - x) + \mathcal{O}(|x - y|^2). \tag{4.16}$$

Note that this expansion is only valid if u_j is smooth in the vicinity of x. This can be assumed as long as x is on a smooth part of a $\tilde{C}^2$-surface. Then the hyper-singular operator can be rewritten as

$$\begin{aligned}
\mathcal{D}_{ij}u_j(x) &= -\int_\Gamma \gamma_{ik}\left\{\gamma_{kl}\left[U_{lj}(x,y),y\right]\right\} u_j(y) ds_y \\
&= -\int_\Gamma \gamma_{ik}\left\{\gamma_{kl}\left[U_{lj}(x,y),y\right]\right\} \left[u_j(y) - u_j(x) - (\nabla_T u_j)(x)\cdot(y-x)\right] ds_y \\
&\quad - u_j(x)\int_\Gamma \gamma_{ik}\left\{\gamma_{kl}\left[U_{lj}(x,y),y\right]\right\} ds_y \\
&\quad - \int_\Gamma \gamma_{ik}\left\{\gamma_{kl}\left[U_{lj}(x,y),y\right]\right\} (\nabla_T u_j)(x)\cdot(y-x) ds_y.
\end{aligned}$$

Since constant and linear functions are trivial solutions of the equations of linear elasticity, the HSBIE implies that

$$-\int_\Gamma \gamma_{ik}\left\{\gamma_{kl}\left[U_{lj}(x,y),y\right]\right\} ds_y = 0$$

and

$$-\int_\Gamma \gamma_{ik}\left\{\gamma_{kl}\left[U_{lj}(x,y),y\right]\right\} (\nabla_T u_j)(x)(y-x) ds_y = \left((1-\sigma_i)\delta_{ij}\mathcal{I} - \mathcal{K}'_{ij}\right)\bar{t}_j(x)$$

where

$$\bar{t}_j(x) := (\nabla_T u_j)_k(x)\gamma_{kl}\left[(y-x)_l, x\right].$$

Now the hyper-singular operator can be rewritten as

$$\begin{aligned}
&\mathcal{D}_{ij}u_j(x) = \\
&\quad = -\int_\Gamma \gamma_{ik}\left\{\gamma_{kl}\left[U_{lj}(x,y),y\right]\right\}\left[u_j(y) - u_j(x) - (\nabla_T u_j)(x)\cdot(y-x)\right] ds_y \\
&\qquad + \left((1-\sigma_i)\delta_{ij}\mathcal{I} - \mathcal{K}'_{ij}\right)\bar{t}_j(x).
\end{aligned}$$

The first term in this equation is weakly singular because of (4.16). The second term can be evaluated by weakly singular integrals only as long as x is on a smooth part of a $\tilde{C}^2$-surface because it is the adjoint double-layer operator.

In summary, we have established that the SBIE can be evaluated by weakly-singular integrals only if the basis functions $N_A^{D,i}$ are Lipschitz continuous, and the HSBIE can be evaluated by weakly-singular integrals only if, additionally, x is on a smooth part of a $\tilde{C}^2$-surface. In Chapter 3, we have shown that the use of discontinuous basis functions $N_A^{N,i}$ allows one to use collocation points $x_A^{N,i}$ on smooth parts of Γ only. Since the HSBIE only has to be evaluated at the collocation points $x_A^{N,i}$, this shows that the evaluation of all boundary integral operators can be reduced to the evaluation of weakly-singular integrals only.

Chapter 5

Patch Tests for Boundary Element Methods

It is commonly accepted that individual finite elements must be constructed so that they can represent solutions of certain BVPs exactly. A test of this property is known as the Patch Test. In contrast, no Patch Tests have been proposed for BEMs. In this Chapter, we introduce BEM Patch Tests, and demonstrate that they are particularly appealing in the context of IgA. Our presentation is based on the equations of linear elasticity but can be easily extended to other applications.

5.1 Neumann Patch Test

Consider a pure Neumann BVP problem (4.1)-(4.3) with the data

$$t_i(x) = \lambda \alpha_{kk} n_i(x) + \mu(\alpha_{ij} + \alpha_{ji}) n_j(x) \quad x \in \Gamma \,,$$

where α_{ij} is a constant second-rank tensor. A solution of this BVP is

$$u_i(x) = \alpha_{ij} x_j \quad x \in \Omega \,.$$

An approximate solution of this problem can be obtained in two steps. First,

one solves (4.11)

$$-\left(\Sigma^D + K\right)\underline{\tilde{u}} = \underline{f}_S \tag{5.1}$$

for $\underline{\tilde{u}}$. Since for $x \in \Gamma$ $u_i(x)$ is a linear function of x, it can be represented exactly by the basis functions on the entire surface. Then the only errors associated with (5.1) are due to numerical integration. Second, once $\underline{\tilde{u}}$ has been computed, one can compute $u_i(x)$ for $x \in \Omega$ using the representation formula. Note that, again, the only errors at this step are due to numerical integration. Thus one can recover the exact solution as long as all boundary integral operators are evaluated exactly. It is well-known that while boundary integral operators cannot be evaluated exactly in general, it has been established [92] that numerical integration schemes, like the one introduced in Section 3.4, converge exponentially with respect to the number of Gaussian integration points. Thus we say that a BEM implementation passes the Patch Test if it exhibits an exponential convergence with respect to the number of Gaussian integration points.

The introduced Patch Test requires an exact representation of Γ in terms of the basis functions. For restricted classes of surfaces, this is possible for both conventional and isogeometric BEMs. On the other hand, it is clear that the class of surfaces for IBEMs is much larger. In particular, Patch Tests can be performed for any CAD generated surface, which is particularly useful for applications.

5.2 Dirichlet Patch Test

Let u be the solution of the pure Dirichlet problem with the data

$$u_i(x) = \alpha_{ij} x_j \quad x \in \Gamma \,,$$

so that our task is to construct an approximate solution for

$$t_i(x) = \lambda \alpha_{kk} n_i(x) + \mu(\alpha_{ij} + \alpha_{ji}) n_j(x) \quad x \in \Gamma \,.$$

In contrast, to the Neumann problem, the unknown field $t_i(x)$ cannot be exactly represented by the basis functions in general, due to the presence of the normal vector. This means that the numerical solution is affected by both integration and approximation errors. Of course, for a restricted class of surfaces, $n_i(x)$ and consequently $t_i(x)$ can be exactly represented by the basis functions, and therefore the numerical solution is affected by integration errors only. Thus Dirichlet Patch Tests can be conducted by controlling the numerical integration error using more restrictive classes of surfaces. In particular, CAD generated surfaces are not generally suitable for Dirichlet Patch Tests.

The Dirichlet Patch Test can be easily extended to Patch Tests for mixed BVPs. In this case, the surface has to be such that the normal vector can be exactly represented by the basis functions on the Dirichlet part of Γ.

5.3 Numerical examples

5.3.1 Overview

In this section, we present numerical examples demonstrating how the Patch Tests work. All examples involve a sphere and an oblate spheroid, with the aspect ratio equal to 1/2. For the sphere, both the surface and its normal vector can be represented exactly using CAD basis functions. In contrast, for the spheroid, only the surface can be represented exactly using CAD basis functions. In all examples, we chose Young's modulus $E = 1$ and Poisson's ratio $\nu = 1/4$. Both surfaces were parametrized using 8 elements, with commercial tools described in Chapter 6.

5.3.2 Neumann Patch Test

In this section, we present numerical examples for Neumann Patch Tests. For both surfaces, we chose

$$u_1(x) = x_1 + x_2 + x_3,$$
$$u_2(x) = 2x_1 + 2x_2 + 2x_3,$$
$$u_3(x) = 3x_1 + 3x_2 + 3x_3.$$

For the integration scheme we chose $C_a = 5$ and $C_c = 1.01125$. These numbers were determined empirically and no effort was made to optimize them.

Figure 5.1 and Table 5.1 present the results for the sphere and spheroid. The results confirm an exponential convergence for all shapes. Therefore, our im-

plementation passes the Neumann Patch Test for all shapes. Note that we were able to reach machine precision for both shapes.

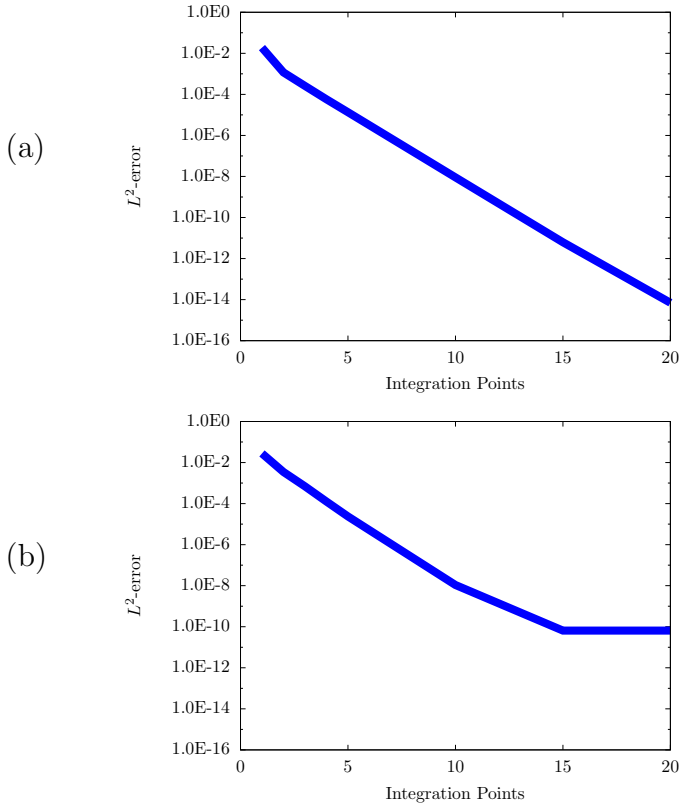

Figure 5.1: Neumann Patch Test for the (a) sphere and (b) spheroid.

5.3.3 Dirichlet Patch Test on canonical shapes

In this section, we present examples for Dirichlet Patch Tests, using the setting described in Section 5.3.2.

Figure 5.2 and Table 5.2 present the results of the Dirichlet Patch Tests for

(a)

Int. Pts.	L^2-error
1	1.90E-02
2	1.17E-03
3	2.59E-04
4	5.76E-05
5	1.35E-05
10	9.02E-09
15	6.25E-12
20	7.02E-15

(b)

Int. Pts.	L^2-error
1	2.77E-02
2	3.48E-03
3	6.91E-04
4	1.25E-04
5	2.37E-05
10	1.08E-08
15	6.52E-11
20	6.48E-11

Table 5.1: Neumann Patch Test for the (a) sphere and (b) spheroid.

the sphere and spheroid. The results show that for the sphere, the solution converges exponentially with respect to the number of integration points. In contrast, the results for the spheroid do not converge to machine precision with respect to the number of integration points. This is because the normal vector cannot be represented as a linear combination of the basis functions on the spheroid. The error therefore stagnates at the approximation error of the normal vector.

5.4 Exterior Problems

Exterior problems involving ellipsoidal cavities present an interesting opportunity for patch testing thanks to a remarkable property valid for elliptical PDEs with constant coefficients. In particular, if a large (infinite) body containing an ellipsoidal cavity is subjected to remote boundary conditions realizing a uniform stress (or strain) field far away from the cavity, then the

(a)

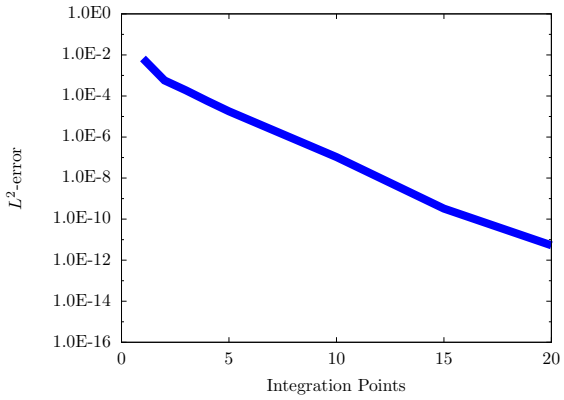

(b)

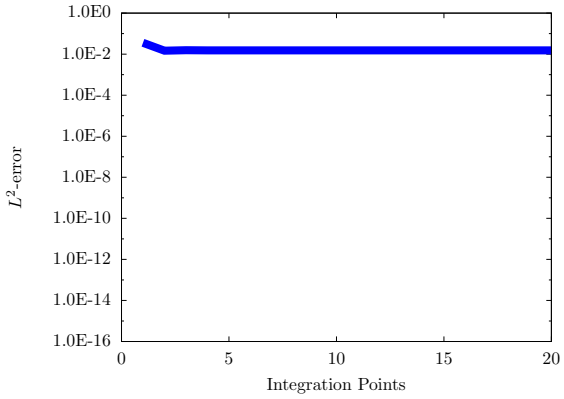

Figure 5.2: Dirichlet Patch Test for the (a) sphere and (b) spheroid.

(a)

Int. Pts.	L^2-error
1	6.68E-03
2	5.73E-04
3	1.88E-04
4	5.64E-05
5	1.79E-05
10	1.06E-07
15	3.26E-10
20	5.32E-12

(b)

Int. Pts.	L^2-error
1	3.58E-02
2	1.47E-02
3	1.56E-02
4	1.53E-02
5	1.53E-02
10	1.53E-02
15	1.53E-02
20	1.53E-02

Table 5.2: Dirichlet Patch Test for the (a) sphere and (b) spheroid.

displacement field on the cavity surface is linear. More generally, a remote polynomial stress (or strain) field induces a polynomial displacement field on the cavity surface. Furthermore, this result can be extended to ellipsoidal cavities filled with elastic materials different from the surrounding one. All of these results are due to Eshelby [44, 45].

As far as patch testing is concerned, exterior problems with ellipsoidal cavities are interesting because a polynomial displacement field on the interior induces a rational field in the domain. In contrast, for interior problems, patch testing involves polynomial boundary data and polynomial fields.

Examples in this section involve spheroidal cavities with the aspect ratios of 0.01., 0.1, 0.5, 1, 2, 10, 100 embedded in an infinite body with $\mu = 1$ and $\nu = 1/4$. The remote stress state is uniaxial tension along the symmetry axis of the cavity. The surfaces were parametrized using 8 elements, independently of the aspect ratio. Extreme cases ($\kappa = 0.01$ and $\kappa = 100$) were chosen to demonstrate the robustness of the integration scheme, and inadequacy of the basic integration scheme for cavities with extreme aspect ratios.

First, let us compute the L_2 error of the surface displacements obtained using the basic integration scheme. For oblate spheroids, the results are presented in Figure 5.3 and Table 5.3, and for prolate Spheroids in Figure 5.4 and Table 5.4. It is clear that all solutions converge exponentially to the exact solution

except the one for the spheroid with $\kappa = 100$. However, it is also clear that the convergence rate significantly deteriorates as the aspect ratio deviates from unity. This error is due to numerical integration only, and its root is the presence of highly curved elements with large aspect ratios. This issue is resolved with the introduction of the subdivision scheme which eliminates elements with high curvature and/or high aspect ratios. For prolate spheroids we chose $C_a = 5$ and $C_c = 1.04$, and for oblate spheroids we chose $C_a = 5$ and $C_c = 1.01125$. Figure 5.5 and Table 5.5 present the results for oblate spheroids, and Figure 5.6 and Table 5.6 for prolate spheroids. It is clear that all numerical solutions converge exponentially to the exact ones and a machine precision can be attained for all aspect ratios.

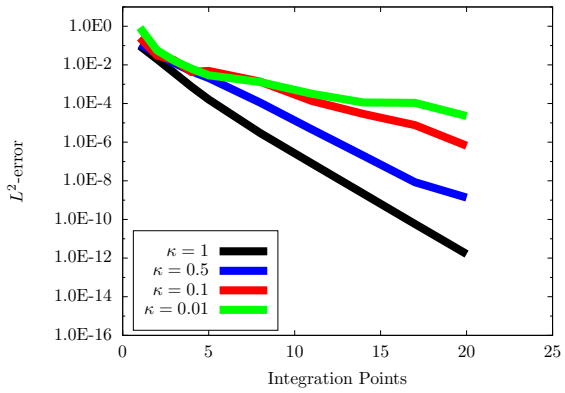

Figure 5.3: Neumann Patch Test for oblate spheroidal voids in an infinite body.

Int. Pts.	Aspect ratio			
	$\kappa = 1$	$\kappa = 0.5$	$\kappa = 0.1$	$\kappa = 0.01$
1	9.62E-02	1.18E-01	2.53E-01	8.51E-01
2	1.99E-02	3.79E-02	3.03E-02	5.67E-02
3	3.87E-03	1.24E-02	1.76E-02	1.66E-02
4	7.43E-04	4.66E-03	4.32E-03	6.39E-03
5	1.63E-04	2.10E-03	4.87E-03	2.91E-03
8	2.96E-06	1.12E-04	1.36E-03	1.30E-03
11	7.91E-08	4.59E-06	1.37E-04	3.20E-04
14	2.16E-09	1.99E-07	2.90E-05	1.14E-04
17	5.78E-11	8.46E-09	7.65E-06	1.08E-04
20	1.62E-12	1.35E-09	6.56E-07	2.27E-05

Table 5.3: Neumann Patch Test for oblate spheroidal voids in an infinite body.

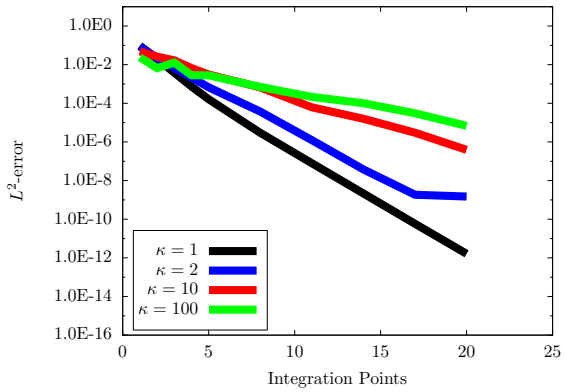

Figure 5.4: Neumann Patch Test for prolate spheroidal voids in an infinite body.

Int. Pts.	Aspect ratio			
	$\kappa = 1$	$\kappa = 0.5$	$\kappa = 0.1$	$\kappa = 0.01$
1	9.62E-02	8.66E-02	4.95E-02	2.38E-02
2	1.99E-02	2.21E-02	2.59E-02	6.59E-03
3	3.87E-03	6.77E-03	1.69E-02	1.28E-02
4	7.43E-04	2.17E-03	6.65E-03	2.84E-03
5	1.63E-04	6.73E-04	3.10E-03	2.79E-03
8	2.96E-06	3.74E-05	6.65E-04	7.10E-04
11	7.91E-08	1.24E-06	6.22E-05	2.15E-04
14	2.16E-09	3.76E-08	1.58E-05	1.01E-04
17	5.78E-11	1.85E-09	3.01E-06	3.06E-05
20	1.62E-12	1.49E-09	3.90E-07	6.87E-06

Table 5.4: Neumann Patch Test for prolate spheroidal voids in an infinite body.

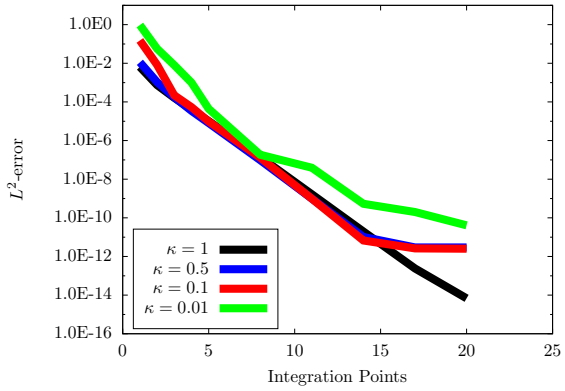

Figure 5.5: Neumann Patch Test for oblate spheroidal voids in an infinite body.

Int. Pts.	Aspect ratio			
	$\kappa = 1$	$\kappa = 0.5$	$\kappa = 0.1$	$\kappa = 0.01$
1	6.49E-03	1.13E-02	1.53E-01	9.60E-01
2	7.49E-04	1.07E-03	8.37E-03	5.72E-02
3	1.64E-04	1.77E-04	2.21E-04	8.05E-03
4	4.01E-05	3.46E-05	5.36E-05	9.97E-04
5	1.02E-05	8.09E-06	9.73E-06	4.38E-05
8	1.40E-07	9.72E-08	1.30E-07	1.85E-07
11	1.66E-09	9.89E-10	9.80E-10	3.94E-08
14	1.95E-11	1.03E-11	6.70E-12	5.34E-10
17	2.38E-13	2.95E-12	2.62E-12	2.01E-10
20	6.84E-15	2.93E-12	2.52E-12	4.11E-11

Table 5.5: Neumann Patch Test for oblate spheroidal voids in an infinite body.

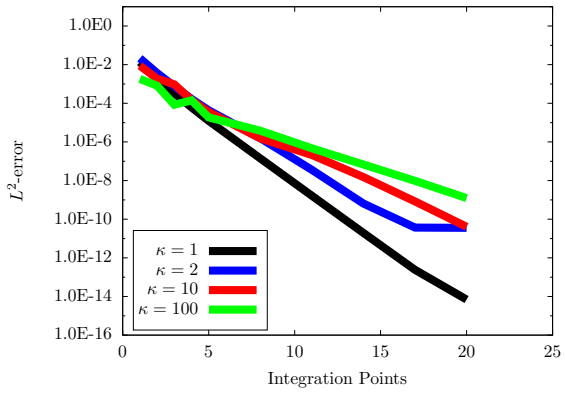

Figure 5.6: Neumann Patch Test for prolate spheroidal voids in an infinite body.

Int. Pts.	Aspect ratio			
	$\kappa = 1$	$\kappa = 0.5$	$\kappa = 0.1$	$\kappa = 0.01$
1	1.35E-02	2.15E-02	8.84E-03	1.83E-03
2	1.77E-03	3.68E-03	1.90E-03	8.16E-04
3	3.35E-04	7.62E-04	9.60E-04	8.40E-05
4	6.17E-05	1.69E-04	1.48E-04	1.42E-04
5	1.23E-05	4.34E-05	3.62E-05	1.87E-05
8	1.41E-07	1.57E-06	1.53E-06	3.81E-06
11	1.65E-09	3.61E-08	2.11E-07	4.68E-07
14	1.95E-11	6.48E-10	1.51E-08	6.76E-08
17	2.38E-13	3.67E-11	8.33E-10	9.65E-09
20	6.95E-15	3.57E-11	4.04E-11	1.24E-09

Table 5.6: Neumann Patch Test for prolate spheroidal voids in an infinite body.

Chapter 6

An industrial example

6.1 Introduction

In this chapter, we use IBEMs to analyze a propeller. In doing this, we demonstrate the compatibility of IBEMs with CAD software packages and applicability of IBEMs to industrial problems. In the process, we demonstrate the usefulness of Patch Tests to assessing the quality of IBEM approximations and integration rules.

6.2 Compatibility with CAD Tools

A key feature IBEMs is their reliance on CAD generated geometries. Those can be produced using various commercially available software packages, most of which rely on NURBS rather than T-splines. In this regard, we chose Rhinoceros ^{TM}(Rhino) package, developed by Robert McNeel & Associates, because it can be combined with the T-Splines ^{TM}plug-in developed by Autodesk ^{TM}. Using the plug-in, one can convert a NURBS-based CAD description into a T-spline description or develop a T-spline description from scratch. The former version was used for the canonical shapes, while the latter option was used for the problem in this chapter [95].

As far as IBEMs are concerned, one needs to develop two additional geometric inputs necessary for specifying (i) boundary conditions and (ii) discontinuous basis functions. The boundary conditions are specified using the selection sets option, which allows one to identify sets of faces comprising Dirichlet and Neumann boundaries. The discontinuous basis functions are specified according to the following procedure:

1. Mark Bézier edges where discontinuous basis functions are required. Those include the interface between the Dirichlet and Neumann boundaries, (geometric as opposed to Bézier) edges, and corners.

2. "Crease" the marked Bézier edges. This command generates the discontinuous basis functions and two-ring collocation points.[1]

3. Mark all collapsed edges, and replace the corresponding default collocation points with those required for collocating near collapsed edges; see Chapter 2.

All data involved in this task is written using the .iga file format [96]. If these three steps were implemented in the T-Splines plug-in, that would result in fully automated IBEM analysis.

[1] At this stage the crease command is not fully automated for IBEMs applications, but it is straightforward to tweak manually.

6.3 A propeller under a wind load

6.3.1 Problem and CAD description

As an example problem, we analyzed a propeller subjected to a wind load. The propeller was specified using a CAD file generated using Rhino's T-splines plug-in [95]. The CAD representation involved 5136 Bézier elements and 48 extraordinary points (Figs. 6.1 and 6.2).

To simulate a wind load, we assigned zero displacements on the interior cylindrical surface of the hub, as shown in Figure 6.3. The remaining boundary was subjected to traction boundary conditions prescribed as

$$t = [0, 0, -Pn_3 H(n_3)] \ ,$$

where P is the wind pressure, n is the outward unit normal, H is Heavyside's function, and x_3 is the symmetry axis of the propeller. The propeller was made of an aluminum alloy with Young's modulus $E = 6.9 \times 10^{10} Pa$ and Poisson's ratio $\nu = 0.334$.

In addition to the steps described in the previous section, we creased all edges on the Dirichlet boundary (Fig. 6.4). The purpose of this modification was to eliminate collocation points on the edges of Bézier elements on the Dirichlet boundary. This is a temporary measure necessary for computing consistent tangent vectors. Ultimately, this measure can be replaced with a proper computation of tangent vectors on Bézier edges.

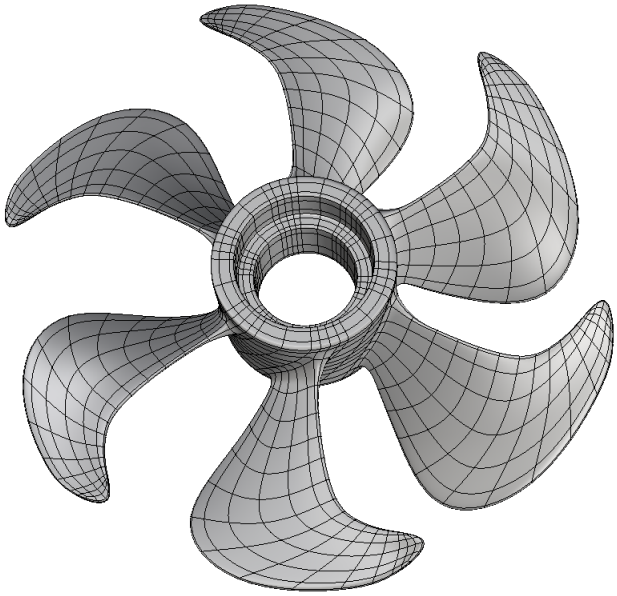

Figure 6.1: The CAD geometry of the propeller.

6.3.2 Patch Tests

Once the Dirichlet and Neumann boundaries, have been specified, it is useful to perform Patch Tests to assess approximation and integration errors Since the given problem is a mixed BVP, it is natural to consider a mixed BVP Patch Test associated with the original problem. Accordingly, we selected the problem of uniaxial compression along the x_3-axis, with the fields

$$\sigma_{ij} = -P\delta_{i3}\delta_{j3}$$

and

$$u = \left(\frac{\nu P x_1}{E}, \frac{\nu P x_2}{E}, -\frac{P x_3}{E} \right) .$$

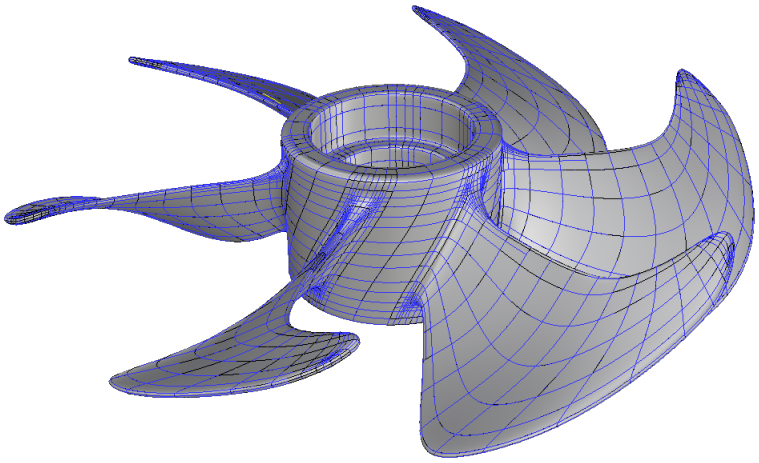

Figure 6.2: The Bézier mesh of the propeller.

These fields generate the corresponding Dirichlet and Neumann data. Note that the Dirichlet boundary is such that its normal is spanned by the basis functions, and therefore as established in Chapter 5, the posed Patch Test can be solved exactly, modulo numerical integration errors. Instead of establishing an exponential convergence rate with respect to the number of integration points, we simply solved the Patch Test problem using the basic integration scheme. The normalized L^2-error on Γ was considered for both the displacement and the traction field. The average normalized L^2-error of the displacements was close to 10^{-3} and the average normalized L^2-error of the tractions was 10^{-7}. We regarded these errors as acceptable and proceeded to the analysis of the main problem.

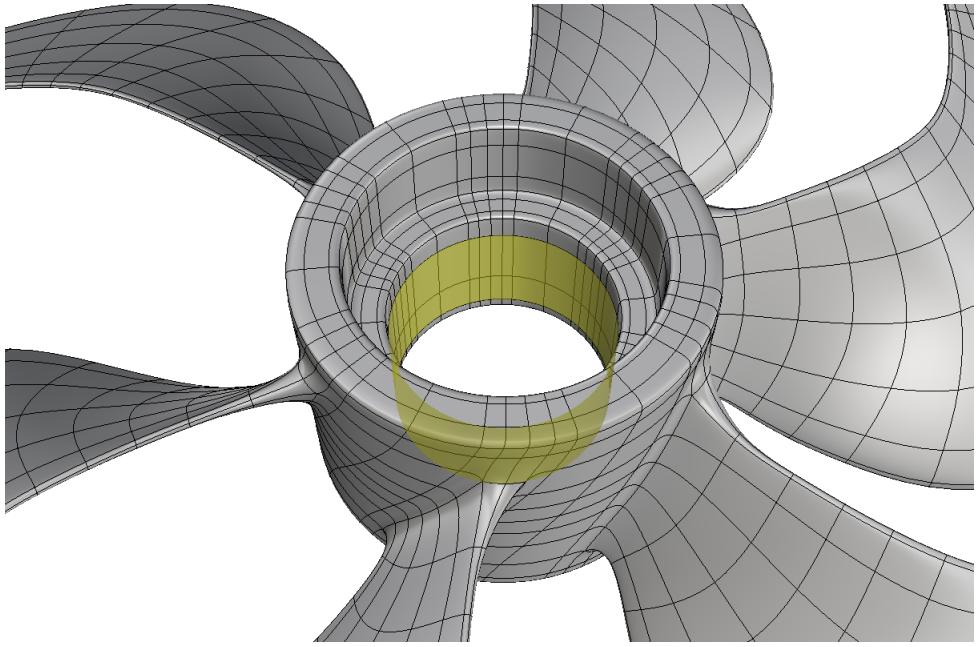

Figure 6.3: The Dirichlet boundary for the wind loading on the propeller.

6.3.3 Results

For simulation purposes, we selected $P = 1,500\,Pa$, which corresponds to the wind speed of about $55\,m/s$. Figure 6.5 shows the deformed shape of the propeller where the displacement field is exaggerated by a factor of 1000. The deformed propeller is colored using the magnitude of the displacement, and the Bézier mesh of the original geometry is superimposed. Note that the lack of smoothness of the Bézier mesh is due to post-processing only. Note that the solution exhibits appropriate symmetry.

Figure 6.6 shows the von Mises stress. Again, it is clear that the results are symmetric. Furthermore, each blade of the propeller resembles the behavior

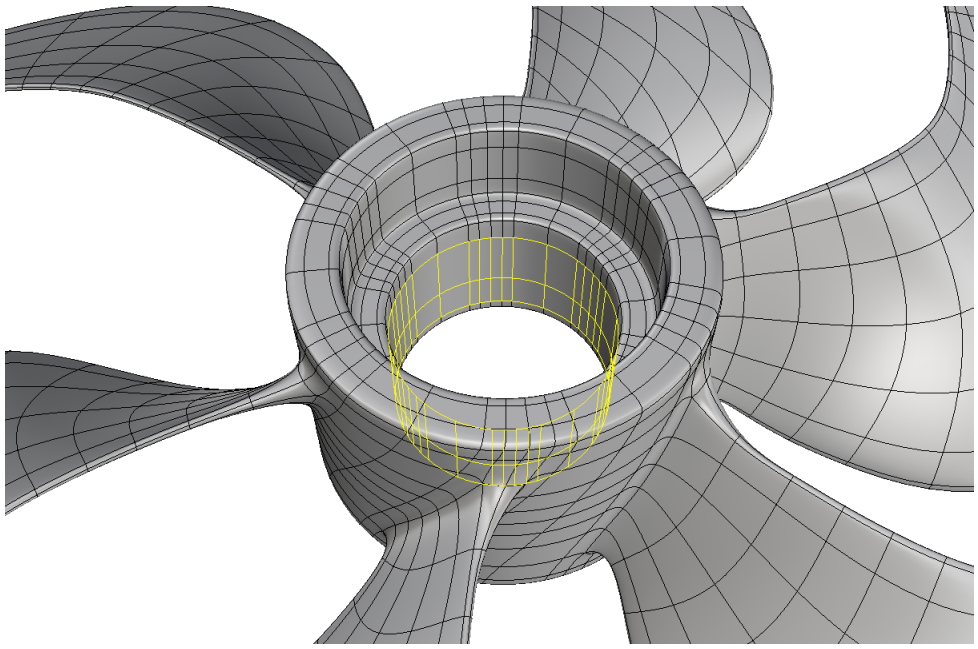

Figure 6.4: The creased edges to define discontinuous basis functions.

of a cantilever beam, as the maximum stress is near the hub.

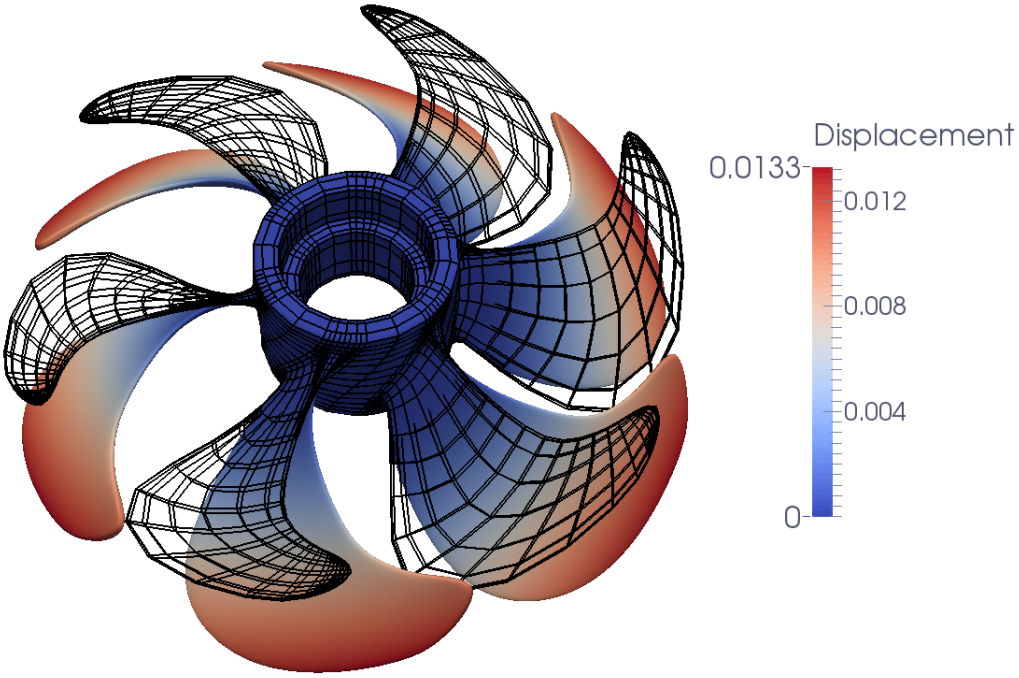

Figure 6.5: The deformed propeller exaggerated by a factor of 1000. The propeller is colored by the magnitude of the displacement and superimposed by the Bézier mesh of the original geometry.

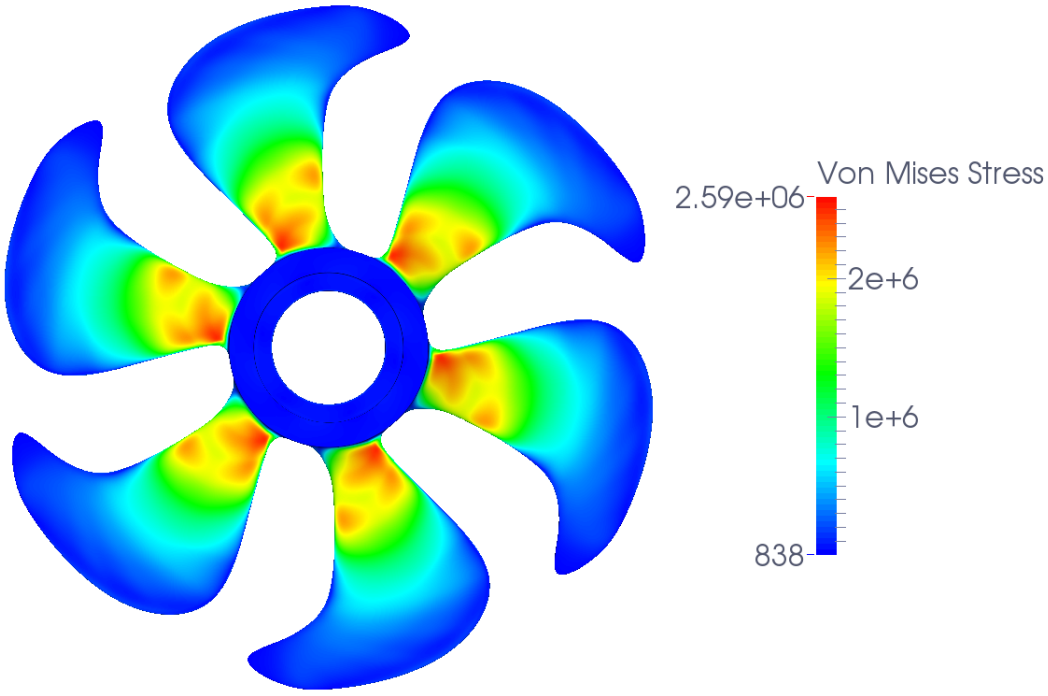

Figure 6.6: The Von Mises Stress on the propeller.

Chapter 7

Conclusion

In this dissertation, we adopted IgA as the foundation for solving BIEs. Accordingly, we focused on problems defined on $\tilde{C}^2$-surfaces, which are common in IgA. Our theoretical results and numerical schemes take full advantage of this geometric smoothness. In this regard, our work is a major departure from previous research concerned with applying IgA to BIEs, where IgA was considered merely as a BEM with different basis functions.

Numerical schemes developed in this dissertation allow one to apply collocation schemes to both SBIE and HSBIE; ordinarily the HSBIE can be analyzed within Galerkin's setting only. The access to both SBIE and HSBIE was exploited for constructing governing linear algebraic equations with optimal spectral properties. Furthermore, all integral operators involved in the SBIE and HSBIE were reduced to weakly-singular integrals, for which we adopted effective numerical integration schemes available in the literature, including the polar coordinates transformation, local reparametrization of the surface, and recursive subdivision. This combination resulted in an exponentially convergent integration scheme, essential for attaining optimal approximation properties.

Adopting IgA for numerical treatment of BIEs necessitated the introduction of the following numerical schemes:

- Discontinuous basis functions for treating edges and vertices of non-smooth domains, and irregularities associated with collapsed edges and extraordinary points, both common in IgA.
- Local reparametrization of surfaces necessary for effective and accurate integration schemes, especially in the vicinity of collapsed edges.
- Recursive subdivision of elements necessary for effective and accurate integration schemes, especially if for elements with high curvature and aspect ratio.
- Degree elevated basis functions advantageous for solving mixed boundary-value problems.

In addition, we developed Patch Tests in the context of BEMs. These tests not only allow one to assess the reliability of IBEM implementations but also show that IBEMs can be used to solve problems up to machine precision on very coarse meshes. Furthermore, our implementation of IBEMs is directly compatible with commercial CAD packages and does not rely on user-generated meshes.

We have applied our method to Laplace's equation and the equations of linear elasticity. Several numerical examples have been considered. These examples

show the necessity of the developments presented in this dissertation and confirm all theoretical findings. Further, we have subjected our implementation to the developed Patch Tests which not only confirmed the reliability of our method but also showed its robustness with respect to geometries with high local curvature. Finally, we applied our method to analyze a propeller under a wind load. In this problem a CAD geometry was used to provide a solution for an industrial problem with high confidence.

While this dissertation sets a rigorous base for the development of IBEMs, there are several open issues, whose resolution may significantly advance IgA of BIEs. Among them are:

- Mathematical foundations for collocation schemes for BIEs corresponding to pure BVPs defined on non-smooth domains.
- Mathematical foundations for collocation schemes for BIEs corresponding to mixed BVPs defined on smooth and ultimately non-smooth domains.
- Efficient integration schemes for Galerkin discretizations.
- Better numerical integration schemes that exploit smoothness of the basis functions.
- Adaptive numerical integration and approximation schemes, in the spirit of $h-p-k$ methods, introduced and described herein [35, 36].

Further, we would like to mention that in this dissertation we did not present results on fast IBEMs. We were able to merge our implementation with a fast multipole method developed by Greengard and Gimbutas [47]. This approach was proved to be reliable for canonical geometries such as tori, spheres or cubes but for more complicated geometries the conditioning of the system matrices prevented an efficient use of the fast multipole method. To this end, preconditioning techniques, e.g. domain decomposition methods, seem to be a fruitful direction of future research to further improve on the applicability and efficiency of IBEMs, especially in the context of fast multipole methods. In conclusion, let us mention that most of the theoretical results and computational numerical schemes of this dissertation can also be extended to other applications, e.g. the Stokes equations of fluid mechanics. Those extensions may have a significant impact on the development of tools for engineering design and analysis.

Appendices

Appendix A

Compactness of integral operators

In this section we prove that the double-layer operators $\mathcal{K}$ and $\mathcal{K}'$ defined on $\Gamma \in C^2$ are compact operators on the space of continuous functions.

Consider a bounded domain $\Omega \subset \mathbb{R}^3$ with $\Gamma := \partial\Omega$. By definition $\Gamma \in C^2$ if it satisfies the following conditions:

1. For any $x \in \Gamma$ there exists a constant $R > 0$, independent of x, and a neighborhood $N_x \subset \mathbb{R}^3$ such that $\text{dist}(x, \Gamma \backslash N_x) > R$;

2. The surface $\Gamma_x := \Gamma \cap N_x$ is an image of a domain $\hat{N}_x \subset \mathbb{R}^2$ under the map ψ_x;

3. The map ψ_x is bijective and twice continuously differentiable;

4. The maps ψ_x and ψ_x^{-1} are Lipschitz continuous.

Theorem A.0.1. *If $\Gamma \in C^2$ then there exists a constant $C > 0$ such that*

$$\left| \frac{(x-y) \cdot n(y)}{4\pi |x-y|^3} \right| \leq \frac{C}{|x-y|}$$

for all $x, y \in \Gamma$.

Proof. Let $x \in \Gamma$. If $y \notin \Gamma_x$, then there exists a constant $R > 0$ such that $\operatorname{dist}(x, \Gamma \backslash \Gamma_x) > R$ and consequently $|y - x| > R$. As a result we obtain the estimate

$$\left| \frac{(x-y) \cdot n(y)}{4\pi |x-y|^3} \right| \leq \frac{\operatorname{diam}(\Omega)}{4\pi R^3} \leq \frac{\operatorname{diam}(\Omega)^2}{4\pi R^3} \frac{1}{|x-y|} \, .$$

If $y \in \Gamma_x$ then there exist $\hat{x} \in \hat{N}_x$ and $\hat{y} \in \hat{N}_x$ such that $\psi_x(\hat{x}) = x$ and $\psi_x(\hat{y}) = y$ because ψ_x is bijective. Since ψ_x is twice continuously differentiable, we can use the following expressions for the normal

$$n(y) = \frac{\frac{\partial \psi_x(\hat{y})}{\partial \hat{y}_1} \times \frac{\partial \psi_x(\hat{y})}{\partial \hat{y}_2}}{\left| \frac{\partial \psi_x(\hat{y})}{\partial \hat{y}_1} \times \frac{\partial \psi_x(\hat{y})}{\partial \hat{y}_2} \right|}$$

and Taylor's expansion

$$x - y = \psi_x(\hat{x}) - \psi_x(\hat{y}) = \frac{\partial \psi_x(\hat{y})}{\partial \hat{y}_1}(\hat{x}_1 - \hat{y}_1) + \frac{\partial \psi_x(\hat{y})}{\partial \hat{y}_2}(\hat{x}_2 - \hat{y}_2) + \mathcal{O}(|\hat{x} - \hat{y}|^2)$$

to obtain the estimate

$$(x-y) \cdot n(y) = \mathcal{O}(|\hat{x} - \hat{y}|^2).$$

Since ψ_x^{-1} is Lipschitz continuous, there exists a constant $l > 0$ such that $l|\hat{x} - \hat{y}| \leq |\psi_x(\hat{x}) - \psi_x(\hat{y})| = |x - y|$, which implies

$$\left| \frac{(x-y) \cdot n(y)}{4\pi |x-y|^3} \right| = \mathcal{O}\left(\frac{1}{|x-y|} \right).$$

□

This theorem implies that the operator $\mathcal{K}$ is weakly singular. Similarly, we can establish the bound

$$\left| \frac{(x-y) \cdot n(x)}{4\pi |x-y|^3} \right| \leq \frac{C}{|x-y|} \quad \forall x, y \in \Gamma \, ,$$

and thus establish that the operator $\mathcal{K}'$ is also weakly singular.

Using well-established techniques, it can be proved that the operators $\mathcal{K}, \mathcal{K}' : C(\Gamma) \to C(\Gamma)$ are compact and the operators $\frac{1}{2}I + \mathcal{K}$ and $\frac{1}{2}I - \mathcal{K}'$ are invertible [46, Chapter 3]. Furthermore, if we assume that there exists a bounded interpolation operator that maps continuous functions onto continuous basis functions (2.2), one can invoke compact perturbations theory to prove that the discrete problems (3.13) and (3.15) are uniquely solvable and their solutions $\tilde{u}_h$ and $\tilde{t}_h$ satisfy quasi-optimal error estimates in the $L^\infty(\Gamma)$-norm [71, Chapter XII.1].

Appendix B

Numerical evaluation of weakly singular integrals

In Section 3.4 we have determined that the evaluation of all boundary integral operators requires the evaluation of weakly singular integrals over parallelograms

$$\int_{\tilde{e}} \frac{f(\tilde{\varphi}(\xi_1, \xi_2))}{|\tilde{\varphi}(\hat{t}) - \tilde{\varphi}(\xi_1, \xi_2)|} d\xi_1 d\xi_2 \, .$$

Here, $\tilde{e}$ is a parallelogram and f is a smooth function. In what follows, we provide details for the technique using polar coordinate transformations to regularize integrals of this form.

Using polar coordinates, the integral can be written as

$$\int_{\tilde{e}} \frac{f(\tilde{\varphi}(\xi_1, \xi_2))}{|\tilde{\varphi}(\hat{t}) - \tilde{\varphi}(\xi_1, \xi_2)|} d\xi_1 d\xi_2 = \int_0^{2\pi} \int_0^{R(\theta)} \frac{\rho f(\tilde{\varphi}(\rho\cos\theta, \rho\sin\theta))}{|\tilde{\varphi}(\hat{t}) - \tilde{\varphi}(\rho\cos\theta, \rho\sin\theta)|} d\rho d\theta.$$

As described in Section 3.4, results in [91] can be used to show that the integrand on the right-hand side is analytic in ρ and θ. However, the bound $R(\theta)$ for the variable ρ is not analytic in the vicinity of the vertices of the parallelogram. Therefore, it is customary to subdivide the parallelogram into triangles

by connecting the collocation point with all vertices of the parallelogram as shown in Figure B.1. Then the integral can be evaluated as

$$\int_{\tilde{e}} \frac{f(\tilde{\varphi}(\xi_1,\xi_2))}{|\tilde{\varphi}(\hat{t})-\tilde{\varphi}(\xi_1,\xi_2)|} d\xi_1 d\xi_2 = \sum_{i=1}^{M} \int_{\theta_i}^{\theta_{i+1}} \int_0^{R_i(\theta)} \frac{\rho f(\tilde{\varphi}(\rho\cos\theta,\rho\sin\theta))}{|\tilde{\varphi}(\hat{t})-\tilde{\varphi}(\rho\cos\theta,\rho\sin\theta)|} d\rho d\theta.$$

where

$$R_i(\theta) = \frac{R_i(\theta_i)\sin\alpha_i}{\sin(\pi-\alpha_i-(\theta-\theta_i))}$$

and, depending on the position of the collocation point $\hat{t}$, $M = 2, 3, 4$.

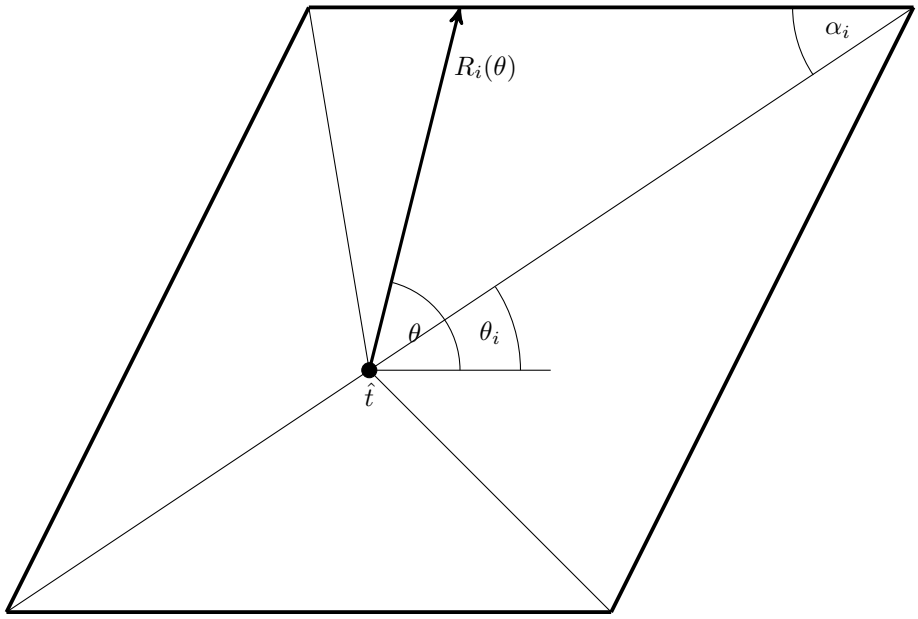

Figure B.1: The definition of the triangles used to define polar coordinate transformations centered at $\hat{t}$.

While this approach results in analytic integrals, the bound $R_i(\theta)$ becomes less smooth as the point $\hat{t}$ approaches an edge of the parallelogram. In this case

$\alpha_1 \approx 0$ and $\theta_2 - \theta_1 \approx \pi$ and consequently $R_i(\theta)$ is not bounded if θ is close to θ_2. To overcome this issue we use the additional transformation [52]

$$\theta(\tilde{\theta}) = \theta_i + \pi - \alpha_i - 2\tan^{-1}\left(e^{\tilde{\theta}}\right)$$

with

$$R_i(\theta) = \frac{R_i(\theta_i)\sin\alpha_i}{\sin(\pi - \alpha_i - (\theta - \theta_i))} = R_i(\theta_i)\sin\alpha_i\cosh\tilde{\theta}.$$

Note that in this representation of $R_i(\theta)$ it is easy to see that, independently of the location of the collocation point $\hat{t}$, $R(\theta(\tilde{\theta}))$ is a smooth function in $\tilde{\theta}$ and therefore the integral can be efficiently evaluated using Gaussian quadratures for the variables ρ and $\tilde{\theta}$.

The number of integration points needed for the accurate evaluation of the integral in the polar coordinates ρ and θ has been estimated in [92]. It has been shown that in order to preserve the optimal convergence rates with mesh refinement, the number of integration points used for ρ can be constant with respect to the mesh size h, whereas the number of integration points for θ have to be increased logarithmically with h. Assuming that the additional transformation $\tilde{\theta}(\theta)$ only improves the convergence of the numerical integration scheme, we use the same estimates to determine the number of Gaussian integration points for ρ and $\tilde{\theta}$ in order to preserve the optimal convergence rates. Accordingly, we use

$$n_\rho \geq p + 2, \quad \text{and} \quad n_{\tilde{\theta}} \geq (p+2)\frac{\log h}{\log 4.62}$$

Gaussian integration points for the variables ρ and $\tilde{\theta}$ respectively. Note that these estimates were determined in [92] under the assumption that the vectors $\frac{\partial\varphi(\xi_1,\xi_2)}{\partial\xi_1}$ and $\frac{\partial\varphi(\xi_1,\xi_2)}{\partial\xi_2}$ are orthonormal. If the collocation point is away from a collapsed edge, our integration scheme is such that this assumption is satisfied. If the collocation point is on a collapsed edge, following Section 3.4 and the proof of Theorem 2 in [92], it can be seen that the same choice is sufficient to preserve optimal error estimates. All numerical examples presented in this dissertation confirm that this choice of integration points is sufficient for a robust and accurate evaluation of weakly singular integrals.

Bibliography

[1] I. Akkerman, Y. Bazilevs, V. M. Calo, T. J. R. Hughes, and S. Hulshoff. The role of continuity in residual-based variational multiscale modeling of turbulence. *Computational Mechanics*, 41(3):371–378, 2008.

[2] D.N. Arnold and W.L. Wendland. On the asymptotic convergence of collocation methods. *Mathematics of Computation*, 41(164):349–381, 1983.

[3] K. E. Atkinson and I. G. Graham. Iterative solution of linear systems arising from the boundary integral method. *SIAM journal on scientific and statistical computing*, 13(3):694–722, 1992.

[4] K.E. Atkinson. *The numerical solution of integral equations of the second kind*. Cambridge university press, 1997.

[5] F. Auricchio, L. Beirão da Veiga, A. Buffa, C. Lovadina, A. Reali, and G. Sangalli. A fully locking-free isogeometric approach for plane linear elasticity problems: A stream function formulation. *Computer Methods in Applied Mechanics and Engineering*, 197(14):160 – 172, 2007.

[6] F. Auricchio, L. Beirão Da Veiga, T. J. R. Hughes, A. Reali, and G. Sangalli. Isogeometric collocation methods. *Mathematical Models and Methods in Applied Sciences*, 20(11):2075–2107, 2010.

[7] F. Auricchio, L. Beirão da Veiga, C. Lovadina, and A. Reali. The importance of the exact satisfaction of the incompressibility constraint in nonlinear elasticity: mixed FEMs versus NURBS-based approximations. *Computer Methods in Applied Mechanics and Engineering*, 199(58):314 – 323, 2010.

[8] F. Auricchio, L. Beiro da Veiga, T.J.R. Hughes, A. Reali, and G. Sangalli. Isogeometric collocation for elastostatics and explicit dynamics. *Computer Methods in Applied Mechanics and Engineering*, 249252(0):2 – 14, 2012.

[9] Y. Bazilevs and I. Akkerman. Large eddy simulation of turbulent Taylor-Couette flow using isogeometric analysis and the residual-based variational multiscale method. *Journal of Computational Physics*, 229(9):3402 – 3414, 2010.

[10] Y. Bazilevs, V. M. Calo, J. A. Cottrell, T. J. R. Hughes, A. Reali, and G. Scovazzi. Variational multiscale residual-based turbulence modeling for large eddy simulation of incompressible flows. *Computer Methods in Applied Mechanics and Engineering*, 197(14):173 – 201, 2007.

[11] Y. Bazilevs, V. M. Calo, T. J. R. Hughes, and Y. Zhang. Isogeometric fluid-structure interaction: theory, algorithms, and computations. *Computational Mechanics*, 43(1):3–37, 2008.

[12] Y. Bazilevs, V. M. Calo, Y. Zhang, and T. J. R. Hughes. Isogeometric

Fluid-structure Interaction Analysis with Applications to Arterial Blood Flow. *Computational Mechanics*, 38(4-5):310–322, 2006.

[13] Y. Bazilevs, J. R. Gohean, T. J. R. Hughes, R. D. Moser, and Y. Zhang. Patient-specific isogeometric fluid-structure interaction analysis of thoracic aortic blood flow due to implantation of the Jarvik 2000 left ventricular assist device. *Computer Methods in Applied Mechanics and Engineering*, 198(4546):3534 – 3550, 2009.

[14] Y. Bazilevs, C. Michler, V. M. Calo, and T. J. R. Hughes. Isogeometric variational multiscale modeling of wall-bounded turbulent flows with weakly enforced boundary conditions on unstretched meshes. *Computer Methods in Applied Mechanics and Engineering*, 199(1316):780 – 790, 2010.

[15] K. Belibassakis, T. Gerostathis, K. Kostas, C. Politis, P. Kaklis, A. Ginnis, and C. Feurer. A bem-isogeometric method with application to the wavemaking resistance problem of ships at constant speed. In *30th International Conference on Offshore Mechanics and Arctic Engineering, OMAE2011, Rotterdam, The Netherlands*, pages 95–102, 2011.

[16] K. A. Belibassakis, T. P. Gerostathis, K. V. Kostas, C. G. Politis, P. D. Kaklis, A. I. Ginnis, and C. Feurer. A BEM-isogeometric method for the ship wave-resistance problem. *Ocean Engineering*, 60(0):53 – 67, 2013.

[17] D. J. Benson, Y. Bazilevs, M.-C. Hsu, and T. J. R. Hughes. Isogeometric shell analysis: The ReissnerMindlin shell. *Computer Methods in Applied Mechanics and Engineering*, 199(58):276 – 289, 2010.

[18] D. J. Benson, Y. Bazilevs, M.-C. Hsu, and T. J. R. Hughes. A large deformation, rotation-free, isogeometric shell. *Computer Methods in Applied Mechanics and Engineering*, 200(1316):1367 – 1378, 2011.

[19] M. J. Borden, C. V. Verhoosel, M. A. Scott, T. J. R. Hughes, and C. M. Landis. A phase-field description of dynamic brittle fracture. *Computer Methods in Applied Mechanics and Engineering*, 217220(0):77 – 95, 2012.

[20] J. Bremer. On the Nyström discretization of integral equations on planar curves with corners. *Appl. Comput. Harmon. Anal.*, 32(1):45–64, 2012.

[21] J. Bremer and Z. Gimbutas. A Nyström method for weakly singular integral operators on surfaces. *J. Comput. Phys.*, 231(14):4885–4903, 2012.

[22] J. Bremer and V. Rokhlin. Efficient discretization of Laplace boundary integral equations on polygonal domains. *J. Comput. Phys.*, 229(7):2507–2525, 2010.

[23] J. Bremer, V. Rokhlin, and I. Sammis. Universal quadratures for boundary integral equations on two-dimensional domains with corners. *J. Comput. Phys.*, 229(22):8259–8280, 2010.

[24] O. P. Bruno, Y. Han, and M. M. Pohlman. Accurate, high-order representation of complex three-dimensional surfaces via fourier continuation analysis. *Journal of Computational Physics*, 227(2):1094–1125, 2007.

[25] O. P. Bruno, J. S. Ovall, and C. Turc. A high-order integral algorithm for highly singular PDE solutions in Lipschitz domains. *Computing*, 84(3-4):149–181, 2009.

[26] O.P. Bruno and L.A. Kunyansky. A fast, high-order algorithm for the solution of surface scattering problems: basic implementation, tests, and applications. *Journal of Computational Physics*, 169(1):80–110, 2001.

[27] O.P. Bruno and S.K. Lintner. A high-order integral solver for scalar problems of diffraction by screens and apertures in three-dimensional space. *Journal of Computational Physics*, 252:250–274, 2013.

[28] A. Buffa, G. Sangalli, and R. Vázquez. Isogeometric analysis in electromagnetics: B-splines approximation. *Computer Methods in Applied Mechanics and Engineering*, 199(1720):1143 – 1152, 2010.

[29] E. Catmull and J. Clark. Recursively generated b-spline surfaces on arbitrary topological meshes. *Computer-aided design*, 10(6):350–355, 1978.

[30] F. Cirak, M. Ortiz, and P. Schroder. Subdivision surfaces: a new paradigm for thin-shell finite-element analysis. *International Journal for Numerical Methods in Engineering*, 47(12):2039–2072, 2000.

[31] F. Cirak, M. J. Scott, E. K. Antonsson, M. Ortiz, and P. Schröder. Integrated modeling, finite-element analysis, and engineering design for thin-shell structures using subdivision. *Computer-Aided Design*, 34(2):137–148, 2002.

[32] M. Costabel. Boundary integral operators on Lipschitz domains: elementary results. *SIAM J. Math. Anal.*, 19(3):613–626, 1988.

[33] M. Costabel and W. McLean. Spline collocation for strongly elliptic equations on the torus. *Numerische Mathematik*, 62(1):511–538, 1992.

[34] M. Costabel and E.P. Stephan. On the convergence of collocation methods for boundary integral equations on polygons. *Mathematics of Computation*, 49(180):461–478, 1987.

[35] J. A. Cottrell, T. J. R. Hughes, and Y. Bazilevs. *Isogeometric analysis: Toward Integration of CAD and FEA*. Wiley, Chichester, 2009.

[36] J. A. Cottrell, T. J. R. Hughes, and A. Reali. Studies of refinement and continuity in isogeometric structural analysis. *Computer Methods in Applied Mechanics and Engineering*, 196(4144):4160 – 4183, 2007.

[37] J. A. Cottrell, A. Reali, Y. Bazilevs, and T. J. R. Hughes. Isogeometric analysis of structural vibrations. *Computer Methods in Applied Mechanics and Engineering*, 195(4143):5257 – 5296, 2006.

[38] T.A. Cruse. Numerical solutions in three dimensional elastostatics. *International Journal of Solids and Structures*, 5(12):1259 – 1274, 1969.

[39] D. J. Benson and Y. Bazilevs and E. De Luycker and M.-C. Hsu and M. Scott and T. J. R. Hughes and T. Belytschko. A generalized finite element formulation for arbitrary basis functions: From isogeometric analysis to xfem. *International Journal for Numerical Methods in Engineering*, 83(6):765–785, 2010.

[40] C. De Boor. On bounding spline interpolation. *Journal of Approximation Theory*, 14(3):191–203, 1975.

[41] Stephen Demko. On the existence of interpolating projections onto spline spaces. *Journal of Approximation Theory*, 43(2):151 – 156, 1985.

[42] R. Echter and M. Bischoff. Numerical efficiency, locking and unlocking of NURBS finite elements. *Computer Methods in Applied Mechanics and Engineering*, 199(58):374 – 382, 2010.

[43] T. Elguedj, Y. Bazilevs, V. M. Calo, and T. J. R. Hughes. $\bar{\mathrm{B}}$ and $\bar{\mathrm{F}}$ projection methods for nearly incompressible linear and non-linear elasticity and plasticity using higher-order NURBS elements. *Computer Methods in Applied Mechanics and Engineering*, 197(3340):2732 – 2762, 2008.

[44] J. D. Eshelby. The determination of the elastic field of an ellipsoidal inclusion, and related problems. *Proceedings of the Royal Society of London A: Mathematical, Physical and Engineering Sciences*, 241(1226):376–396, 1957.

[45] J.D. Eshelby. The elastic field outside an ellipsoidal inclusion. *Proceedings of the Royal Society of London. Series A, Mathematical and Physical Sciences*, 252(1271):pp. 561–569, 1959.

[46] G. Folland. *Introduction to partial differential equations*. Princeton University Press, 1995.

[47] Z. Gimbutas and L. Greengard. Fmmlib3d/stfmmlib3d. `http://www.cims.nyu.edu/cmcl/fmm3dlib/fmm3dlib.html`. Accessed: 2015-06-18.

[48] A. I. Ginnis, C. Feurer, K. A. Belibassakis, P. D Kaklis, K. V. Kostas, T. P. Gerostathis, and C. G. Politis. A Catia ship-parametric model for isogeometric hull optimization with respect to wave resistance. In *ICCAS 2011*. Royal Institution of Naval Architects, 2011.

[49] H. Gómez, V. M. Calo, Y. Bazilevs, and T. J. R. Hughes. Isogeometric analysis of the Cahn-Hilliard phase-field model . *Computer Methods in Applied Mechanics and Engineering*, 197(4950):4333 – 4352, 2008.

[50] H. Gómez, T. J. R. Hughes, X. Nogueira, and V. M. Calo. Isogeometric analysis of the isothermal Navier-Stokes-Korteweg equations. *Computer Methods in Applied Mechanics and Engineering*, 199(2528):1828 – 1840, 2010.

[51] L. Greengard and V. Rokhlin. A fast algorithm for particle simulations. *Journal of Computational Physics*, 73(2):325–348, 1987.

[52] J.-L. Guermond. Numerical quadratures for layer potentials over curved domains in r^3. *SIAM Journal on Numerical Analysis*, 29(5):1347–1369, 1992.

[53] W. Hackbusch. *Integral Equations: Theory and Numerical Treatment*. International Series of Numerical Mathematics. Birkhäuser Basel, 2012.

[54] J. Helsing and R. Ojala. Corner singularities for elliptic problems: integral equations, graded meshes, quadrature, and compressed inverse preconditioning. *J. Comput. Phys.*, 227(20):8820–8840, 2008.

[55] G. G. C. Hsiao and W. W. L. Wendland. *Boundary Integral Equations*. Applied Mathematical Sciences Series. Springer-Verlag Berlin Heidelberg, 2008.

[56] G.C. Hsiao and S. Prössdorf. A generalization of the arnold-wendland lemma to a modified collocation method for boundary integral equations in r3. *Mathematische Nachrichten*, 163(1):133–144, 1993.

[57] T. J. R. Hughes, J. A. Cottrell, and Y. Bazilevs. Isogeometric analysis: CAD, finite elements, NURBS, exact geometry and mesh refinement. *Computer Methods in Applied Mechanics and Engineering*, 194(3941):4135 – 4195, 2005.

[58] H. Ipson. T-spline Merging. Master's thesis, Brigham Young University, 2005.

[59] M. A. Jaswon. Integral equation methods in potential theory. i. *Proceedings of the Royal Society of London A: Mathematical, Physical and Engineering Sciences*, 275(1360):23–32, 1963.

[60] Rong-Qing Jia. Spline interpolation at knot averages. *Constructive Approximation*, 4(1):1–7, 1988.

[61] K. H. Muci-Küchler and T. J. Rudolphi. A weakly singular formulation of traction and tangent derivative boundary integral equations in three dimensional elasticity. *Engineering Analysis with Boundary Elements*, 11(3):195 – 201, 1993.

[62] J. Kiendl, Y. Bazilevs, M.-C. Hsu, R. Wüchner, and K.-U. Bletzinger. The bending strip method for isogeometric analysis of Kirchhoff-Love shell structures comprised of multiple patches. *Computer Methods in Applied Mechanics and Engineering*, 199(3740):2403 – 2416, 2010.

[63] A. Klöckner, A. Barnett, L. Greengard, and M. O'Neil. Quadrature by expansion: a new method for the evaluation of layer potentials. *Journal of Computational Physics*, 252:332–349, 2013.

[64] R. Kress. *Linear Integral Equations*. Springer My Copy UK, 1989.

[65] R. Kress. A Nyström method for boundary integral equations in domains with corners. *Numer. Math.*, 58(2):145–161, 1990.

[66] V.D Kupradze. *Potential methods in the theory of elasticity*. Israel program for scientific translations, 1965.

[67] Kang L. and Xiaoping Q. Isogeometric analysis and shape optimization via boundary integral. *Computer Aided Design*, 43(11):1427–1437, 2011.

[68] S. Lipton, J. A. Evans, Y. Bazilevs, T. Elguedj, and T. J. R. Hughes. Robustness of isogeometric structural discretizations under severe mesh distortion. *Computer Methods in Applied Mechanics and Engineering*, 199(58):357 – 373, 2010.

[69] William Charles Hector McLean. *Strongly elliptic systems and boundary integral equations*. Cambridge university press, 2000.

[70] S.G. Mikhlin. Integral equations. 1957.

[71] S.G. Mikhlin and S. Prößdorf. *Singular Integral Operators*. 2. Springer Berlin Heidelberg, 1987.

[72] A. P. Nagy, M. M. Abdalla, and Z. Gürdal. Isogeometric sizing and shape optimisation of beam structures . *Computer Methods in Applied Mechanics and Engineering*, 199(1720):1216 – 1230, 2010.

[73] A. P. Nagy, M. M. Abdalla, and Z. Gürdal. On the variational formulation of stress constraints in isogeometric design . *Computer Methods in Applied Mechanics and Engineering*, 199(4144):2687 – 2696, 2010.

[74] N Nishimura. Fast multipole accelerated boundary integral equation methods. *Applied Mechanics Reviews*, 55(4):299–324, 2002.

[75] M. J. Peake, J. Trevelyan, and G. Coates. Extended isogeometric boundary element method (XIBEM) for two-dimensional Helmholtz problems. *Computer Methods in Applied Mechanics and Engineering*, 259(0):93 – 102, 2013.

[76] L. Piegl and W. Tiller. The nurbs book. 1997. *Monographs in Visual Communication*, 1997.

[77] C. Politis, A. I. Ginnis, P. D. Kaklis, K. Belibassakis, and C. Feurer. An isogeometric BEM for exterior potential-flow problems in the plane. In *2009 SIAM/ACM Joint Conference on Geometric and Physical Modeling*, pages 349–354. ACM, 2009.

[78] Xiaoping Q. Full analytical sensitivities in NURBS based isogeometric shape optimization. *Computer Methods in Applied Mechanics and Engineering*, 199(2932):2059 – 2071, 2010.

[79] B. Quaife and G. Biros. High-volume fraction simulations of two-dimensional vesicle suspensions. *Journal of Computational Physics*, 274:245–267, 2014.

[80] J. Ritter. Graphics gems. chapter An Efficient Bounding Sphere, pages 301–303. Academic Press Professional, Inc., 1990.

[81] F.J. Rizzo. An integral equation approach to boundary value problems of classical elastostatics. *Quarterly of Applied Mathematics*, 25(1):83–&, 1967.

[82] D. F. Rogers. *An introduction to NURBS: with historical perspective*. Elsevier, 2000.

[83] V. Rokhlin. Rapid solution of integral equations of classical potential theory. *J. Comput. Phys.*, 60(2):187–207, 1985.

[84] T. J. Rudolphi. The use of simple solutions in the regularization of hypersingular boundary integral equations. *Math. Comput. Modelling*, 15(3-5):269–278, 1991. Boundary integral equation methods (boundary element methods).

[85] Y. Saad and M. H. Schultz. GMRES: A Generalized Minimal Residual Algorithm for Solving Nonsymmetric Linear Systems. *SIAM J. Sci. Stat. Comput.*, 7(3):856–869, 1986.

[86] M. Sabin. Recent progress in subdivision: a survey. In *Advances in Multiresolution for Geometric Modelling*, pages 203–230. Springer, 2005.

[87] J. Saranen and W.L. Wendland. On the asymptotic convergence of collocation methods with spline functions of even degree. *Mathematics of Computation*, 45(171):91–108, 1985.

[88] S. A. Sauter and C. Schwab. Boundary Element Methods. In *Boundary Element Methods*, volume 39 of *Springer Series in Computational Mathematics*, pages 183–287. Springer Berlin Heidelberg, 2011.

[89] D. Schillinger, L. Dedè, M. A. Scott, J. A. Evans, M. J. Borden, E. Rank, and T. J. R. Hughes. An isogeometric design-through-analysis methodology based on adaptive hierarchical refinement of NURBS, immersed boundary methods, and T-spline CAD surfaces. *Computer Methods in Applied Mechanics and Engineering*, 249252(0):116 – 150, 2012.

[90] P. Schröder, D. Zorin, T. DeRose, D. R. Forsey, L. Kobbelt, M. Lounsbery, and J. Peters. Subdivision for modeling and animation. *ACM SIGGRAPH Course Notes*, 12, 1998.

[91] C. Schwab and W. L. Wendland. Kernel properties and representations of boundary integral operators. *Mathematische Nachrichten*, 156(1):187–218, 1992.

[92] C. Schwab and W. L. Wendland. On numerical cubatures of singular surface integrals in boundary element methods. *Numerische Mathematik*, 62(1):343–369, 1992.

[93] M. A. Scott. *T-splines as a Design-Through-Analysis Technology*. PhD thesis, The University of Texas at Austin, 2011.

[94] M. A. Scott, R. N. Simpson, J. A. Evans, S. Lipton, S. P. A. Bordas, T. J. R. Hughes, and T. W. Sederberg. Isogeometric boundary element analysis using unstructured T-splines. *Computer Methods in Applied Mechanics and Engineering*, 254(0):197 – 221, 2013.

[95] M.A. Scott. private communication.

[96] M.A. Scott, T.J.R. Hughes, T.W. Sederberg, and M.T. Sederberg. An integrated approach to engineering design and analysis using the autodesk t-spline plugin for rhino3d. *Advances in Engineering Software (in preparation)*, 2013.

[97] T. W. Sederberg, G. T. Finnigan, X. Li, H. Lin, and H. Ipson. Watertight trimmed nurbs. *ACM Transactions on Graphics (TOG)*, 27(3):79, 2008.

[98] T. W. Sederberg, J. Zheng, A. Bakenov, and A. Nasri. T-splines and T-NURCCs. *ACM Trans. Graph.*, 22(3):477–484, July 2003.

[99] T.W. Sederberg, J. Zheng, A. Bakenov, and A. Nasri. T-splines and t-nurccs. *ACM Trans. Graph.*, 22(3):477–484, 2003.

[100] R. N. Simpson, S. P. A. Bordas, J. Trevelyan, and T. Rabczuk. A two-dimensional isogeometric boundary element method for elastostatic analysis. *Computer Methods in Applied Mechanics and Engineering*, 209-212:87–100, 2012.

[101] R. N. Simpson, M.A. Scott, M. Taus, D.C. Thomas, and H. Lian. Acoustic isogeometric boundary element analysis. *Computer Methods in Applied Mechanics and Engineering*, 269(0):265 – 290, 2014.

[102] V. Sladek, J. Sladek, and M. Tanaka. Numerical integration of logarithmic and nearly logarithmic singularity in bems. *Applied Mathematical Modelling*, 25(11):901–922, 2001.

[103] O. Steinbach. *Numerical Approximation Methods for Elliptic Boundary Value Problems: Finite and Boundary Elements*. Texts in applied mathematics. Springer, 2008.

[104] G.T. Symm. Integral equation methods in potential theory. ii. *Proceedings of the Royal Society of London A: Mathematical, Physical and Engineering Sciences*, 275(1360):33–46, 1963.

[105] W. A. Wall, M. A. Frenzel, and C. Cyron. Isogeometric structural shape optimization. *Computer Methods in Applied Mechanics and Engineering*, 197(3340):2976 – 2988, 2008.

[106] L. Ying, G. Biros, and D. Zorin. A high-order 3d boundary integral equation solver for elliptic pdes in smooth domains. *Journal of Computational Physics*, 219(1):247–275, 2006.

[107] Y. Zhang, Y. Bazilevs, S. Goswami, C. L. Bajaj, and T. J. R. Hughes. Patient-specific vascular NURBS modeling for isogeometric analysis of blood flow. *Computer Methods in Applied Mechanics and Engineering*, 196(2930):2943 – 2959, 2007.

Vita

Matthias Franz Taus was born in Graz, Austria. In 2004, He finished high school, Bundesgymnasium und Bundesrealgymnasium, in Weiz, Austria. Matthias went to the University of Technology in Graz, Austria, from which he received a Bachelors and Masters degree in Technical Mathematics under the supervision of Olaf Steinbach. In 2010, he joined the Computational and Applied Mathematics program at the Institute for Computational Engineering and Sciences at the University of Texas at Austin.

Permanent address: matthias.taus@gmail.com

This dissertation was typeset with LaTeX[†] by the author.

[†]LaTeX is a document preparation system developed by Leslie Lamport as a special version of Donald Knuth's TeX Program.